

3D Electro-Magnetic Particle-In-Cell Simulation for Relativistic Jets

March 2017

Kazem Ardaneh

3D Electro-Magnetic Particle-In-Cell Simulation for Relativistic Jets

Graduate School of Systems and Information Engineering
University of Tsukuba

March 2017

Kazem Ardaneh

Abstract

An astrophysical jet is an event frequently found in Earth and Space Science, where flow of matter is ejected alongside the axis rotation of a compact object, for example in the accretion disk or massive objects such as black holes and neutron stars. When the relativistic jets interact with the ambient medium, two shocks will be excited, trailing shock and leading shock which are separated by a contact discontinuity (Zel'dovich and Raizer, 2002, Piran, 2003, Zhang and Kobayashi, 2005). The shocks are mediated by some plasma instabilities, such as electrostatic instabilities in the non-relativistic regime (two-stream or Buneman) and electromagnetic instabilities (Weibel or filamentation) in the relativistic regime (Buneman, 1958, Fried, 1959, Weibel, 1959, Nishikawa et al., 2003, 2005, Bret et al., 2010). The plasma instabilities are excited through the high degree of anisotropy in the particles phase-space on the jet-ambient interaction region. They grow at the expense of the kinetic energy stored in the incoming jet. In the relativistic regime, the kinetic energy of the incoming jet is transferred to the transverse electric and magnetic fields, and these fields then accelerate the particles mainly in the transverse directions (Hededal et al., 2004, Hededal, 2005a, Ardaneh et al., 2014, 2015, 2016).

Acceleration of particles is present in the astrophysical jets and shocks, although the mechanism of the particle acceleration still is not fully understood for the relativistic regime (Sironi, 2011). Generally, in the vicinity of the shocks, it is believed that particles are accelerated by the first-order Fermi acceleration which is based on the particles trapping and oscillating at the shock front (Blandford and Znajek, 1977, Blandford and Ostriker, 1978, Bell, 1978, 2013). In any reflection, the particles might gain energy from the magnetic fields generated around the shock front by the Weibel or filamentation instability (Spitkovsky, 2008b, Martins et al., 2009, Sironi and Spitkovsky, 2011, Sironi et al., 2013). The first-order Fermi acceleration can be directly applied for the ions, because the shock thickness is in the order of the several ion skin depths. However, for the electrons, participation in the Fermi acceleration is not straightforward. They need some pre-acceleration mechanisms to be capable for Fermi acceleration. The pre-acceleration mechanisms are not also clear so far and is called electron injection problem (Balogh and Treumann, 2013).

A magnetized jet with an upstream magnetic field as \vec{B}_0 has a motional electric field as $\vec{E}_0 = -\vec{\beta} \times \vec{B}_0$, where $\vec{\beta} = \vec{v}/c$ is the ratio of jet velocity to the speed of the light. For these cases, the motional electric field can provide the energization regarding the electron pre-acceleration. There are two possibilities: (1) The interactions between the reflected

jet ions and the incoming electrons can excite the Buneman instability (Buneman, 1958) which produces electrostatic solitary waves in the shock front. These waves trap the electrons and the trapped electrons are accelerated by the motional electric fields. This process is called shock surfing acceleration (Lee et al., 1996, Hoshino and Shimada, 2002, Shapiro and Ücer, 2003, Amano and Hoshino, 2009, Matsumoto et al., 2012) and was first reported for the ions (Lee et al., 1996). It is basically based on the trapping of the ions at the potential of the ambipolar electric fields associated with the electrostatic shocks or double layers. The trapped ions are accelerated by the motional electric fields of the upstream flow. The shock surfing acceleration is applicable just for the electron-ion plasmas, because if the species have same mass, and therefore same inertia, the electrostatic solitary waves would not be generated. (2) As we discussed in the shock surfing acceleration, if any process provides trapping of the electrons on the shock front, their acceleration is then plausible. The electrons may have drift perpendicular to the shock propagation direction as a result of the gradient of the magnetic fields at the shock front, in which the drift velocity is proportional to the $\vec{B} \times \nabla \vec{B} / B^2$ (Chen and Armstrong, 1975, Webb et al., 1983, Begelman and Kirk, 1990, Park et al., 2012, 2013, Guo et al., 2014). In these cases, the acceleration mechanism is called shock drift acceleration.

So far one question is still unanswered; how is the electron pre-acceleration in the unmagnetized jets? There is no motional electric field to accelerated the trapped electrons (if there is any trapped electron). A useful tool to investigate this course is particle-in-cell simulation. In this technique, the trajectories of particles are updated based on the electromagnetic fields calculated on the fixed grid points (Dawson, 1983, Birdsall and Langdon, 1991). The fields are defined on a three-dimensional staggered Yee mesh (Yee, 1966) and are updated by the source densities (charge and current) calculated from the charged particles. Performing a particle-in-cell simulation is limited by the available computational resources. Whereas plasma instabilities act in the scales related to the plasma skin depth, using the real proton-to-electron mass ratio (1836) would make the computations very expensive. Therefore, to perform an efficient simulation, we usually use a reduced mass ratio as 16 – 100. Furthermore, number of the particle per cell per species is another limiting parameter which affects the computational costs. For this case, we use the super particles that each of the super particles includes many real particles (Birdsall and Langdon, 1991).

Particle-in-cell simulation is employed in the study of the astrophysical shocks. To do so, in most of the simulations, the shocks are generated by the reflection of the incoming stream of plasma from a rigid boundary (Hoshino, 2001, Hoshino and Shimada, 2002, Spitkovsky, 2008a,b, Amano and Hoshino, 2009, Martins et al., 2009, Sironi and Spitkovsky, 2011, Sironi et al., 2013, Guo et al., 2014). Therefore, a shock is generated due to the interactions between the incoming and reflected stream. This method reduces

the computation efforts although it has some disadvantages as well; It simulates just one shock and is limited to two identical stream of plasmas. Another question arises here: How do we simulate the asymmetric shock cases? These cases are more computational demanding. In these thesis, I will focus on the jet-ambient interactions which can excite the double shock systems for the asymmetric cases (different properties for the jet and ambient). The simulations are based on a modified version of the three-dimensional particle-in-cell TRISTAN code.

The TRISTAN code is originally developed by [Buneman \(1993\)](#) to study the interaction between the solar winds and Earth magnetosphere. We adopted this code for relativistic jet-ambient interactions and parallelized it based on the Message Passing Interface on the basis of the algorithm discussed in [Wang et al. \(1995\)](#). It is performed on the Kyoto supercomputer Xe6 Machine, and its performance is analyzed for the strong and weak scaling setups. In the strong scaling where we divide a fixed problem size between multiple processors, the efficiency of the code decreases due to the increase of the communication time between the processors. However, for the weak scaling analysis where the problem size increases as number of the processors increases, we reach a efficiency of 95 % and a communication time around 4% of the computation time.

We use the adopted version of TRISTAN code to study the courses of the jet-ambient integrations. The first analysis is focused on the fields generation in the jet-ambient interactions, considering the earliest evolution in shock formation. Simulation results demonstrate that the Weibel instability is responsible for generating and amplifying the small-scale, fluctuating, and dominantly transversal magnetic fields. These magnetic fields deflect particles behind the beam front both perpendicular and parallel to the beam propagation direction. Initially, the incoming electrons respond to field fluctuations growing as the result of the Weibel instability. Therefore, the electron current filaments are generated and the total magnetic energy grows linearly due to the mutual attraction between the filaments, and downstream advection of the magnetic field perturbations. When the magnetic fields become strong enough to deflect the much heavier ions, the ions begin to get involved in the instability. Subsequently, the linear growth of total magnetic energy decreases because of opposite electron-ion currents and topological change in the structure of magnetic fields. The ion current filaments are then merged and magnetic field energy grows more slowly at the expense of the energy stored in ion stream. It has been clearly illustrated that the ion current filaments extend through a larger scale in the longitudinal direction, while extension of the electron filaments is limited. Hence, the ions form current filaments that are the sources of deeply penetrating magnetic fields. The results also reveal that the Weibel instability is further amplified due to the ions streaming, but on a longer time scale. Our simulation predictions are in valid agreement with analytical predictions.

The second analysis is focused on the collisionless external shocks, and the electron injection–acceleration associated with the unmagnetized relativistic jet propagating into an unmagnetized ambient plasma. In accordance with hydrodynamic shock systems (Zel’dovich and Raizer, 2002), the shock consists of a reverse shock and forward shock separated by a contact discontinuity. The development and structure are controlled by the ion Weibel-like instabilities. The ion filaments are sources of strong transverse electromagnetic fields at both sides of the double shock structure over a length of 30 - 100 ion skin depths. Electrons are heated up to a maximum energy $\epsilon_e \sim \sqrt{\epsilon_B}$, where ϵ is the energy normalized to the total incoming energy. The shock-reflected ambient ions generate a double layer in the reverse shock transition region which evolves consequently into an electrostatic shock. In addition, a double layer is formed in the forward shock transition region because of the decelerated jet ions and ambient electrons. The simulations show strong electron acceleration that is required for injecting the electrons into the diffusive shock acceleration. The large energy stored in the jet ions causes the extreme electron acceleration. The double layers convert directed ion energy into directed electron energy, without heating up the plasma. Electrons can thus be accelerated by the double layers to much higher speeds than by a shock because the latter also transfers flow energy into heat. The electron distribution functions in the reverse shock and forward shock transition regions show power-law distributions with index $p = 1.8 - 2.6$.

The results presented in this thesis are already published in the following journal articles:

1. **K. Ardaneh**, D. Cai, K.-I. Nishikawa. [Collisionless electron-ion shocks in relativistic unmagnetized jet-ambient interactions: Non-thermal electron injection by double layer](#). *The Astrophysical Journal*, 2016, Volume 827, 124 (15pp).
2. **K. Ardaneh**, D. Cai, K.-I. Nishikawa, B. Lembége. [Collisionless Weibel shocks and electron acceleration in gamma-ray bursts](#). *The Astrophysical Journal*, 2015, Volume 811 (1), 57 (9pp).
3. **K. Ardaneh**, D. Cai, K.-I. Nishikawa. [Amplification of Weibel instability in the relativistic beam-plasma interactions due to ion streaming](#). *New Astronomy*, 2014, Volume 33, pp. 1-6.

The presented results in the current thesis are associated to the particle-in-cell simulation of the relativistic electron-ion shocks generated by the propagation of the jets into the ambient in a self-consistent way. We have investigated the electron injection problem in the unmagnetized plasmas. More studies for the magnetized case with different oblique angles for the jet magnetic field, the different Lorentz factors, the different mass ratios, and etc., are considered in the future researches. Therefore, the suggestions for the futures works are summarized as follow:

1. The presented results are for the unmagnetized jet and ambient plasma. However, many of the astrophysical jets are magnetized. For this cases, we introduce the magnetization parameter σ as the ratio of the upstream magnetic energy to the incoming jet energy. Therefore, study of the magnetized cases for the different magnetization parameters would provide useful information about the effect of the upstream magnetic fields, regarding the self-consistent PIC simulation of the relativistic jets and shocks.
2. In the magnetized cases, the angle of the upstream magnetic field with respect to the propagation direction of the jet may also be an important parameter regarding the particle acceleration. Therefore, study of the particle acceleration for the different angles can also provide useful information about the effects of the oblique angle.
3. In this thesis, we consider two Lorentz factors, $\gamma = 5$, and $\gamma = 10$. Investigation of the dependence of particle acceleration, and fields strength to the jet Lorentz factor is also an important issue. For the larger Lorentz factors we need much larger simulation boxes and simulation times and we expect to detect stronger electromagnetic fields.
4. The presented works, we use the ion-to-electron mass ratio of 16, and 20. As will be discussed, these low mass ratios although are essential to make the computations efficient in three dimensions, they give a higher importance to the Weibel instability ([Bret and Dieckmann, 2010](#)). Therefore, using the larger mass ratios, such as 100 or higher, would provide more reliable results. However, for the large mass ratios, again we need large simulation boxes and simulation times.
5. Another important mechanism for the particle accelerating is magnetic reconnection, which spend the magnetic energy stored in the magnetic fields for the kinetic energy of the particles ([Zenitani and Hoshino, 2001, 2007, 2008](#), [Sironi and Spitkovsky, 2014](#)). Investigation of this issue can also provide better view about the responsible mechanisms for the particle acceleration in the jets and shocks. To follow this process, a large simulation box and longer simulation time is needed. During this process, the filaments merge together and reconnection would happen in some sites, where particle acceleration take places.

Contents

Contents	vi
List of Figures	viii
List of Tables	xiii
Abbreviations	xiv
Physical Constants	xv
Symbols	xvi

1 Introduction	1
1.1 Astrophysical jet	1
1.2 GRB	3
1.3 Relativistic shocks	5
1.4 Non-thermal radiation	8
1.5 PIC simulation	9
2 The TRISTAN PIC code	15
2.1 Kinetic vs fluid description of collisionless shocks	15
2.2 Governing equations	16
2.3 Features of TRISTAN	19
2.3.1 Heaviside form of governing equations	19
2.3.2 Spatial and temporal defenition in Yee lattice	19
2.3.3 Particle update	20
2.3.3.1 Particle position	20
2.3.3.2 Particle velocity	21
2.3.4 Force interpolation	22
2.3.5 Field update	24
2.3.5.1 Magnetic field update	24
2.3.5.2 Electric field update	25
2.3.5.3 Forth-order accurate for the curl operator	26
2.3.6 Parallelization	27
3 Fields generation in relativistic jet-ambient interactions	34
3.1 Introduction	35

3.2	Linear analysis	37
3.3	Parameters setup for PIC simulation	41
3.4	Simulation results	41
3.5	Conclusions	47
4	Collisionless shocks in relativistic jet-ambient interactions	49
4.1	Introduction	50
4.2	The fluid dynamics of relativistic shocks	52
4.2.1	Jump conditions for relativistic 90° shock	52
4.2.2	Jump conditions for jet-ambient interaction	54
4.3	Simulation model and parameters setup	56
4.4	Simulation results	58
4.4.1	Formation of the CD	58
4.4.2	Evolution of the TS	59
4.4.3	Evolution of the LS	64
4.4.4	Shock structure at the end of simulation	71
4.4.5	Formation of the double layers	72
4.4.6	Electron heating and acceleration	76
4.4.7	Evolution of the electron distribution function	79
4.4.8	Dependence on the dimensionality	80
4.5	Summary and conclusions	81
5	Conclusions	85
5.1	The presented works	85
5.2	Conclusions	85
5.3	Future works	87
A	The mean free path in relativistic jet-ambient interactions	90
	Acknowledgements	92
	Bibliography	93

List of Figures

1.1	An illustration of the Relativistic jet in AGN. The relativistic collimated stream of plasma outflow along the pole of SMBH. Source: en.Wikipedia.	2
1.2	M87 galaxy emit a relativistic jet, seen by the VLA. Source: Junor et al. (1999).	3
1.3	Pulsar IGR J11014-6103 with SNR origin, nebula and jet. Source: NASA/CXC/ ISDC/ Pavan et al. (2014).	4
1.4	Hubble detected infrared blaze of a kilo-nova explosion. Source: NASA/ESA/ Tanvir et al. (2013).	5
1.5	Number of bursts for the GRBs vs time. Source: NASA/ Paciesas et al. (1999).	6
1.6	Fireball scenario for the GRBs (Waxman, 2006). A shock system excited in relativistic jet-ambient interactions. The system includes two distinct shocks which are separated with a CD. Source: Piran (2003).	7
1.7	Fermi acceleration mechanism in a relativistic electron - positron shock. The particles achieve energy in any reflection on the shock front by the magnetic turbulences generated by the Weibel-like instabilities. Source: Spitkovsky (2008b).	7
1.8	The non-thermal radiation spectrum vs the thermal radiation spectrum. The non-thermal radiation can be expressed as a power-law function. Drown based on the Chaisson and McMillan (2014).	8
1.9	A cycle in a typical PIC code which includes sampling the contributions of the particles on the fields and the effects of the fields on the particles. Source: A. Marocchino Sapienza-Italy Website.	10
1.10	SSA for electron where an electron is trapped in an ESW and accelerated by the upstream electric field. Source: Hoshino and Shimada (2002).	11
1.11	SDA for electron where an electron drift perpendicular to the shock propagation direction and is accelerated by the upstream electric field. Source: Guo et al. (2014).	12
1.12	Self-consistent PIC simulation of the electron-positron shocks: (a) Average electron density as a function of the axial distance for the jet (red), ambient (blue), and total (black). (b) Average field energy as a function of the axial distance for the magnetic field (blue) and electric field (red). Source: Nishikawa et al. (2009).	13
2.1	The staggered Yee lattice (Yee, 1966). The \vec{E} components are defined at the middle of the cell edges, and the \vec{B} components are defined at the centre of the cell surfaces.	18
2.2	Time step chart for a typical PIC code. Source: Omura and Matsumoto (1993).	20

2.3	Velocity vector relation in Hartree method. Adopted from Birdsall and Langdon (1991), Buneman (1993).	21
2.4	The electric and magnetic components as presented in Yee lattice in green, and other possibilities which are shown in red and blue. Source: Greenwood et al. (2004).	27
2.5	A time step cycle of modified TRISTAN code. Blue boxes show the parallel parts.	29
2.6	TRISTAN code performance for fixed-sized problem as a function of number of processors N_p . Shown are (Left): Parallel efficiency and the communication time $T_{\text{com}}/T_{\text{tot}}$ as a function of N_p , (Right): Speedup as a function of N_p .	32
2.7	TRISTAN code performance for scale-sized problem as a function of number of processors N_p . Shown are: Parallel efficiency and the communication time $T_{\text{com}}/T_{\text{tot}}$ as the function of N_p . The black dashed line shows the line corresponding to the $\eta = 1 - T_{\text{com}}/T_{\text{tot}}$.	33
3.1	A simple illustration of the Weibel instability. Adopted based on the Medvedev and Loeb (1999).	36
3.2	(a) Weibel instability threshold map for different jet forward momentums, and (b) the Weibel instability growth rate vs wave number and perpendicular temperature for $\gamma_0 = 5$ and $\eta = 0.67$.	40
3.3	Time evolution of the square root of the normalized magnetic field energy density. The inset shows a log-log plot of the same data.	42
3.4	Distribution of jet particles (a) electrons at $t = 24.9\omega_{\text{pe}}^{-1}$ in $x - v_{\text{ve}}$ phase space, (b) electrons at $t = 24.9\omega_{\text{pe}}^{-1}$ in $x - v_{\text{pe}}$ phase space, (c) ions at $t = 69.72\omega_{\text{pe}}^{-1}$ in $x - v_{\text{vi}}$ phase space, and (d) ions at $t = 69.72\omega_{\text{pe}}^{-1}$ in $x - v_{\text{pi}}$ phase space,. Roughly 20% of the jet particles are randomly selected for these plots. $v_v = (v_y^2 + v_z^2)^{1/2}$, $v_p = v_x$.	43
3.5	One dimensional displays of transversally averaged electric and magnetic field energies at (a) $t = 24.9\omega_{\text{pe}}^{-1}$, (b) $t = 69.72\omega_{\text{pe}}^{-1}$.	43
3.6	Time evolution of the Weibel instability in the $x - z$ plane ($y = 16.67\lambda_{\text{ce}}$). Transverse magnetic field, B_y , at simulation times (a) $t = 19.92\omega_{\text{pe}}^{-1}$, (b) $t = 24.9\omega_{\text{pe}}^{-1}$, (c) $t = 69.72\omega_{\text{pe}}^{-1}$, (d) $t = 144.4\omega_{\text{pe}}^{-1}$.	44
3.7	Longitudinal current density through a transverse section. (a) Electron flux at $x = 25\lambda_{\text{ce}}$ and $t = 24.9\omega_{\text{pe}}^{-1}$, (b) Ion flux at $x = 83\lambda_{\text{ce}}$ and $t = 144.4\omega_{\text{pe}}^{-1}$.	45
3.8	Longitudinal current density in 3D view. The electron current density (negative) and the ion current density (positive) are shown with two different colors.	46
4.1	Illustration of the shock system. (a) illustration of a simple shock structure with the shock discontinuity separating the unshocked upstream medium and the shocked downstream medium drawn in a frame where the shock discontinuity is at rest, and (b) illustration of a double-shock structure with FS moving away from the shock creation site, RS moving back towards the shock creation site and the CD separating the downstream regions of the forward and the RS drawn in a frame where the CD is at rest. Adopted based on the Zhang and Kobayashi (2005), Zel'dovich and Raizer (2002), Piran (2003).	53

- 4.2 Illustration of the jet-ambient interaction showing (a) a particle jet being injected into an ambient plasma and (b) the resulting double shock structure. The shocks are named according to Nishikawa et al. (2009). 56
- 4.3 Structure of the jet-ambient interaction at time $t = 40\omega_{pe}^{-1}$ when the fastest jet ions reach $x = 45\lambda_{ce}$. The longitudinal phase-space distribution and density in log scale are displayed for the following: jet electrons in panels (a) and (b), ambient electrons in panels (c) and (d), jet ions in panels (e) and (f), and ambient ions in panels (g) and (h). The over-plotted line in panels (a), (c), (e), and (g), shows the average momentum in x -direction. The over-plotted line in panels (b), (d), (f), and (h), shows the transversely averaged (in yz -plane) density normalized to the density in the unshocked ambient. In panels (a), (c), (e), and (g), the phase-space distributions are expressed in $\log[N(x, p_x)]$ 60
- 4.4 The time evolution of the TS structure. Sequence snapshots of the magnetic field component B_y at $y = 24\lambda_{ce}$ from $t = 40\omega_{pe}^{-1}$ panel (a), up to $t = 280\omega_{pe}^{-1}$ panel (g), with an interval of $\Delta t = 40\omega_{pe}^{-1}$. Over-plotted in each panel is the transversely averaged total ion density normalized to the density in the unshocked ambient. 61
- 4.5 The longitudinal phase-space distribution of ambient ions expressed in $\log[N(x, p_x)]$ during evolution of the TS structure from $t = 80\omega_{pe}^{-1}$, panel (a), up to $t = 280\omega_{pe}^{-1}$, panel (f), with an interval of $\Delta t = 40\omega_{pe}^{-1}$. The position of the CD at each time is shown by a vertical white line. 62
- 4.6 The longitudinal phase-space distribution of jet electrons expressed in $\log[N(x, p_x)]$ during evolution of the TS structure from $t = 80\omega_{pe}^{-1}$, panel (a), up to $t = 280\omega_{pe}^{-1}$, panel (f), with an interval of $\Delta t = 40\omega_{pe}^{-1}$. The position of the CD at each time is shown by a vertical white line. 63
- 4.7 Structure of the trailing edge at time $t = 280\omega_{pe}^{-1}$. The density of the particle in log scale with an over-plotted line for the average density of the particle normalized to the density in the unshocked ambient is shown for the: (a) jet electron, (b) jet ion, (c) ambient electron, and (d) ambient ion, respectively. 65
- 4.8 Structure of the trailing edge at $t = 280\omega_{pe}^{-1}$. Panels (a), (b) and (c) show the components of the magnetic field B_x , B_y , and B_z , respectively, at $y = 24\lambda_{ce}$. Panels (d), (e) and (f) show the components of the electric field E_x , E_z , and E_y , respectively, at $y = 24\lambda_{ce}$. The transversally averaged field components $(E_x : B_x)$, $(E_z : B_y)$, and $(E_y : B_z)$ are shown in panels (g), (h) and (i), respectively. 66
- 4.9 The time evolution of the TS structure. Sequence snapshots of the magnetic field component B_y at $y = 24\lambda_{ce}$ from $t = 300\omega_{pe}^{-1}$, panel (a), up to $t = 500\omega_{pe}^{-1}$, panel (f), with an interval of $\Delta t = 40\omega_{pe}^{-1}$. Over-plotted in each panel shows the transversely averaged (in yz -plane) total ion density normalized to the density in the unshocked ambient. 67
- 4.10 The longitudinal phase-space distribution of ambient electrons expressed in $\log[N(x, p_x)]$ during evolution of the LS structure from $t = 300\omega_{pe}^{-1}$, panel (a), up to $t = 500\omega_{pe}^{-1}$, panel (f), with an interval of $\Delta t = 40\omega_{pe}^{-1}$. The position of the CD at each time is shown by a vertical white line. 68

- 4.11 The longitudinal phase-space distribution of ambient ions expressed in $\log[N(x, p_x)]$ during evolution of the LS structure from $t = 300\omega_{pe}^{-1}$, panel (a), up to $t = 500\omega_{pe}^{-1}$, panel (f), with an interval of $\Delta t = 40\omega_{pe}^{-1}$. The position of the CD at each time is shown by a vertical white line. 69
- 4.12 Structure of the leading edge at time $t = 500\omega_{pe}^{-1}$. The density of the particle in log scale with an over-plotted line for the average density of the particle normalized to the density in the unshocked ambient is shown for the: (a) jet electron, (b) jet ion, (c) ambient electron, and (d) ambient ions, respectively. 70
- 4.13 Structure of the leading edge at $t = 500\omega_{pe}^{-1}$. Panels (a), (b) and (c) show the components of the magnetic field B_x , B_y , and B_z , respectively, at $y = 24\lambda_{ce}$. Panels (d), (e) and (f) show the components of the electric field E_x , E_z , and E_y , respectively, at $y = 24\lambda_{ce}$. The transversally averaged field components $(E_x : B_x)$, $(E_z : B_y)$, and $(E_y : B_z)$ are shown in panels (g), (h) and (i), respectively. 71
- 4.14 Panel (a) shows stacked profiles of the transversely averaged ion density (total jet+ambient) from $t = 20\omega_{pe}^{-1}$ up to $540\omega_{pe}^{-1}$ with an interval of $\Delta = 20\omega_{pe}^{-1}$ and panel (b) represents the ion density profile at $t = 500\omega_{pe}^{-1}$. Solid, dashed-dot, and dotted black lines in panel (a) indicate the TS, LS, and jet front, respectively. In panel (b) the shocked region is shown as orange, yellow represents the shock transition region (left for the TS and right for the LS), white shows the unshocked regions (jet or ambient), and the dashed blue line shows the CD. 72
- 4.15 Structure of the relativistic double shock at $t = 500\omega_{pe}^{-1}$. Panels (a) and (b) show the z -component of the electric field E_z and the y -component of the magnetic field B_y at $y = 24\lambda_{ce}$. Panels (c)-(e) show the transversally averaged (in the yz -plane) field components. Total of the jet (blue) + ambient (red) particle energy distribution, and average energy along x -direction are presented in panels (f) and (g) for electrons, and (h) and (i) for ions. The shocked region is identified by orange coloring or between vertical orange lines. The ellipse in panel (f) shows the high-energy electrons reflected into the upstream. In (f) and (h), 1.2×10^6 particles are randomly selected. Due to the very large number of particles in the simulation, only a part of them is represented. Particles of each population are selected randomly so that the respective distribution function is not affected. 74
- 4.16 The stacked profiles of the transversely averaged E_x is shown from $t = 20\omega_{pe}^{-1}$ up to $500\omega_{pe}^{-1}$ with an interval of $\Delta t = 20\omega_{pe}^{-1}$. Dashed-dot-dot, dashed-dot, and dashed lines represent the TS, LS, and jet ions front, respectively. 75
- 4.17 Longitudinal current density through a transverse cross section at $x = 320\lambda_{ce}$ (first column) and $x = 480\lambda_{ce}$ (second column) for $t = 500\omega_{pe}^{-1}$. The arrows represent the transverse magnetic (first row), and electric (second row) fields. 77
- 4.18 Electrons heating and acceleration. Displayed are: (a) magnetic energy density ϵ_B , normalized to the jet energy density, (b) average change in the electron energy due to the transverse electric fields of ion filaments, $\langle \Delta E_e / m_e c^2 \rangle = \langle \Delta \gamma_e \rangle$, (c) average change in the electron kinetic energy due to the double layer electric field, $e\langle \phi \rangle / m_e c^2$, and (d) average electron energy, $\langle \Delta \gamma_e \rangle$, along x -direction. All panels are calculated at $t = 500\omega_{pe}^{-1}$. 78

- 4.19 Evolution of the electron distribution function from $t = 20\omega_{\text{pe}}^{-1}$ (leftmost red line) up to $500\omega_{\text{pe}}^{-1}$ (rightmost orange line) with an interval of $\Delta t = 20\omega_{\text{pe}}^{-1}$: (a) for ambient in the leading edge taken at $(\beta_{41} - \beta_{1s1})t\omega_{\text{pe}}^{-1}$, (b) for ambient+jet in the shocked region taken at $(\beta_{1s1} - \beta_{ts1})t\omega_{\text{pe}}^{-1}$, and (c) for jet in the trailing edge taken at $x/\lambda_{\text{ce}} \lesssim \beta_{ts1}t\omega_{\text{pe}}^{-1}$. White line in panel (a) and (c) shows a power-law fit to the non-thermal component in the electron distribution function at the latest time. The inset in panel (c) shows the time evolution of the most probable momentum for jet electrons, p_{mpm} 80
- 4.20 2D run: Evolution of the electron distribution function from $t = 20\omega_{\text{pe}}^{-1}$ (leftmost red line) up to $560\omega_{\text{pe}}^{-1}$ (rightmost cyan line) with an interval of $\Delta t = 20\omega_{\text{pe}}^{-1}$: (a) for ambient in the leading edge taken at $(\beta_{41} - \beta_{1s1})t\omega_{\text{pe}}^{-1}$, and (b) for jet in the trailing edge taken at $x/\lambda_{\text{ce}} \lesssim \beta_{ts1}t\omega_{\text{pe}}^{-1}$. White line shows a power-law fit to the non-thermal component in the electron distribution function at the latest time. 81
- 5.1 Illustration of the magnetic reconnection where magnetic field lines configuration is reformed, panel (a), and the magnetic energy will be transferred to the kinetic energy of the particle in the reconnection site, panels (b), (c), and (d). Source: Sironi and Spitkovsky (2014). 89

List of Tables

2.1	System A supercomputer on the KDK computer system at Research Institute for Sustainable Humanosphere, Kyoto University. Source: Research Institute for Sustainable Humanosphere, Kyoto University.	31
4.1	Parameters of the formed double shock structure.	58

Abbreviations

AGN	A ctive G alactic N uclei
BH	B lack H ole
BS	B inary S ystem
CD	C ontact D iscontinuity
CR	C osmic R ay
D	D imension
DSA	D iffusive S hock A cceleration
ESW	E lectrostatic S olitary W ave
FDTD	F inite D ifference T ime D omain
FS	F orward S hock
GRB	G amma R ay B urst
ISM	I nter S tellar M edium
MHD	M agneto H ydro D ynamic
MPI	M essage P assing I nterface
PIC	P article I n C ell
PWN	P ulsar W ind N ebula
RS	R everse S hock
SDA	S hock D rift A cceleration
SSA	S hock S urfing A cceleration
SNR	S uper N ova R emnant
SMBH	S upper M assive B lack H ole

Physical Constants

Speed of Light	c	$=$	$2.99792458 \times 10^8 \text{ms}^{-1}$
Electron charge	e	$=$	$1.602 \times 10^{-19} \text{ C}$
Electron mass	m_e	$=$	$9.109 \times 10^{-31} \text{ Kg}=0.511\text{MeVc}^{-2}$
Proton mass	m_p	$=$	$1.673 \times 10^{-27} \text{ Kg}=938.272\text{MeVc}^{-2}$
Neutron mass	m_n	$=$	$1.675 \times 10^{-27} \text{ Kg}=939.566\text{MeVc}^{-2}$
Avogadro number	N_A	$=$	$6.022 \times 10^{23} \text{mol}^{-1}$
Boltzmann constant	K_B	$=$	$1.381 \times 10^{-23} \text{JK}^{-1}$
Gas constant	R	$=$	$8.31 \text{Jmol}^{-1} \text{K}^{-1}$
Permittivity of free space	ε_0	$=$	$8.854 \times 10^{-12} \text{Fm}^{-1}$
Permeability of free space	μ_0	$=$	$4\pi \times 10^{-7} \text{NA}^{-2}$

Symbols

\vec{B}	Magnetic field	T or G
c_s	Sound velocity	ms^{-1}
\vec{D}	Displacement field	Cm^{-2}
\vec{E}	Electric field	Vm^{-1}
e	Elementary charge	C
f	Density function	m^{-3}
\vec{i}	unit vector in x -direction	
\vec{J}	Current density	Am^{-2}
\vec{j}	unit vector in y -direction	
\vec{k}	unit vector in z -direction or wave vector	m^{-1}
k	wave number	m^{-1}
L	Length	m
M	Mach number	
m	Mass	Kg
N	Number of particles	
n	Number density	m^{-3}
P	Pressure	Nm^{-2}
\vec{p}	Momentum	Kgms^{-1}
q	charge	C
R	Radius	m
\vec{r}	Position vector	m
T	Temperature	K
t	Time	s
\vec{v}	Velocity vector	ms^{-1}
v	speed	ms^{-1}

u	Energy density	Jm^{-3}
α	Power-law index	
β	Ratio of speed to the speed of light c	
δ	Difference operator	
Δ	grid space	m
ϵ_e	flow energy stored in the electrons	
ϵ_B	flow energy stored in magnetic fields	
ϕ	Electric potential	V
Γ	Growth rate	s^{-1}
$\tilde{\Gamma}$	Adiabatic index	
γ	Lorentz factor	
λ	Skin depth	m
μ	Molar enthalpy	Jm^{-3}
ρ	Charge density	Cm^{-3}
τ	Proper time	s
σ	Magnetization	
ω	Angular frequency	Rads^{-1}

Chapter 1

Introduction

1.1 Astrophysical jet

An astrophysical jet is an event frequently found in Earth and Space Science, where flow of matter is ejected alongside the axis rotation of a compact object. Although it is still under the examination to see how outflow are shaped and energized, the two suggested sources are the dynamical interactions through the accretion disk, or a process related to the massive objects ([Junor et al., 1999](#), [de Gouveia Dal Pino, 2005](#), [Pavan et al., 2014](#)), such as BHs (Figures [1.1](#) and [1.2](#)) and neutron stars (Figures [1.3](#)). When matter travels at the speeds close to the speed of the light, the jets are referred to as relativistic jets. Most of the jets are ejected from BHs in active galaxies, for example, quasars and radio galaxies. Relativistic jets lengths can achieve a few thousand or even a huge number of light years ([Biretta, 1957](#)).

Accretion disks around massive stellar items can eject the jets, in spite of the fact that those from SMBHs are mainly the fastest and most active. It has been known that the speed of the jet is proportional to the matter escape speed from the central object ([de Gouveia Dal Pino, 2005](#)). Although it is not known precisely how accretion disk will energize jets or generate positron-electron-ion plasma, they are mostly believed to produce transverse electromagnetic fields that force the jets to propagate in collimate way ([David et al., 2001](#), [de Gouveia Dal Pino, 2005](#)).

The bipolar outflows are astonishingly usual in Astrophysics and Astronomy. They have been probed in relation to the AGNs, young stellar objects, binary X-ray sources, SNRs and so on ([de Gouveia Dal Pino, 2005](#)). The outflow speeds are also in order of the escape speed from the central object; for the AGNs, Lorentz factors of $\gamma \sim 10$ are proven ([Bykov and Treumann, 2011](#)).

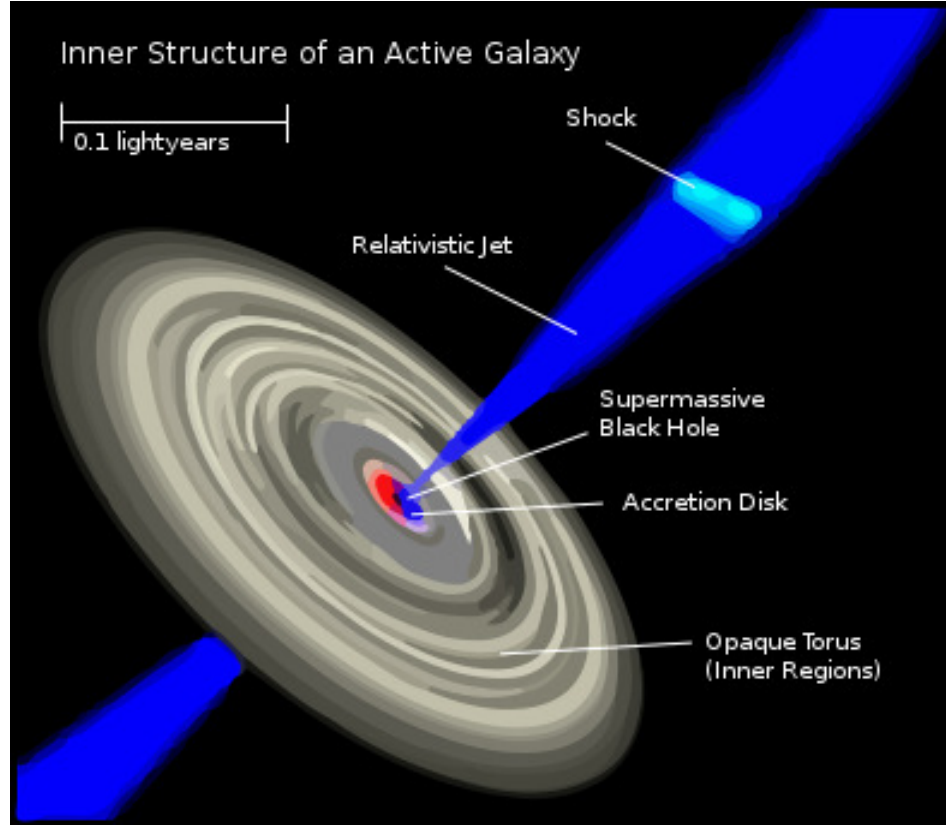


FIGURE 1.1: An illustration of the Relativistic jet in AGN. The relativistic collimated stream of plasma outflow along the pole of SMBH. Source: [en.Wikipedia](https://en.wikipedia.org/wiki/Active_galaxy#/media/File:AGN_diagram.png).

The massive galactic central BHs include the most powerful jets. Similar jets on a smaller scale are ejected from neutron stars and stellar BHs. These objects are usually called micro-quasars. Two examples are M87 ([Junor et al., 1999](#)), and SS433 ([Cherepashchuk, 2002](#)) which the detected jet has a speed of $0.23c$, although other micro-quasars seem to have higher jets speeds. Weaker and non-relativistic jets can be related to many BSs; the acceleration process for them might be like the magnetic reconnection mechanism which is detected in the interactions of the solar winds with Earth's magnetosphere ([Frey et al., 2003](#)).

Whereas large amount of energy is required for producing the relativistic jets, it is believed that some of the relativistic jets are associated with the rotating BHs. Two famous processes are accepted regarding the transformation of the energy from the BHs to the jets ([Blandford and Znajek, 1977](#), [Penrose, 1969](#), [de Gouveia Dal Pino, 2005](#)):

1. Blandford-Zanjek mechanism: It is the common concept for the energy pumping from a BH. Because of the BH rotation, magnetic fields around the disk are twisted. The relativistic particles are probably produced due to the twisting of the field lines.

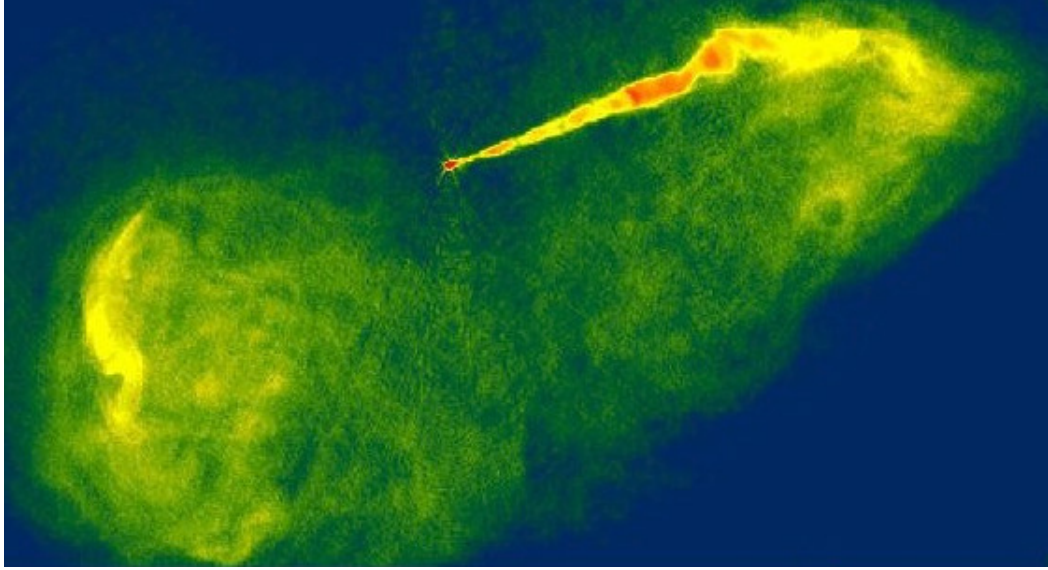


FIGURE 1.2: M87 galaxy emit a relativistic jet, seen by the VLA. Source: [Junor et al. \(1999\)](#).

2. Penrose process: This mechanism pumps energy from a rotating BH via the frame dragging. At first, this process was shown to be capable to explain the ejection of relativistic particle and consequently proven to be a promising process for the jets formation.

Neutron stars might also inject the jets. An example is the pulsar IGR J11014-6103 ([Pavan et al., 2014](#)), Figure 1.3, which generated the largest observed jet in the Milky-Way Galaxy. The jet is observed in X-rays and has no observed radio signature. The neutron star magnetic fields launch the jets and the magnetic field rotation will generate strong electric fields that rip particles from the star surface and form the jets. IGR J11014-6103 has an approximately speed of $0.8c$.

1.2 GRB

The common idea in the Astronomy and Astrophysics is that the relativistic jets is the crucial concept to explain the generation of GRBs. The relativistic jets in the GRBs have Lorentz factors of $\gamma \sim 100$ or larger ([Bykov and Toptygin, 1985](#), [Bykov and Treumann, 2011](#)), labeling them as some of the strangest celestial phenomena currently known. In the observational methods, to examine the process which generate jets, the jet composition is determined at radii where they may be detected straightly. For BH jets, the plasma include electron-ion if the jet propagates from a disk, or positron-electron if it propagates from the BH ([Wardle et al., 1989](#)).

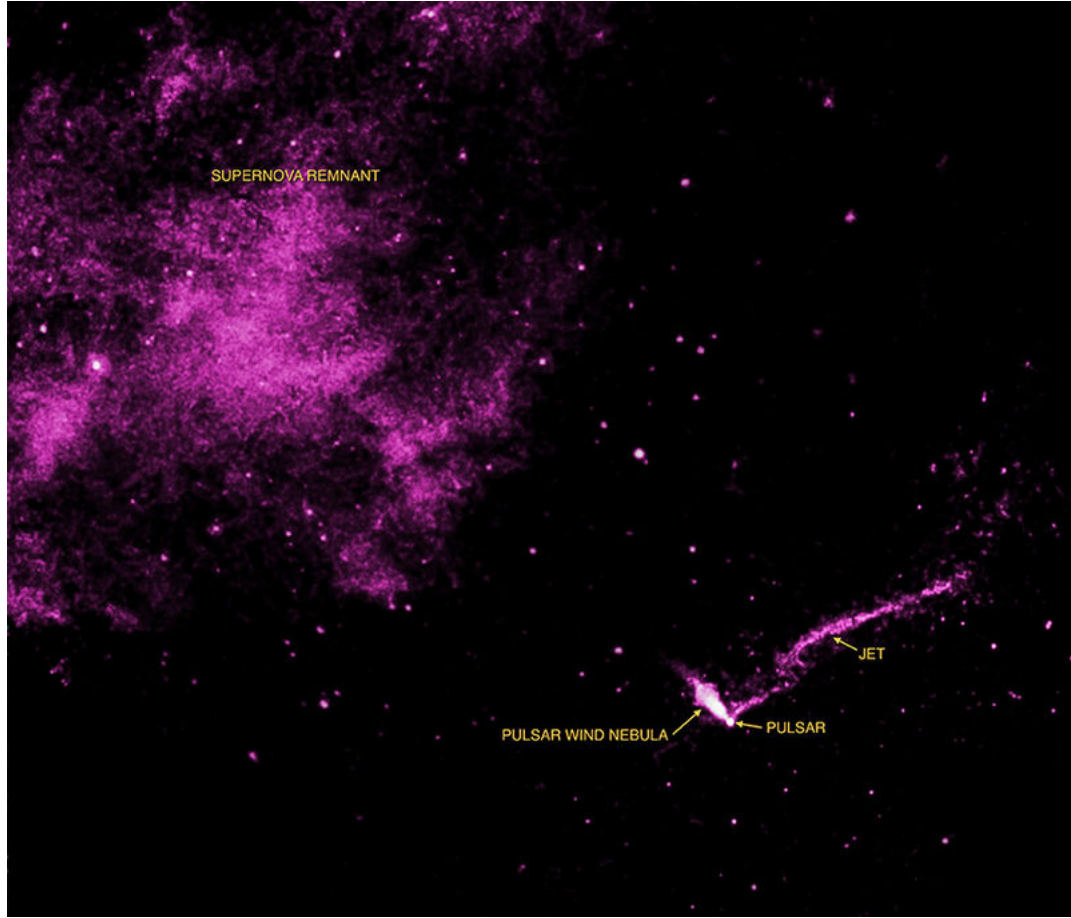


FIGURE 1.3: Pulsar IGR J11014-6103 with SNR origin, nebula and jet. Source: [NASA/CXC/ ISDC/ Pavan et al. \(2014\)](#).

The first GRBs were detected in the late 1960s by Vela satellites in US ([Schilling, 2002](#)). GRBs are considered as short lived bursts of gamma-ray light (Figure 1.4), having the shortest wavelength among the light wavelengths. They last from a few milliseconds up to several minutes ([Bykov and Treumann, 2011](#)). The luminosity of the GRBs are several times larger than a usual SN and around a million trillion times larger than the Sun $L \sim 10^{45}$ J/Sec ([Schilling, 2002](#), [Bykov and Treumann, 2011](#)). During the burst of a GRB, it would be the brightest origin of cosmic gamma-ray photons in the visible universe.

To the date, GRBs are debatably the greatest anonymous in high-energy Astrophysics. Confirmations from recent satellites, such as Fermi, show that the energy following a GRB derives from the direct collapse of matter into a BH ([Schilling, 2002](#)). When scientist investigated the number of bursts vs their lifetime, they discovered two distinctive types of bursts: long-term and short-term ([Paciesas et al., 1999](#)), Figure 1.5.

1. Long-term bursts last from two seconds to several minutes, with a typical time of around 30 seconds. They are related with the demises of massive stars in SNs;

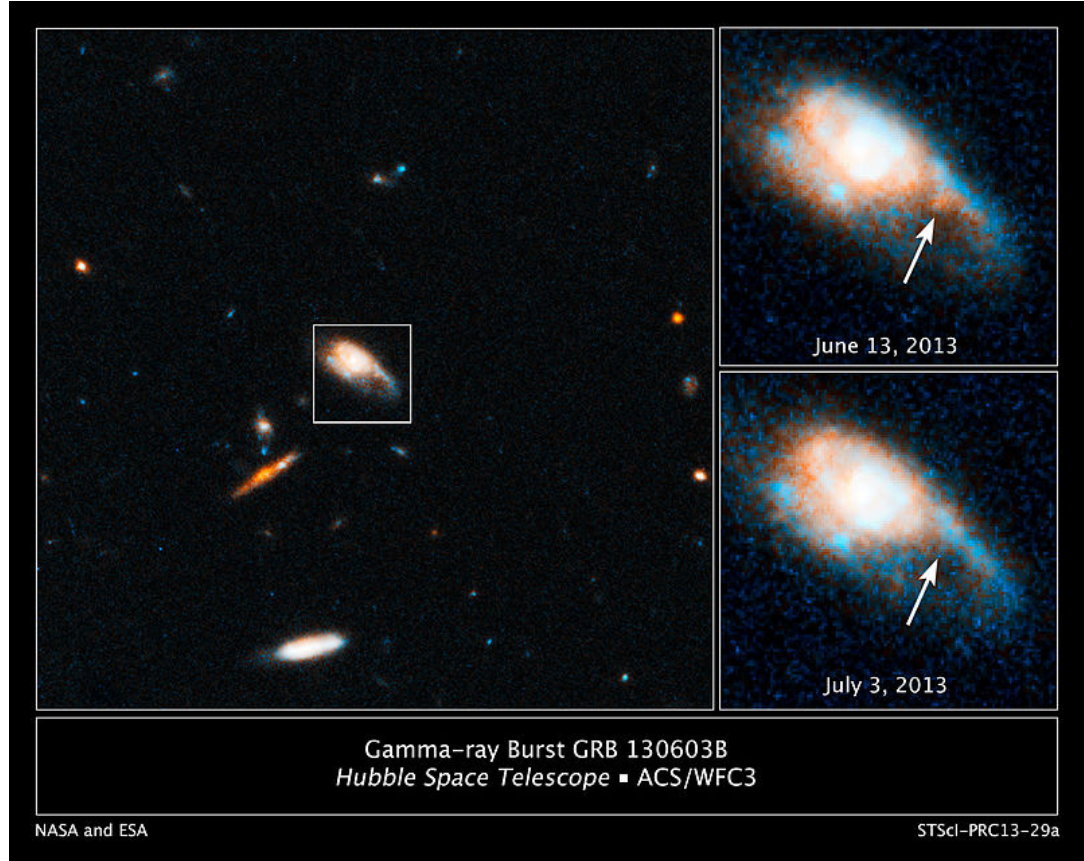


FIGURE 1.4: Hubble detected infrared blaze of a kilo-nova explosion. Source: [NASA/ESA/ Tanvir et al. \(2013\)](#).

however not all SN creates a GRB.

2. Short-term bursts last from a few milliseconds to two seconds with a typical time of around 300 milliseconds. They are related to the combining of two neutron stars to form a brand new BH or a neutron star together with a BH which form a larger BH.

1.3 Relativistic shocks

Although the real origin of the GRBs is not fully understood so far, the most accepted model for the generation of the gamma ray radiation is based on the so-called Fireball scenario ([Waxman, 2006](#)). In this model, the gamma ray radiation are associated with the high-energetic particles which are accelerated at the relativistic shock sides. Shocks are ubiquitous in astrophysical systems. When relativistic jets interact with the ambient medium, two shocks will be excited, RS and FS which are separated by a CD (Figure 1.6), as discussed in [Zel'dovich and Raizer \(2002\)](#), [Piran \(2003\)](#), [Zhang and Kobayashi](#)

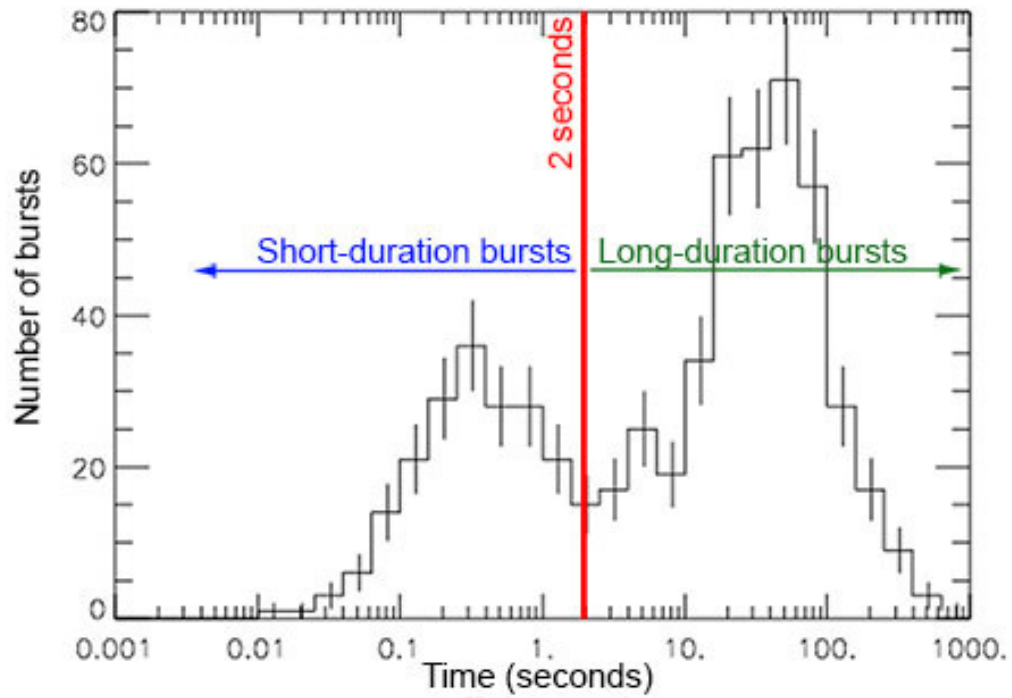


FIGURE 1.5: Number of bursts for the GRBs vs time. Source: [NASA/ Paciesas et al. \(1999\)](#).

(2005). Due to the low particle density in ambient, mostly the astrophysical shocks are referred to as collisionless ([Zel'dovich and Raizer, 2002](#), [Hededal, 2005a](#)). In this case, the mean free path for the Coulomb collision between two particles is much larger than system size (see Chapter 2 and Appendix A) and the resulting shocks are not excited by Coulomb collisions, and are referred to as collisionless shocks. It is extensively believed that plasma instabilities handle the process of shocks formation ([Medvedev and Loeb, 1999](#), [Hededal, 2005a](#), [Spitkovsky, 2008a](#)). These instabilities function on the spatial scale of the plasma skin depth which is naturally much shorter than the Coulomb collision mean free path.

It is recognized that high-energy particles are tied to the collisionless shocks, although the mechanism of the particle acceleration still is not fully understood. Furthermore, It is not absolutely recognized whether the detected high-energy photons are produced by electrons, ions or both. In the shock systems, the high-energy particles are in overall accepted to attain energy via the first-order Fermi process ([Blandford and Znajek, 1977](#), [Blandford and Ostriker, 1978](#), [Bell, 1978, 2013](#)). In this mechanism, charged particles gain energy as they are reflected backward and forward in the vicinity the shock surface by the magnetic turbulences generated by some plasma instabilities (see Figure 1.7), such as Weibel ([Weibel, 1959](#)) and filamentation instabilities. It is shown that shocks excited by SNRs propagating in the ISM accelerate the CRs ([Hoshino, 2001](#), [Hoshino and Shimada, 2002](#), [Amano and Hoshino, 2009](#)). One important sort of astrophysical

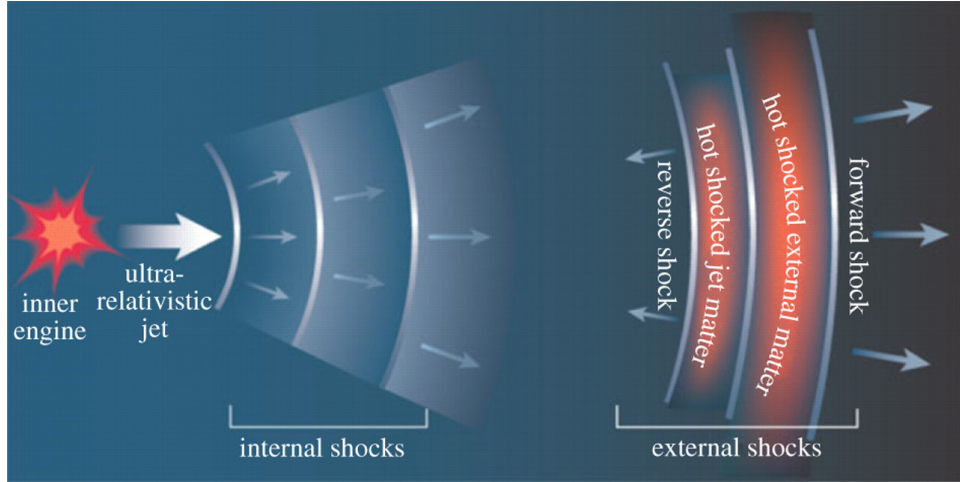


FIGURE 1.6: Fireball scenario for the GRBs (Waxman, 2006). A shock system excited in relativistic jet-ambient interactions. The system includes two distinct shocks which are separated with a CD. Source: Piran (2003).

shocks is the relativistic shock, where the shock speed is close to the speed of light. The relativistic shocks are hypothetically predictable in GRBs, AGNs jets and in several kinds of SN bursts.

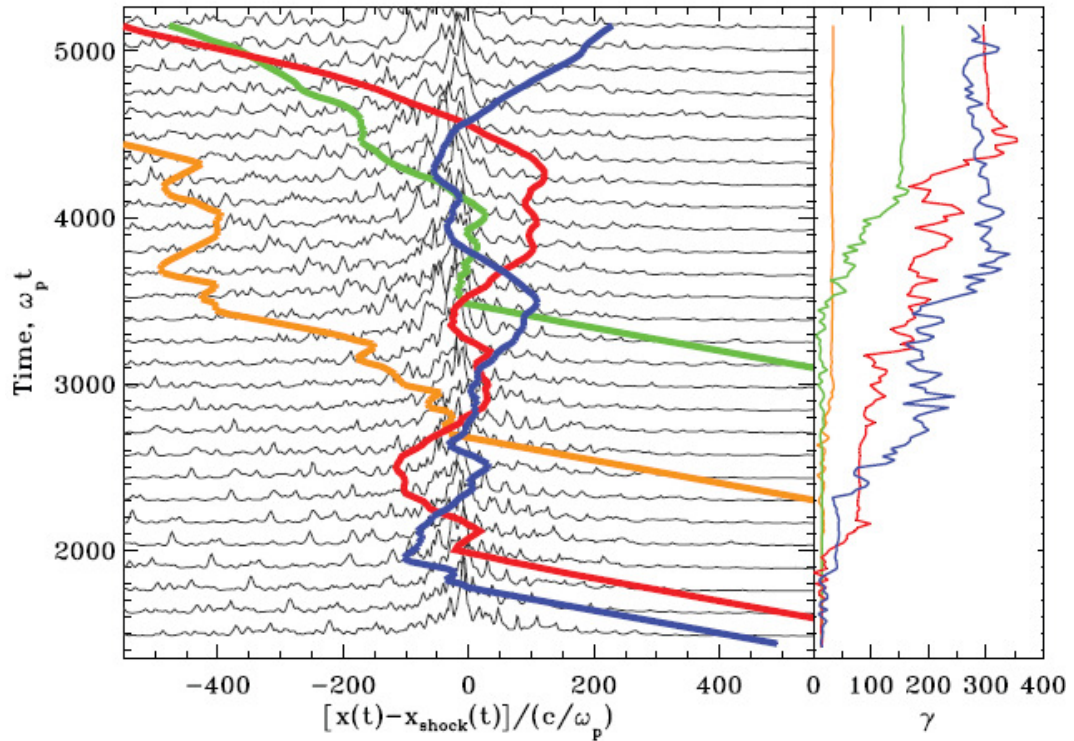


FIGURE 1.7: Fermi acceleration mechanism in a relativistic electron - positron shock. The particles achieve energy in any reflection on the shock front by the magnetic turbulences generated by the Weibel-like instabilities. Source: Spitkovsky (2008b).

1.4 Non-thermal radiation

Radiations from the relativist shock have a power-law pattern as $F(\nu) \propto \nu^{-s}$ (Figure 1.8), and range within the radio-to-gamma band (Heddal, 2005a, Sironi, 2011). In this case, the features of the emissions are not related to the temperature of the medium and the radiation is referred to as non-thermal radiation. In Astronomy and Astrophysics, two usual forms of non-thermal radiation exist (Rybicki and Lightman, 1979):

1. Synchrotron radiation: it is produced by charged particles gyrating around magnetic field lines with the relativistic speeds.
2. Compton scattering: In this case the electrons are affected by high energy photons and consequently the photons are scattered after transferring some fraction of their energy to electrons.

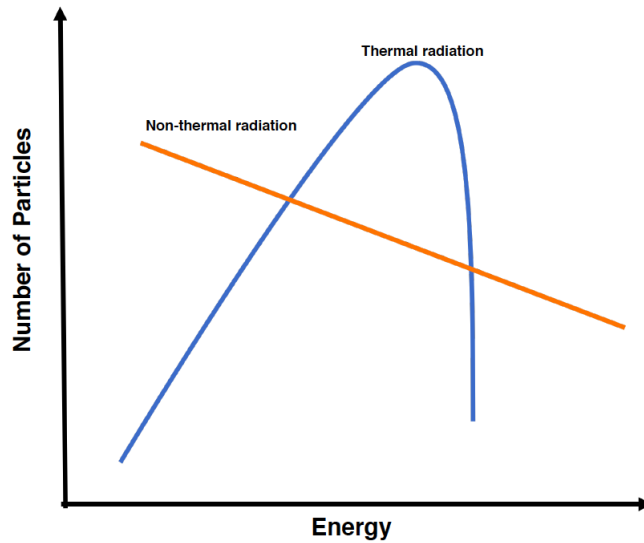


FIGURE 1.8: The non-thermal radiation spectrum vs the thermal radiation spectrum. The non-thermal radiation can be expressed as a power-law function. Drown based on the Chaisson and McMillan (2014).

It has been proven that Fermi acceleration can accelerated the particles such that their distribution function include a power-law regime at high energies with a power-law index as $dN(p)/dp \propto p^{-\alpha}$ with $\alpha \gtrsim 2$ (Bell, 1978, 2013, Balogh and Treumann, 2013). The power-law pattern has been observed for the radio emissions with the index of $\alpha \sim 1-1.2$ (Eriksen et al., 2011) and for the X-ray emissions with the index of $\alpha \sim 2.3-2.6$ (Koyama et al., 1995). This power-law index is related to the spectral index by $s = (\alpha - 1)/2$ (Rybicki and Lightman, 1979). Therefore, the spectral index for the radio emissions is $s \sim 0.5 - 0.6$ and for the X-ray emissions is $s \sim 1.1 - 1.3$ (Sironi, 2011). Due to the anisotropy in the angular momentum and the relativistic effects, the Fermi acceleration

can not be applied directly to the relativistic regime and acceleration mechanisms in this case are still under the investigation (Sironi, 2011). Moreover, Fermi acceleration can be applied straightforwardly to the ions because their Larmor radius is in order of the shock thickness. However, because of the small Larmor radius for the electron, electrons can cross the shock front without any significant reflection. Therefore, to participate in a Fermi-like process, electron need a pre-acceleration process. This mechanism still is not fully understood and is called electron injection problem (Balogh and Treumann, 2013).

1.5 PIC simulation

The PIC technique is used to solve a special course of partial differential equations. In this technique, individual particles are followed in continuous phase-space in a Lagrangian frame, while macroscopic properties, such as densities, fields, and current are treated at the same time on Eulerian (stationary) frame. The PIC technique was used even before the primitive Fortran compilers were accessible. The technique was picked up in the late 1950s and mid 1960s for plasma studies (Dawson, 1983). In a typical PIC code, the trajectories of individual charged particles are traced in a self-consistent way based on the electromagnetic fields computed on a stationary grid (Dawson, 1983). The approach normally includes the ensuing steps (Figure 1.9) as discussed in (Birdsall and Langdon, 1991):

1. Weighting of charge particles in the mesh points and calculate the current density on the mesh points.
2. Calculation of the electromagnetic fields on mesh points.
3. Interpolation of the electromagnetic fields to the positions of the particles.
4. Integration of the equation of motion for the individual particles.

In the PIC simulations, various species, such as electrons, ions, and dust particles are used. The set of the equations are the Lorentz force as the equation of motion, named as pusher or particle mover of the code, and Maxwell's equations deciding the electromagnetic fields, computed in the field solver (Birdsall and Langdon, 1991). The PIC codes include large number of the particles based on the simulation size which is desired. However, due to the lack of the numerical resources the used number of particles per cell in a PIC code is limited. Keeping in mind the end goal to do an efficient PIC, theoretical super-particles are utilized (Birdsall and Langdon, 1991). A super-particle stays as a theoretical particle that contains many actual particles; a huge number of

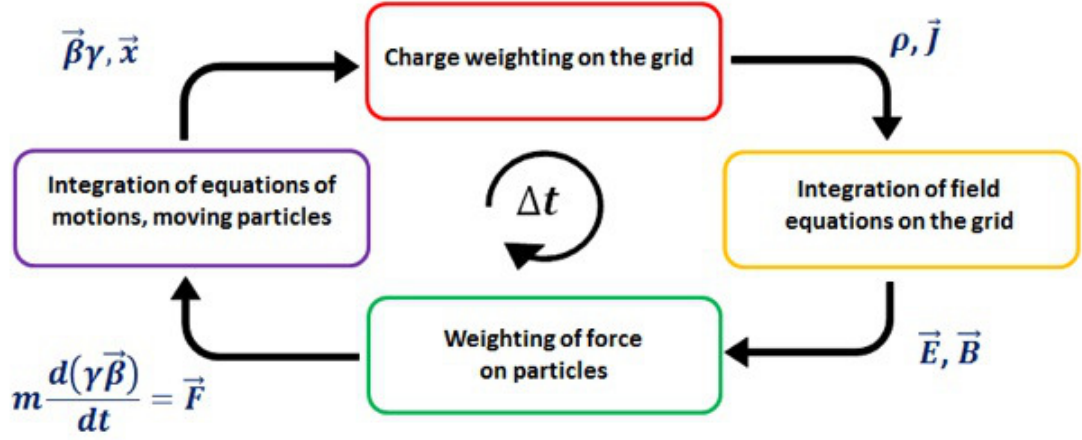


FIGURE 1.9: A cycle in a typical PIC code which includes sampling the contributions of the particles on the fields and the effects of the fields on the particles. Source: [A. Marocchino Sapienza-Italy Website](#).

electrons or ions. Whereas the Lorentz force depends just on the charge to mass ration, a super-particle will follow the same path as a physical particle would.

The PIC codes are useful tools for examination of the particle acceleration mechanisms and used for many application in astrophysical jets and shocks ([Hoshino, 2001](#), [Hoshino and Shimada, 2002](#), [Spitkovsky, 2008a,b](#), [Amano and Hoshino, 2009](#), [Martins et al., 2009](#), [Sironi and Spitkovsky, 2011](#), [Sironi et al., 2013](#), [Guo et al., 2014](#)). Regarding the relativistic jets, and shocks, the most of the progresses were made during the current decade through the improvement of the available numerical resources ([Spitkovsky, 2008a,b](#), [Amano and Hoshino, 2009](#), [Martins et al., 2009](#), [Sironi and Spitkovsky, 2011](#), [Sironi et al., 2013](#), [Guo et al., 2014](#)). In most of the simulations, to save the numerical efforts, just one relativist jet is selected. Therefore, to excite the shock, the incoming jet is reflected from a stiff boundary at the opposite side. However, this type of simulation is not self-consistent cause it assumes a sharp CD and neglects the dynamic of the CD and jet front. Furthermore, it can just capture one shock for the symmetric beams interactions. These simulations found a similar process to first-order Fermi acceleration in both electron-positron and electron-ion shocks ([Spitkovsky, 2008b](#), [Martins et al., 2009](#)). The electron injection problem is also studied via this type of the simulation. It has been shown that electron injection in magnetized upstream is related to the upstream motional electric filed, the electric fields due to the motion of the magnetized upstream ($\vec{E} = -\vec{\beta} \times \vec{B}$). Two type of injection mechanism are proposed in the magnetized upstream ([Hoshino, 2001](#), [Hoshino and Shimada, 2002](#), [Amano and Hoshino, 2009](#), [Guo et al., 2014](#)):

1. SSA: In the SSA process, the incoming electrons are trapped at the shock front due to the ESWs generated by the Buneman instability (See Figure [1.10](#)), and have

surf around the shock front (Hoshino, 2001, Hoshino and Shimada, 2002, Amano and Hoshino, 2009). Therefore, they may be accelerated by the motional electric fields. It has been demonstrated that SSA can produce an electron distribution function which includes a power-law segment with slope of 2.0-2.5 within the shock transition region (Amano and Hoshino, 2009).

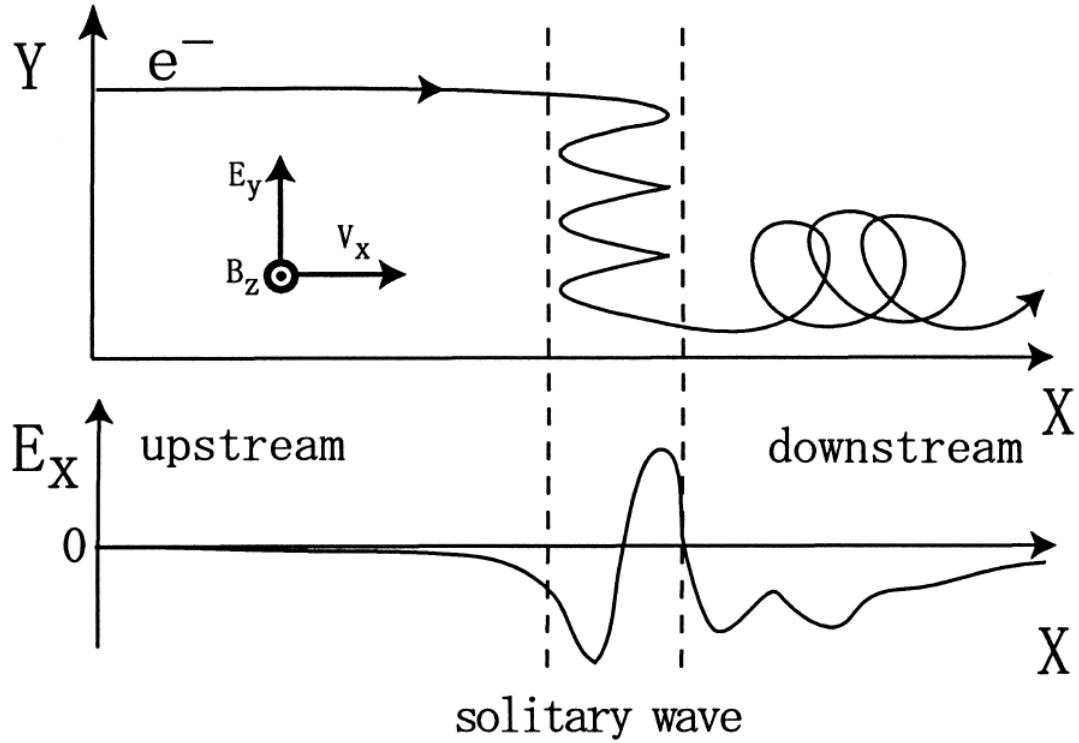


FIGURE 1.10: SSA for electron where an electron is trapped in an ESW and accelerated by the upstream electric field. Source: Hoshino and Shimada (2002).

2. SDA: In the SDA, the incoming electrons drift in the perpendicular directions with respect to the shock propagation direction (See Figure 1.11), as a result of the gradient of the magnetic fields at the shock front (Chen and Armstrong, 1975, Webb et al., 1983, Begelman and Kirk, 1990, Park et al., 2012, 2013, Guo et al., 2014). In this case, it is also possible for them to be accelerated by the motional electric fields. It has been shown that SDA may generate an electron distribution function which includes a power-law segment with slope of 2.4 within the shock transition region (Guo et al., 2014)

To this point, we can see there are two unresolved issues:

1. Self-consistent shock simulation: It means simulation of the GRBs shock such that both shocks be captured.
2. Electron injection problem in unmagnetized upstream: Due to the lack of the motional electric fields, other mechanisms are involved rather than SSA and SDA.

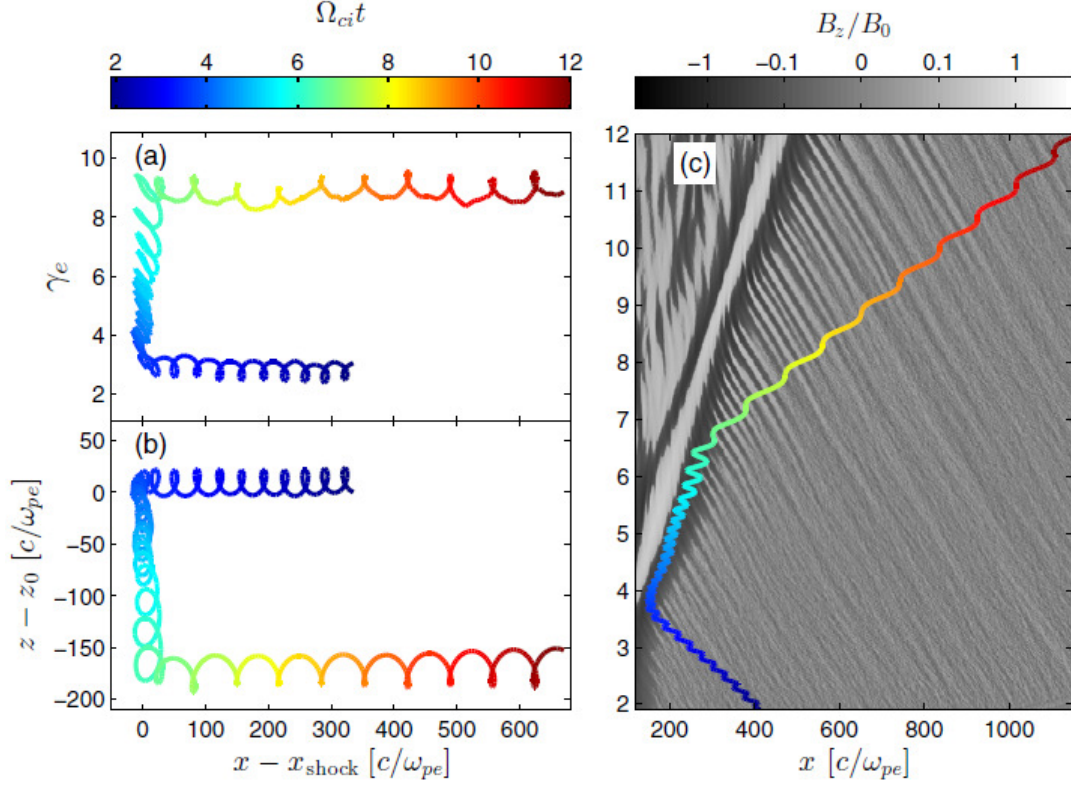


FIGURE 1.11: SDA for electron where an electron drift perpendicular to the shock propagation direction and is accelerated by the upstream electric field. Source: [Guo et al. \(2014\)](#).

Self-consistent simulations were conducted in [Nishikawa et al. \(2003, 2005\)](#), although the simulation scales were not enough large to capture a relativistic shock system as shown in Figure 1.6. These studies showed that Weibel-like instabilities ([Fried, 1959](#), [Weibel, 1959](#), [Bret, 2009](#), [Bret et al., 2010](#)) generate the transverse electromagnetic fields within the jet-ambient interaction region. Later, [Nishikawa et al. \(2009\)](#) reported the first 3D self-consistent simulation of the electron-positron shock (Figure 1.12). They showed that in the jet-ambient interaction, two different shocks will be excited. The electromagnetic fields are more stronger in the TS region than in the LS region, due to the high degree of anisotropy in the TS region. The electromagnetic fields convert around 30% of the incoming jet kinetic energy to the particles in the TS region (see Figure 1.12). However, simulation of the electron-ion shocks demand much large simulation size and time. In this case, [Choi et al. \(2014\)](#) reported the results for a long size in the jet direction (x -direction in their setup), but small size in the transverse direction (three ion skin depths). They captured a hybrid structures for the shock including the double layer and electrostatic shocks.

In this thesis, I have performed several large 3D PIC simulations to simulate the unmagnetized electron-ion shocks. I have used the different jets relative to the previous studies ([Nishikawa et al., 2003, 2005, 2009](#), [Choi et al., 2014](#)), denser and hot jets.

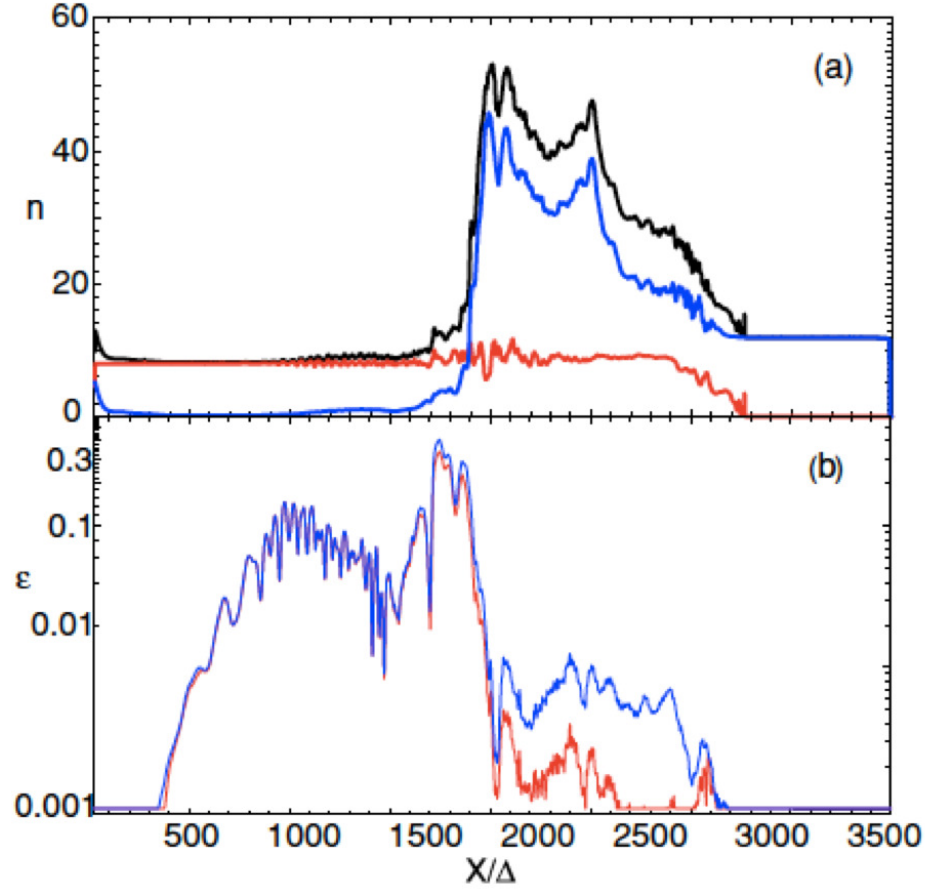


FIGURE 1.12: Self-consistent PIC simulation of the electron-positron shocks: (a) Average electron density as a function of the axial distance for the jet (red), ambient (blue), and total (black). (b) Average field energy as a function of the axial distance for the magnetic field (blue) and electric field (red). Source: [Nishikawa et al. \(2009\)](#).

The electron injection problem is comprehensively studied. The shock structure is analyzed and compared with the hydrodynamical system. Both parallel plasma instabilities (two-stream or Buneman instabilities ([Buneman, 1958](#))) and perpendicular instabilities (filamentation or Weibel instabilities) are present in these simulations. Therefore, the wave spectrum propagate obliquely relative to the jet propagation direction.

The code employed in the present work is an adopted version of the relativistic electromagnetic particle code TRISTAN ([Buneman, 1993](#)) with MPI parallelization. The details of the parallel PIC TRISTAN code is presented in Chapter 2. The electromagnetic fields generation in relativistic jet-ambient interactions is discussed in Chapter 3. The relativistic collisionless shocks and course of electron injection-acceleration are studied in Chapters 4. In Chapters 5, I conclude with a summary and some suggestions for the future works. The results presented in Chapter 3 and Chapter 4 are based on three published papers as detailed below:

1. **K. Ardaneh**, D. Cai, K.-I. Nishikawa. [Collisionless electron-ion shocks in relativistic unmagnetized jet-ambient interactions: Non-thermal electron injection by double layer](#). *The Astrophysical Journal*, 2016, Volume 827, 124 (15pp).
2. **K. Ardaneh**, D. Cai, K.-I. Nishikawa, B. Lembége. [Collisionless Weibel shocks and electron acceleration in gamma-ray bursts](#). *The Astrophysical Journal*, 2015, Volume 811 (1), 57 (9pp).
3. **K. Ardaneh**, D. Cai, K.-I. Nishikawa. [Amplification of Weibel instability in the relativistic beam-plasma interactions due to ion streaming](#). *New Astronomy*, 2014, Volume 33, pp. 1-6.

Chapter 2

The TRISTAN PIC code

In this chapter I briefly describe the aspects of TRISTAN PIC code, and explain why PIC simulation is essential compared to a fluid description. I also discuss about suppressing some numerical instabilities. Finally, I describe in some details parallelization of the TRISTAN code.

2.1 Kinetic vs fluid description of collisionless shocks

The mean free path for the 90° Coulomb collision between an electron moving with momentum $\gamma v_e m_e$ in an ambient plasma with density n is approximated as (see [Appendix A](#) for details):

$$\lambda_{\text{mfp}} = \frac{32\pi\epsilon_0^2\gamma^2 v_e^4 m_e^2}{ne^4} \quad (2.1)$$

For the relativistic jets that propagates into the ambient medium, we can use this equation to approximate the mean free path for Coulomb collisions between the jets and ambient particles. With an ambient density $n = 10^6 \text{m}^{-3}$ and a jet bulk Lorentz factor $\gamma = 10$ ($v_e = 0.995c$), the mean free path for Coulomb collisions is $\lambda_{\text{mfp}} = 10^{24} \text{m}$. This is billion times large than the expected size of the fireball. Therefore, it is natural to expect a relativistic jet to propagate unrestricted through the ambient medium. However, it is in straight contrast with observational properties, where GRBs afterglows are explained by synchrotron or inverse Compton radiations from slowed down relativistic jets that interacts with, and heats - accelerates, the ambient medium. Absence of interactions imposes serious complications in explanation of the particle acceleration and source of the magnetic fields, that are required to generate the detected synchrotron

radiation (Waxman, 1997, Sari et al., 1998). The interaction driver must be located in the micro-physical processes between particles and electromagnetic fields (Sagdeev, 1966). Therefore, it makes sense that a dealing of the jet-ambient interaction musts to be started. For this objective, we need a theoretical framework. Using the MHD framework in this regard is useless by several opinions (Hededal, 2005a):

1. The low collision rate between the ions and electrons would not provide the satisfactorily fast equilibration for the plasma to perform as a fluid. It also happens for the low energy shocks related to the SNRs (Vink, 2004). Observations are consistent with a population of high-energy accelerated particles overlaid on a low-energy background population (Gruzinov, 2001).
2. MHD shocks are stable and do not produce magnetic field turbulences. In these cases, magnetic fields are only compressed with a subsequent field strength that is orders of magnitudes lower than what is needed for the synchrotron radiation from the GRB afterglows (Gruzinov, 2001).

2.2 Governing equations

Our interested area is within the the kinetic and highly non-linear regime of plasma physics. For these type of the problems, we start from the beginning by working on the Maxwell's equations with source densities for the electromagnetic fields, and the relativistic equation of motion for charged particles (Birdsall and Langdon, 1991).

$$\nabla \cdot \vec{E} = \frac{\rho}{\epsilon_0} \quad (2.2a)$$

$$\nabla \times \vec{B} = \frac{1}{c^2} \frac{\partial \vec{E}}{\partial t} + \mu_0 \vec{J} \quad (2.2b)$$

$$\nabla \times \vec{E} = -\frac{\partial \vec{B}}{\partial t} \quad (2.2c)$$

$$\nabla \cdot \vec{B} = 0 \quad (2.2d)$$

and

$$m \frac{d(\gamma \vec{v})}{dt} = q(\vec{E} + \vec{v} \times \vec{B}) \quad (2.3a)$$

$$\frac{d\vec{r}}{dt} = \vec{v} \quad (2.3b)$$

where ϵ_0 and μ_0 are the electric permittivity and magnetic permeability of vacuum with $c^2 \epsilon_0 \mu_0 = 1$, m is the mass, and q is charge of a particle of a given species, \vec{v} is the velocity

vector and $\gamma = (1 - v^2/c^2)^{-1/2}$ is the relativistic Lorentz factor. The source densities, \vec{J} and ρ , in the above equations are determined by the particles in the simulations.

We are going to find a general solution for the coupled differential equations of Eqs. 2.2 and Eqs. 2.3. Having the initial-boundary conditions, for roughly 10^{25} particles, this solution is not possible to be achieved analytically. Nevertheless, the solution of a scaled-down version of the same problem is achievable numerically, with PIC codes (Birdsall and Langdon, 1991). As discussed before, a PIC technique integrates the trajectories of the charged particles in the electromagnetic fields. Some restrictions are included in this technique. Some of the major differences between a PIC modeled plasma and an actual plasma are as follow (Birdsall and Langdon, 1991, Hededal, 2005a):

1. The number of particles in the actual plasma are very large to be loaded in a computer memory: Each $1 \times 1 \times 1 \text{ m}^3$ cube of the ISM includes roughly 10^6 charged particles, which is hardly computationally possible today. Therefore, in the PIC simulations, each particle represents a super-particle that includes a large number of actual plasma charges. Each super-particle has the same charge to mass ratio as the summation of individual particles on it.
2. While continuous in phase-space, the particles positions are discretized in time.
3. The electric and magnetic fields are discretized in space and time. The governing equations are integrated on a Eulerian grid and the interactions with the particles are handled via the interpolations from grid to positions of particles and vice versa. The electric and magnetic field components and source densities are staggered and assigned on a 3D Yee lattice (Yee, 1966). It causes improvement of the resolution that is to a factor 16 in calculating time (Figure 2.1).
4. Most of the plasma instabilities develop on time scales close to the plasma frequency $\tau \propto \omega_p^{-1}$ and on length scales that are related to the skin depth $\delta \propto c/\omega_p$. A large spatial-temporal problems exist in the plasma processes that are ruled by ions (protons) and electrons. To adopt with the restraints in computational resources, it is usual to reduce the dynamical ranges by decreasing the ion (proton)-to-electron mass ratio m_i/m_e from the real value 1836 to 16-100.
5. The maximum temporal and spatial scales in PIC simulations are limited because it is important to resolve micro-physical plasma oscillations. Because the electron plasma frequency ω_{pe} is regularly the restrictive factor, we normalize time relative to the oscillation period ω_{pe}^{-1} and the space relative to the electron skin depth c/ω_{pe} . The plasma frequency is defined as $\omega_{pe} = (n_e q^2 / m_e \epsilon_0)^{-1/2}$, and thus the plasma density n_e determines the re-scaling.

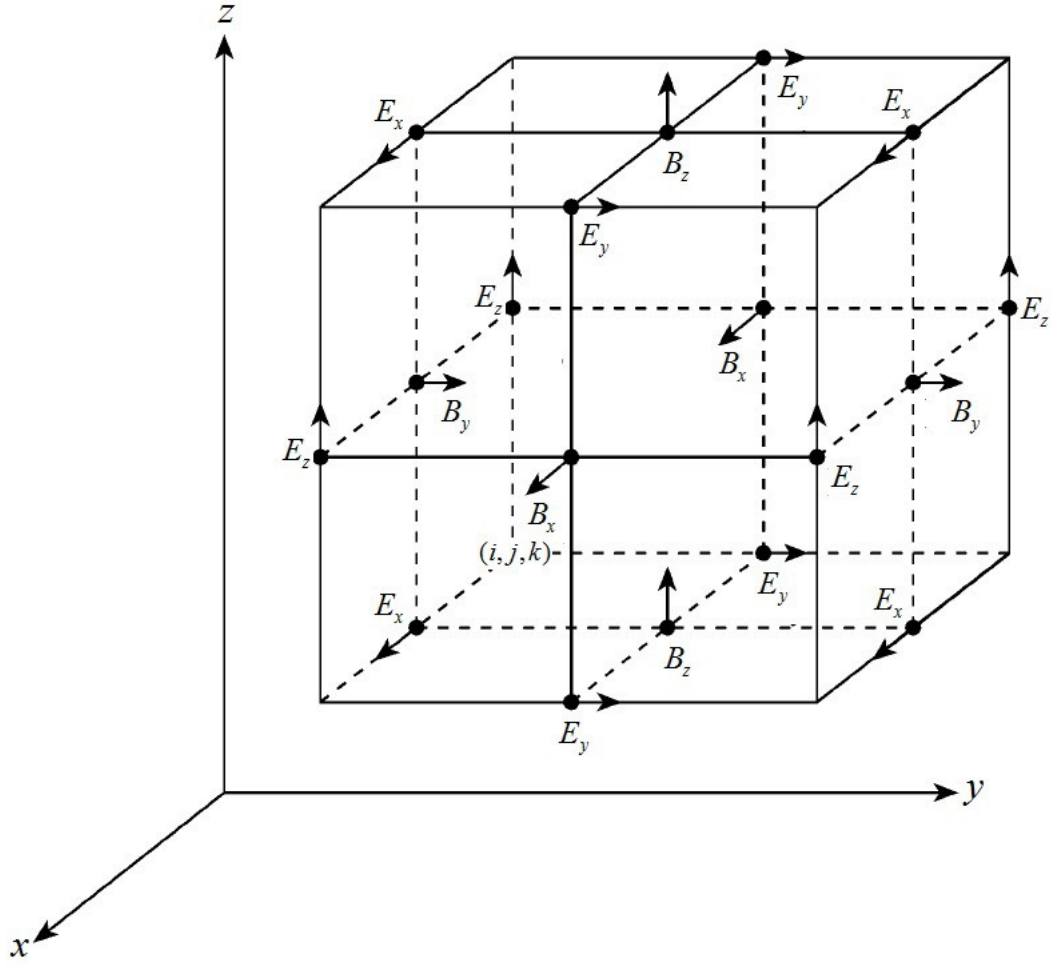


FIGURE 2.1: The staggered Yee lattice (Yee, 1966). The \vec{E} components are defined at the middle of the cell edges, and the \vec{B} components are defined at the centre of the cell surfaces.

More than these limits, the PIC modeling of a plasma is far more fundamentally than the MHD modeling. The PIC simulations are still computationally challenging and fully 3D simulations have only become practically doable within the last few years.

In this thesis, I have employed the 3D TRISTAN PIC code, which I participated in the development at [University of Tsukuba](#) by the supervisory of my PhD supervisor [Prof. Dongsheng Cai](#). It is a MPI parallel version of the TRISTAN originally written by [Buneman \(1993\)](#). It can handle the large scale simulation for the ultra-relativistic flows.

2.3 Features of TRISTAN

The basic features of the original TRISTAN code are discussed in [Buneman \(1993\)](#), and more details are available in [Birdsall and Langdon \(1991\)](#). Here, I presented the basic features of our adopted code borrowed from the original TRISTAN code, and additional implemented aspects.

2.3.1 Heaviside form of governing equations

For the normalization of the TRISTAN code, we use:

$$\epsilon_0 = 1 \quad (2.4a)$$

$$\mu_0 = \frac{1}{c^2} \quad (2.4b)$$

Therefore:

$$\vec{D} = \vec{E} \quad (2.5a)$$

$$c^2 \vec{B} = c(c\vec{B}) = c\vec{B}' \quad (2.5b)$$

Substituting equation Eqs. 2.5 into equations Eqs. 2.2, we derive Heaviside form of Maxwell's equations:

$$\frac{\partial \vec{E}}{\partial t} = c \nabla \times \vec{B}' - \vec{J} \quad (2.6a)$$

$$\frac{\partial \vec{B}'}{\partial t} = -c \nabla \times \vec{E} \quad (2.6b)$$

Therefore, Ampere's and Faraday equations are mutually symmetrical in form.

2.3.2 Spatial and temporal definition in Yee lattice

The fields and particles in current version of the TRISTAN are updated based on what is used in KEMPO1 ([Omura and Matsumoto, 1993](#)) and is shown in Figure 2.2. In this chart, the full-integer time is shown as $n\Delta t$ while half-integer time is shown as $(n + 1/2)\Delta t$. The electric field \vec{E} and the magnetic field \vec{B} are integrated via the leap-frog, at the full-integer and half-integer time step, respectively. The magnetic field \vec{B} is updated via two half time steps $\Delta t/2$ to calculate midway fields required for the particle pusher. The particle positions \vec{r} and the velocities \vec{v} are advanced by the leap-frog approach at the full-integer and the half-integer time step, respectively. The positions are advanced via two half time steps $\Delta t/2$ to calculate midway values for the calculation

of the current density \vec{J} . The current density \vec{J} then can be calculated from the positions and velocities of particles.

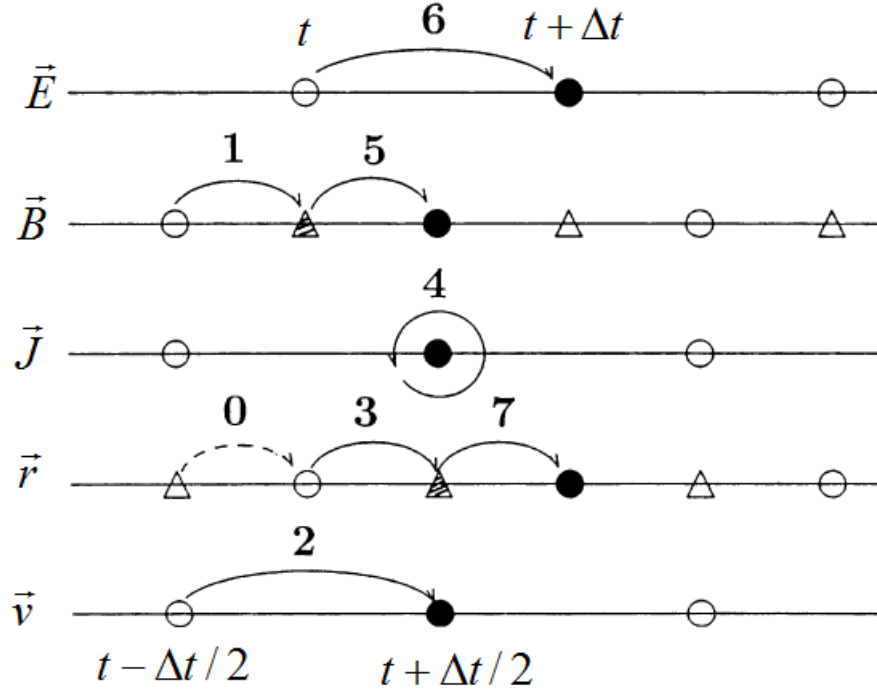


FIGURE 2.2: Time step chart for a typical PIC code. Source: [Omura and Matsumoto \(1993\)](#).

In the PIC codes, to use the standard leap-frog method, the electric field components E_x , E_y , E_z are defined at the midpoint of the cell edges. Also, the current density components J_x , J_y , and J_z are defined at the same point of E_x , E_y , E_z . Furthermore, the magnetic fields component B_x , B_y , B_z are defined at the midpoint of the cell surfaces. This definition is referred to as Yee lattice which is illustrated in Figure 2.1.

2.3.3 Particle update

2.3.3.1 Particle position

The discretized form of the equation of motion Eq. 2.3b in 3D is given by:

$$\vec{r}_{t+\Delta t} = \vec{r}_t + \Delta t \vec{v}_{t+\Delta t/2} = \vec{r}_t + \Delta t \frac{\vec{p}_{t+\Delta t/2}}{m\gamma_{t+\Delta t/2}} \quad (2.7)$$

where $\vec{p} = m\gamma\vec{v}$

2.3.3.2 Particle velocity

The time-centering finite difference form of the Newton-Lorentz equation Eq. 2.3a in non-relativistic case is:

$$\vec{v}_{t+\Delta t/2} - \vec{v}_{t-\Delta t/2} = \frac{q\Delta t}{m} [\vec{E}_t + \frac{1}{2}(\vec{v}_{t+\Delta t/2} + \vec{v}_{t-\Delta t/2}) \times \vec{B}_t] \quad (2.8)$$

The usual calculation is performed with the following method, which is called Hartree method (Birdsall and Langdon, 1991). By introducing the following two variables

$$\vec{v}_- = \vec{v}_{t-\Delta t/2} + \frac{q\Delta t}{2m} \vec{E}_t \quad (2.9a)$$

$$\vec{v}_+ = \vec{v}_{t+\Delta t/2} + \frac{q\Delta t}{2m} \vec{E}_t \quad (2.9b)$$

Eq. 2.8 can be modified as:

$$\vec{v}_+ - \vec{v}_- = \frac{q\Delta t}{m} [\vec{E}_t + \frac{1}{2}(\vec{v}_{t+\Delta t/2} + \vec{v}_{t-\Delta t/2}) \times \vec{B}_t] \quad (2.10)$$

The dot product of Eq. 2.10 with $\vec{v}_+ + \vec{v}_-$ (Figure 2.3 shows that $\vec{v}_+ + \vec{v}_-$ is perpendicular to $\vec{v}_+ - \vec{v}_-$, So $(\vec{v}_+ + \vec{v}_-).(\vec{v}_+ - \vec{v}_-) = 0$) results in $\vec{v}_+^2 = \vec{v}_-^2$.

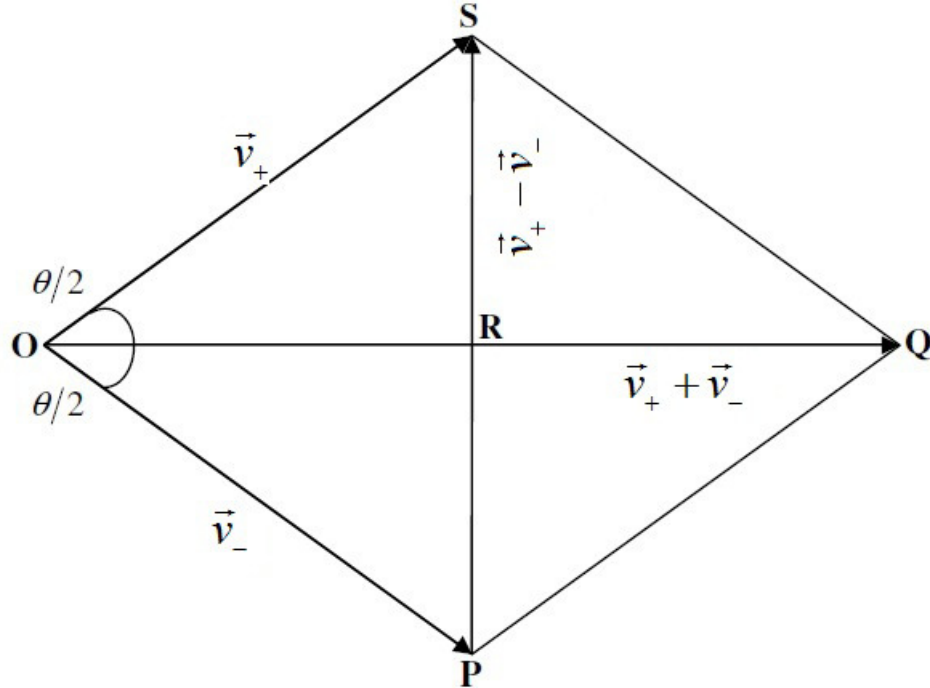


FIGURE 2.3: Velocity vector relation in Hartree method. Adopted from Birdsall and Langdon (1991), Buneman (1993).

It is expected because the kinetic energy of a particle is conserved during gyration around the magnetic fields. From the Figure 2.3, we can write

$$\tan \frac{\theta}{2} = \frac{\Delta t}{2} \frac{q}{m} |\vec{B}| \quad (2.11a)$$

$$\cos^2 \frac{\theta}{2} = \frac{1}{1 + \tan^2 \frac{\theta}{2}} = \frac{1}{1 + (\frac{\Delta t}{2} \frac{q}{m} |\vec{B}|)^2} \quad (2.11b)$$

$$\vec{v}_+ - \vec{v}_- = 2\vec{v}_o \cos^2 \frac{\theta}{2} \times \vec{B}_t \frac{\Delta t}{2} \quad (2.11c)$$

To update the velocity, there are three steps in this method as follow:

1. Half electric acceleration: At first, the new middle velocity \vec{v}_- is derived from the old velocity $\vec{v}_{t-\Delta t/2}$ in half time step using Eq. 2.9a.
2. Pure magnetic rotation: The new velocity \vec{v}_0 is calculated from \vec{v}_- as

$$\vec{v}_0 = \vec{v}_- + \frac{q\Delta t}{2m} \vec{v}_- \times \vec{B}_t \quad (2.12)$$

Then, \vec{v}_+ can be calculated using Eq. 2.11c.

3. Another half electric acceleration: The particle is accelerated in the other half time step. Then the new velocity $\vec{v}_{t+\Delta t/2}$ is derived using Eq. 2.9b.

This algorithm can be simply extended for the relativistic case using $\vec{u} = \vec{p}/m = \gamma\vec{v}$ instead of \vec{v} in Eq. 2.8. Hence

$$\vec{u}_{t+\Delta t/2} - \vec{u}_{t-\Delta t/2} = \frac{q\Delta t}{m} [\vec{E}_t + \frac{1}{2\gamma_t} (\vec{u}_{t+\Delta t/2} + \vec{u}_{t-\Delta t/2}) \times \vec{B}_t] \quad (2.13)$$

where

$$\gamma_t^2 = 1 + u_t^2/c^2 \quad (2.14)$$

2.3.4 Force interpolation

To calculate the Newton-Lorentz force in Eq. 2.3a, The electric and magnetic fields should be interpolated at the position of the particles, cause they are defined the computational grid points. To do so, at first, the charge particles are weighted at the grid points to obtain the charge and current densities, as the source of the Maxwell's equations. To prevent a self-force, same weighting algorithm for both densities and forces is employed as disused in (Buneman, 1993). In this approach, the volumetric weight regarding (i, j, k) is $(1 - dx)(1 - dy)(1 - dz)$, and in regard to $(i + 1, j + 1, k + 1)$ is $dx \times dy \times dz$. For a particle labeled as n at a position (x, y, z) , we define dx, dy, dz and cx, cy, cz as follow:

$$i = x(n), j = y(n), k = z(n) \quad (2.15a)$$

$$dx = x(n) - i \quad (2.15b)$$

$$dy = y(n) - j \quad (2.15c)$$

$$dz = z(n) - k \quad (2.15d)$$

and

$$cx = 1 - dx \quad (2.16a)$$

$$cy = 1 - dy \quad (2.16b)$$

$$cz = 1 - dz \quad (2.16c)$$

As shown in Figure 2.1, the interpolated force of electric field at (x, j, k) due to the x component is shown by $F_{\text{ex}}(x, j, k)$ and is as following:

$$F_{\text{ex}}(x, j, k) = E_x(i, j, k) + [E_x(i + 1, j, k) - E_x(i, j, k)]dx \quad (2.17)$$

where

$$E_x(i, j, k) = \frac{E_x(i + \frac{1}{2}, j, k) + E_x(i - \frac{1}{2}, j, k)}{2} \quad (2.18a)$$

$$E_x(i + 1, j, k) = \frac{E_x(i + \frac{3}{2}, j, k) + E_x(i + \frac{1}{2}, j, k)}{2} \quad (2.18b)$$

Therefore we have

$$2F_{\text{ex}}(x, j, k) = E_x(i + \frac{1}{2}, j, k) + E_x(i - \frac{1}{2}, j, k) + [E_x(i + \frac{3}{2}, j, k) - E_x(i - \frac{1}{2}, j, k)]dx \quad (2.19)$$

The interpolated forces due to E_x at $(x, j + 1, k)$, $(x, j, k + 1)$, and $(x, j + 1, k + 1)$ are

$$2F_{\text{ex}}(x, j + 1, k) = E_x(i + \frac{1}{2}, j + 1, k) + E_x(i - \frac{1}{2}, j + 1, k) + [E_x(i + \frac{3}{2}, j + 1, k) - E_x(i - \frac{1}{2}, j + 1, k)]dx \quad (2.20a)$$

$$2F_{\text{ex}}(x, j, k + 1) = E_x(i + \frac{1}{2}, j, k + 1) + E_x(i - \frac{1}{2}, j, k + 1) + [E_x(i + \frac{3}{2}, j, k + 1) - E_x(i - \frac{1}{2}, j, k + 1)]dx \quad (2.20b)$$

$$2F_{\text{ex}}(x, j + 1, k + 1) = E_x(i + \frac{1}{2}, j + 1, k + 1) + E_x(i - \frac{1}{2}, j + 1, k + 1) + [E_x(i + \frac{3}{2}, j + 1, k + 1) - E_x(i - \frac{1}{2}, j + 1, k + 1)]dx \quad (2.20c)$$

respectively. Therefore, the interpolated forces due to the E_x at (x, y, k) , $(x, y, k + 1)$, and (x, y, z) , are

$$F_{\text{ex}}(x, y, k) = F_{\text{ex}}(x, j, k) + [F_{\text{ex}}(x, j + 1, k) - F_{\text{ex}}(x, j, k)]dy \quad (2.21a)$$

$$F_{\text{ex}}(x, y, k + 1) = F_{\text{ex}}(x, j, k + 1) + [F_{\text{ex}}(x, j + 1, k + 1) - F_{\text{ex}}(x, j, k + 1)]dy \quad (2.21b)$$

$$F_{\text{ex}}(x, y, z) = F_{\text{ex}}(x, y, k) + [F_{\text{ex}}(x, y, k + 1) - F_{\text{ex}}(x, y, k)]dz \quad (2.21c)$$

respectively. In regard to the forces $F_{\text{ey}}(x, y, z)$, $F_{\text{ez}}(x, y, z)$, $F_{\text{bx}}(x, y, z)$, $F_{\text{by}}(x, y, z)$, and $F_{\text{bz}}(x, y, z)$ related to the E_y , E_z , and B_x , B_y , and B_z the presented scheme can be followed.

2.3.5 Field update

The space-time-centering FDTD scheme is used in the TRISTAN which is second-order accurate in space and time. A fourth-order accurate scheme for the Maxwell curl equations ($\nabla \times \vec{E}$ and $\nabla \times \vec{B}$) is also implemented in the TRISTAN code, which is important in reducing the numerical instabilities (Greenwood et al., 2004)

2.3.5.1 Magnetic field update

The Yee lattice, shown in Figure 2.1, confirms that the rotation of electric field \vec{E} around a surface is equal to the negative change of magnetic flux \vec{B} through that surface and the current density through the remarked surface subtracted from the rotation of magnetic field \vec{B} around it is equal to the change of electric flux \vec{E} through that surface. In the TRISTAN, the current density \vec{J} will be applied to the Ampere equation after the particles pushing. The change of \vec{B} is expressed as (Eq. 2.6):

$$\frac{\partial \vec{B}}{\partial t} = c[\vec{i}(\frac{\partial E_y}{\partial z} - \frac{\partial E_z}{\partial y}) + \vec{j}(\frac{\partial E_z}{\partial x} - \frac{\partial E_x}{\partial z}) + \vec{k}(\frac{\partial E_x}{\partial y} - \frac{\partial E_y}{\partial x})] \quad (2.22)$$

Thus,

$$\begin{aligned} \frac{B_x^{t+\Delta t/2}(i, j + \frac{1}{2}, k + \frac{1}{2}) - B_x^{t-\Delta t/2}(i, j + \frac{1}{2}, k + \frac{1}{2})}{\Delta t} = \\ c[\frac{E_y^t(i, j + \frac{1}{2}, k + 1) - E_y^t(i, j + \frac{1}{2}, k)}{\Delta z} - \\ \frac{E_z^t(i, j + 1, k + \frac{1}{2}) - E_z^t(i, j, k + \frac{1}{2})}{\Delta y}] \end{aligned} \quad (2.23)$$

The updated form of B_y , and B_z can be obtained by the same procedures.

$$\begin{aligned} \frac{B_y^{t+\Delta t/2}(i + \frac{1}{2}, j, k + \frac{1}{2}) - B_y^{t-\Delta t/2}(i + \frac{1}{2}, j, k + \frac{1}{2})}{\Delta t} = \\ c \left[\frac{E_z^t(i + 1, j, k + \frac{1}{2}) - E_z^t(i, j, k + \frac{1}{2})}{\Delta x} - \right. \\ \left. \frac{E_x^t(i + \frac{1}{2}, j, k + 1) - E_x^t(i + \frac{1}{2}, j, k)}{\Delta z} \right] \end{aligned} \quad (2.24)$$

and

$$\begin{aligned} \frac{B_z^{t+\Delta t/2}(i + \frac{1}{2}, j + \frac{1}{2}, k) - B_z^{t-\Delta t/2}(i + \frac{1}{2}, j + \frac{1}{2}, k)}{\Delta t} = \\ c \left[\frac{E_x^t(i + \frac{1}{2}, j + 1, k) - E_x^t(i + \frac{1}{2}, j, k)}{\Delta y} - \right. \\ \left. \frac{E_y^t(i + 1, j + \frac{1}{2}, k) - E_y^t(i, j + \frac{1}{2}, k)}{\Delta x} \right] \end{aligned} \quad (2.25)$$

2.3.5.2 Electric field update

As the magnetic fields, the densities, the displacements and velocities of the particles change, the electric fields must be updated according to Maxwell's equations. The vector formula is Eq. 2.6a.

$$\frac{\partial \vec{E}}{\partial t} = c \left[\vec{i} \left(\frac{\partial B_z}{\partial y} - \frac{\partial B_y}{\partial z} \right) + \vec{j} \left(\frac{\partial B_x}{\partial z} - \frac{\partial B_z}{\partial x} \right) + \vec{k} \left(\frac{\partial B_y}{\partial x} - \frac{\partial B_x}{\partial y} \right) \right] \quad (2.26)$$

Hence, the electric fields components are advanced as:

$$\begin{aligned} \frac{E_x^{t+\Delta t}(i + \frac{1}{2}, j, k) - E_x^t(i + \frac{1}{2}, j, k)}{\Delta t} = \\ c \left[\frac{B_z^{t+\Delta t/2}(i + \frac{1}{2}, j + \frac{1}{2}, k) - B_z^{t+\Delta t/2}(i + \frac{1}{2}, j - \frac{1}{2}, k)}{\Delta y} - \right. \\ \left. \frac{B_y^{t+\Delta t/2}(i + \frac{1}{2}, j, k + \frac{1}{2}) - B_y^{t+\Delta t/2}(i + \frac{1}{2}, j, k - \frac{1}{2})}{\Delta z} \right] \end{aligned} \quad (2.27a)$$

$$\begin{aligned} \frac{E_y^{t+\Delta t}(i, j + \frac{1}{2}, k) - E_y^t(i, j + \frac{1}{2}, k)}{\Delta t} = \\ c \left[\frac{B_x^{t+\Delta t/2}(i, j + \frac{1}{2}, k + \frac{1}{2}) - B_x^{t+\Delta t/2}(i, j + \frac{1}{2}, k - \frac{1}{2})}{\Delta z} - \right. \\ \left. \frac{B_z^{t+\Delta t/2}(i + \frac{1}{2}, j + \frac{1}{2}, k) - B_z^{t+\Delta t/2}(i - \frac{1}{2}, j + \frac{1}{2}, k)}{\Delta x} \right] \end{aligned} \quad (2.27b)$$

and

$$\begin{aligned} & \frac{E_z^{t+\Delta t}(i, j, k + \frac{1}{2}) - E_z^t(i, j, k + \frac{1}{2})}{\Delta t} = \\ & c \left[\frac{B_y^{t+\Delta t/2}(i + \frac{1}{2}, j, k + \frac{1}{2}) - B_y^{t+\Delta t/2}(i - \frac{1}{2}, j, k + \frac{1}{2})}{\Delta x} - \right. \\ & \left. \frac{B_x^{t+\Delta t/2}(i, j + \frac{1}{2}, k + \frac{1}{2}) - B_x^{t+\Delta t/2}(i, j - \frac{1}{2}, k + \frac{1}{2})}{\Delta y} \right] \end{aligned} \quad (2.28)$$

The current density is calculated and subtracted from the rotation of the magnetic field subsequent to the particles pushing.

2.3.5.3 Forth-order accurate for the curl operator

The forth-order accurate approximation for the Maxwell's curl equations includes altering the discretization scheme for the spatial derivatives in the FDTD method. The standard FDTD approximation based on the Yee lattice (Figure 2.1) is second-order accurate. Therefore, to update the B_z at the center of Figure 2.4, $\nabla \times \vec{E}$ is approximated based on the E_x and E_y presented in green as:

$$\vec{k} \cdot (\nabla \times \vec{E})_{i+1/2, j+1/2, k} = \frac{E_{y, i+1, j+\frac{1}{2}, k} - E_{x, i+\frac{1}{2}, j+1, k} - E_{y, i, j+\frac{1}{2}, k} + E_{x, i+\frac{1}{2}, j, k}}{\Delta} + O(\Delta^2) \quad (2.29)$$

here $\Delta x = \Delta y = \Delta z = \Delta$ is considered. The operator may also be estimated using those values presented in “red” as

$$\vec{k} \cdot (\nabla \times \vec{E})_{i+1/2, j+1/2, k} = \frac{E_{y, i+2, j+\frac{1}{2}, k} - E_{x, i+\frac{1}{2}, j+2, k} - E_{y, i-1, j+\frac{1}{2}, k} + E_{x, i+\frac{1}{2}, j-1, k}}{3\Delta} + O(\Delta^2) \quad (2.30)$$

or those presented in “blue” as

$$\begin{aligned} \vec{k} \cdot (\nabla \times \vec{E})_{i+1/2, j+1/2, k} &= \frac{1}{6\Delta} \\ & [E_{y, i+2, j-\frac{1}{2}, k} + E_{y, i+2, j+\frac{3}{2}, k} - E_{x, i+\frac{3}{2}, j+2, k} - E_{x, i-\frac{1}{2}, j+2, k} \\ & - E_{y, i-1, j+\frac{3}{2}, k} - E_{y, i-1, j-\frac{1}{2}, k} + E_{x, i-\frac{1}{2}, j-1, k} + E_{x, i+\frac{3}{2}, j-1, k}] \\ & + O(\Delta^2) \end{aligned} \quad (2.31)$$

All of the above expression are second-order accurate and a linear set of them is then second-order accurate. We approximate the curl operator by C_1 times Eq. 2.30 plus C_2 times Eq. 2.31 plus $(1 - C_1 - C_2)$ times Eq. 2.29. The suitable values of C_1 and C_2 are as $C_1 \leq 0$ and $C_2 = 0$ or $C_2 = 2K_1$, as discussed in Greenwood et al. (2004). The set $C_1 = C_2 = 0$ reduces to the FDTD approximation based on the standard Yee lattice. Here, we use $C_1 = -\frac{1}{8}$, $C_2 = 0$ which causes a fourth-order accurate for the spatial derivatives (Greenwood et al., 2004).

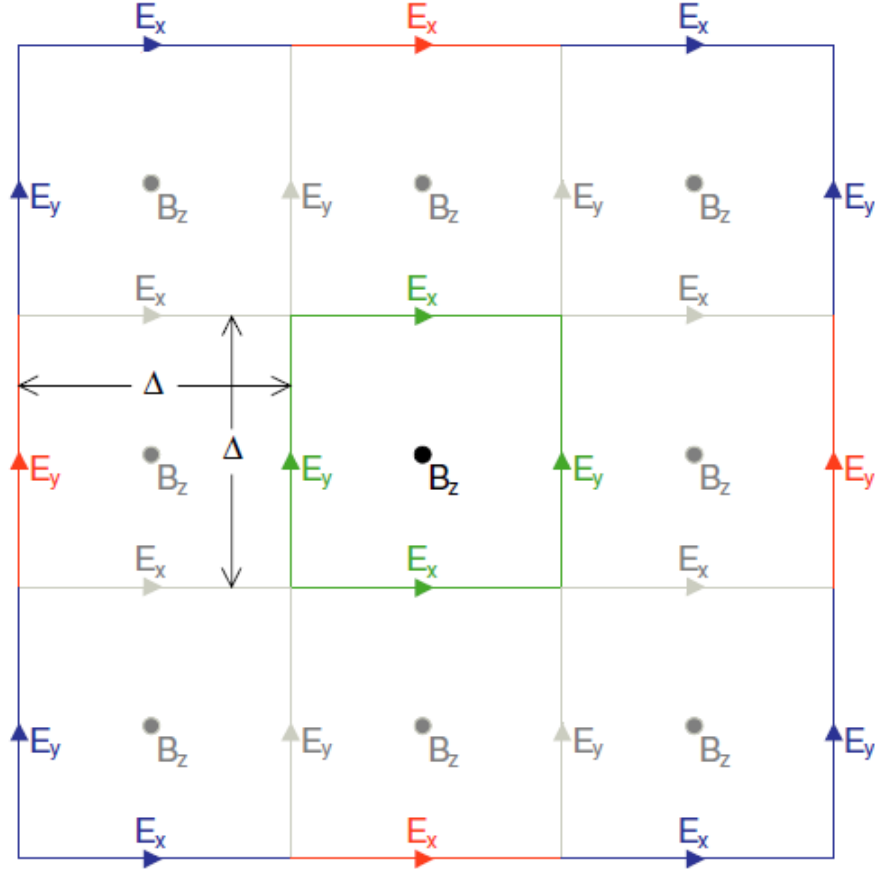


FIGURE 2.4: The electric and magnetic components as presented in Yee lattice in green, and other possibilities which are shown in red and blue. Source: Greenwood et al. (2004).

2.3.6 Parallelization

For the MPI parallelization, the domain decomposition in the TRISTAN code is as follow: primary decomposition, dividing the physical domain between the processors and define a sub-domain for each processor, and secondary decomposition, discretization on the sub-domain of each processor. Due to the using of the finite difference method in approximation of the governing equations, each processor needs some guard cells. Also, when a particle transfers from one processor to the another one, the communication

between the processor is handled via the guard cells. To have the load balance, each sub-domain includes roughly equal number of particles, and number of grid points are same for all of the sub-domains. The implemented algorithm of MPI parallelization is based on the method discussed in Wang et al. (1995).

In each dimension, a sub-domain left and right boundaries are as x_l and x_r and the grid point index are as i_l , i_r , respectively. Here $i_l = \text{integer}(x_l/\delta_{\text{cell}})+1$, $i_r = \text{integer}(x_r/\delta_{\text{cell}})$, δ_{cell} is the cell length. The i_l and i_r mean the grid point indexes on the main physical domain. In each processor, there is also the local indexing for the fields to calculate the fields locally. As explained before, due to the using of the finite difference, in each dimension there are some guard cells based on the employed finite difference method, are defined ig_l and ig_r . Therefore, for each processor, in each dimension, the number of the grid points are bounded between $i_l - ig_l$ to $i_r + ig_r$.

Figure 2.5 shows the main loop of the parallel TRISTAN code. It contains three major subroutines. Mover to move the particles, Deposit to calculate the current - charge density, and Field Pusher for calculate \vec{E} and \vec{B} . In the MPI implementation, the main calculation in Mover, Deposit, and Field Pusher are performed locally. In each loop, communication between the processors are done via the guard cells. There are three major subroutines to handle the communications: Particle Passing, Fields Passing, and Current Passing (blue boxes in Figure 2.5). In the adopted version of the TRISTAN used in this thesis, periodic boundary condition is used in the y and z -direction. however, x -direction is not periodic. The physical periodic boundary conditions in yz -plane are routinely implemented via the communications routines.

Fields Passing

Fields Passing is implemented to communicate the \vec{E} and \vec{B} fields between the processors and also the physical periodic boundary conditions is implemented in this routine. The \vec{E} and \vec{B} fields in this routine are calculated by using the guard cells. The number of the guard cells depends on the finite difference scheme. After calculating the fields in the guard cells on each processor, the communication between the neighboring processor for the three direction x , y , and z is done in a loop over the directions.

DO n = 1,3 for the dimensions

Calculate the fields at left (front: down) and right (rear: up) guard cells

Send left (front: down) and right (rear: up) information to left (front: down) and right (rear: up) processor

Receive the information from the right (rear: up) and left (front: down) processor

Update the fields at the guard cells

ENDDO

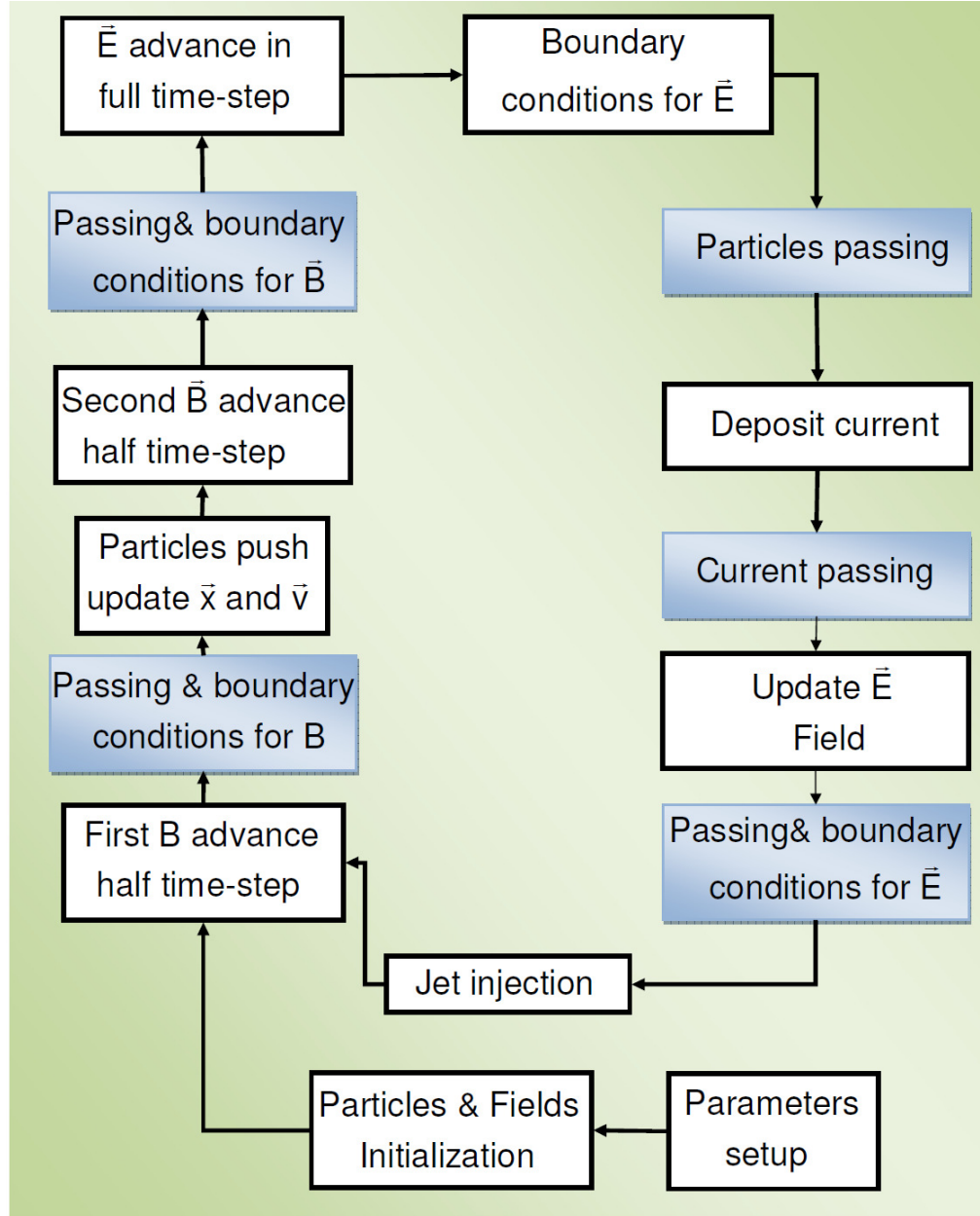


FIGURE 2.5: A time step cycle of modified TRISTAN code. Blue boxes show the parallel parts.

Current Passing

Current Passing do the communication regard the current-charge densities. It calculates the densities at the guard cells and send the information to the proper processor. This routine works as follow:

DO n = 1,3 for the dimensions

Calculate the densities at left (front: down) and right (rear: up) guard cell surfaces

Send left (front: down) and right (rear: up) information to left (front: down) and right (rear: up) processor

Receive the information from the right (rear: up) and left (front: down) processor
 Update the densities and guard cell surfaces
 ENDDO

Particle Passing

The particles communication between the processor is done via the Particle Passing. It peak up the particles that move outward of each processor domain: left (front: down) and right (rear: up). Then send them to the right (rear: up) and left (front: down) proper processor.

DO n = 1,3 for dimensions
 DO np = 1, nparticle for all particles
 Peak up the particles that move out of the processors domain
 Pack the left (front: down)-going particles
 Send to the left (front: down) processors
 Receive from the right (rear: up) processors
 Unpack the particles at the left (front: down) processors
 Pack the right (rear: up)-going particles
 Send to the right (rear: up) processors
 Receive from the left (front: down) processors
 Unpack the particles at the right (rear: up)processors
 ENDDO
 ENDDO

Performance

To examine the performance of our 3D parallel TRISTAN code, the following test is performed. The test is directed on a domain with 1024 cells in the x direction, and 128 cells in the y and z directions. There are 12 particles per cell per species for the ambient plasma, for a total of 330 million particles. Number density of particles in the jet is $0.67n_a$, where n_a is the number density of particles in ambient plasma. The ambient and jet ion-electron has the mass ratio 20. The electron skin depth, $\lambda_{ce} = c/\omega_{pe}$, is 5Δ , where c is the speed of light, ω_{pe} is the electron plasma frequency, and Δ is the grid size. The electron and ion thermal velocity in the ambient plasma are $0.05c$ and $0.05c/\sqrt{m_i/m_e}$, respectively. The time step is $\Delta t\omega_{pe} = 0.025$. In the simulation, a flat jet which fills the computational domain in the transverse directions is injected at $x = 25\Delta$ in the positive x -direction. The relativistic beam bulk velocity is initially $\beta_{0j} = 0.9798$, and the jet electrons and ions have thermal velocities $0.01c$ and $0.01c/\sqrt{m_i/m_e}$, respectively. Radiating boundary condition is used on the surfaces at x_{\min} and x_{\max} based on the

TABLE 2.1: System A supercomputer on the KDK computer system at Research Institute for Sustainable Humanosphere, Kyoto University. Source: [Research Institute for Sustainable Humanosphere, Kyoto University](#).

Specifications	Machine Number of Nodes Performance Total Memory Capacity Network Topology Bisection Bandwidth	Cray XC40 1,800 5.48 PFlops 196.9 TB Dragonfly 13.5 TB/sec
Node Specifications	Processor (Core) Performance Memory Interconnect	1 ($1 \times 68 = 68$) 3.05 TFlops 96GB+16GB Aries
Processor Specifications	Processor Architecture Clock Number of Cores Performance	Intel Xeon Phi KNL x86-64 1.4 GHz 68 3.05 TFlops
High-speed auxiliary storage	System name Total capacity I/O performance	Cray DataWarp 230 TB 200 GB/sec

Lindman's condition ([Lindman, 1975](#)). Periodic boundary condition is applied for all other boundaries ([Buneman, 1993](#)). The results of a similar setup will be discussed in Chapter 3.

In this analysis, the total calculation time, and communication time are measured in the main loop of the code. The measured time is the average time between the all used processors. In the analysis, we have used 3D configuration for the processors as $N_x \times N_y \times N_z$. Whereas the jet is propagating in the x -direction, to have the load balance during the simulation we need to set $N_x = 1$, and $N_y = N_z$. The performance of the code is tested on Cray XC40 supercomputer. The detail of the System A supercomputer on the KDK computer system at Research Institute for Sustainable Humanosphere, Kyoto University is shown in Table 2.1. We use the Cray MPI Fortran compiler to execute our code.

Two quantities are measured to evaluate the performance of the code: efficiency η which accounts for the results of communication overhead and load imbalance and speedup S .

They are defined as follows:

$$S = \frac{T_4}{T_p} \quad (2.32a)$$

$$\eta = \frac{4T_4}{N_p T_p} \quad (2.32b)$$

here N_p is the number of processors, T_4 and T_p is the total time for four processors and N_p processors, respectively.

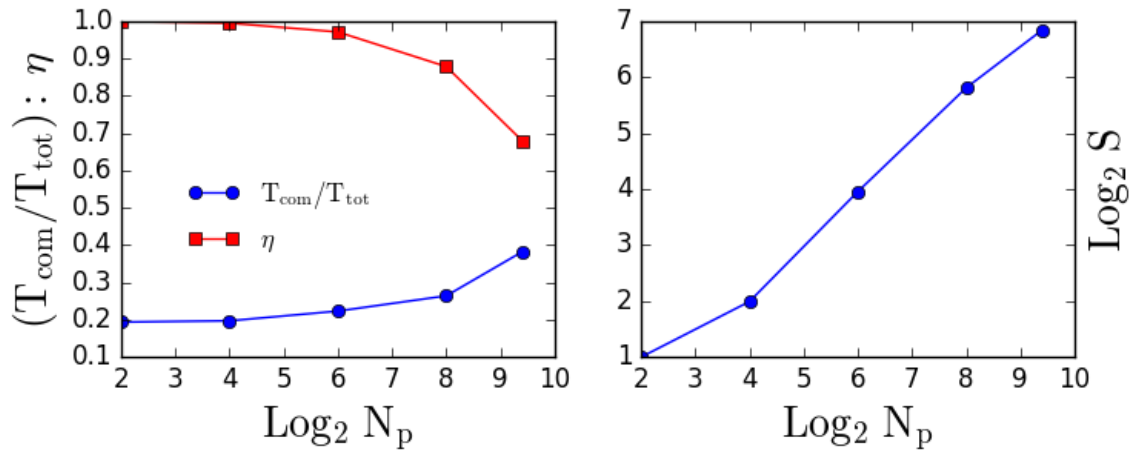


FIGURE 2.6: TRISTAN code performance for fixed-sized problem as a function of number of processors N_p . Shown are (Left): Parallel efficiency and the communication time $T_{\text{com}}/T_{\text{tot}}$ as a function of N_p , (Right): Speedup as a function of N_p .

The speedup, efficiency, and the ratio of $T_{\text{com}}/T_{\text{tot}}$ are shown in Figure 2.6 as a function of processor number of processors. By dividing the calculation between the increasing number pf processors, the speed of calculation increases significantly. When the problem in loaded on $N_p = 512$, the speed up reaches around 128 relative to the $N_p = 4$, as shown in Figure 2.6, right panel. However, when we increase number of the processors, naturally the communication time will increase. Therefore, the communication time increase as number of the processors increase, as shown in Figure 2.6, left panel. This increase in the communication time affects the efficiency, and it decreases as number of the processors increases. In our simulation, the jet is propagating in x -direction. Therefore, the important part of communication is in x -direction, which can be removed by the uses configuration $1 \times N_y \times N_z$. For the this setup, when the simulation is loaded over 512 processors, the communication time reaches around 30 % of computation time which decreases the efficiency to 70 %, Figure 2.6, left panel.

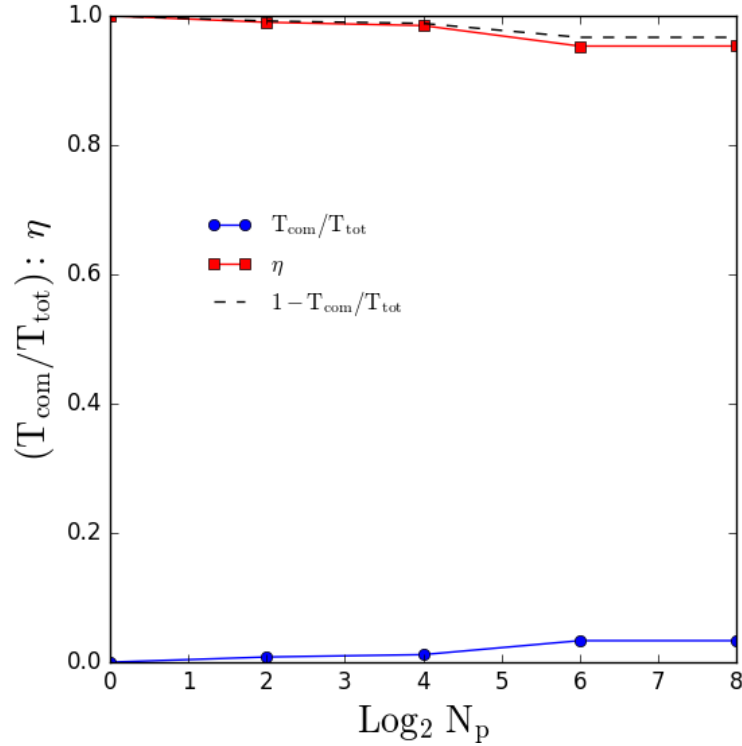


FIGURE 2.7: TRISTAN code performance for scale-sized problem as a function of number of processors N_p . Shown are: Parallel efficiency and the communication time $T_{\text{com}}/T_{\text{tot}}$ as the function of N_p . The black dashed line shows the line corresponding to the $\eta = 1 - T_{\text{com}}/T_{\text{tot}}$.

As the second step, we examine the efficiency and communication time with using the weak scaling analysis. For this kind of analysis, the problem size in each processor is fixed, and the total problem size increase as number of the processors increase. In our test setup, the simulation parameters are as describe in previous analysis, and each processor has a domain as $256 \times 32 \times 32$ grid points. When the problem is performed using 256 processors, the global domain has $256 \times 512 \times 512$ grid points. The efficiency and communication time for this is shown in Figure 2.7. We have load balance for $1 \times N_y \times N_z$ setup, and the efficiency reach around 95% just because of the communication between the processors. It can be proved as we can see $\eta = T_1/T_p \approx 1 - T_{\text{com}}/T_{\text{tot}}$.

Chapter 3

Fields generation in relativistic jet-ambient interactions

On the basis of TRISTAN PIC code, we have analyzed the Weibel instability driven by a relativistic electron-ion jet propagating into an unmagnetized ambient electron-ion plasma. The analysis is focused on the ion contribution in the instability, considering the earliest evolution in shock formation. Simulation results demonstrate that the Weibel instability is responsible for generating and amplifying the small-scale, fluctuating, and dominantly transversal magnetic fields. These magnetic fields deflect particles behind the jet front both perpendicular and parallel to the jet propagation direction. Initially, the incoming electrons respond to field fluctuations growing as the result of the Weibel instability. Therefore, the electron current filaments are generated and the total magnetic energy grows linearly due to the mutual attraction between the filaments, and downstream advection of the magnetic field perturbations. When the magnetic fields become strong enough to deflect the much heavier ions, the ions begin to get involved in the instability. Subsequently, the linear growth of total magnetic energy decreases because of opposite electron-ion currents and topological change in the structure of magnetic fields. The Ion current filaments are then merged and magnetic field energy grows more slowly at the expense of the energy stored in ion stream. It has been clearly illustrated that the ion current filaments extend through a larger scale in the longitudinal direction, while extension of the electron filaments is limited. Hence, the ions form current filaments that are the sources of deeply penetrating magnetic fields. The results also reveal that the Weibel instability is further amplified due to the ions streaming, but on a longer time scale. Our simulation predictions are in valid agreement with those reported in the literature. The current chapter is based on a article as: **K. Ardaneh**, D. Cai, K.-I. Nishikawa. [Amplification of Weibel instability in the relativistic beam-plasma interactions due to ion streaming](#). *New Astronomy*, 2014, Volume 33, pp. 1-6.

3.1 Introduction

Collimated streams of plasma with speeds close to the speed of light, commonly referred to as relativistic jets, exist in some high-energy astrophysical systems, e.g., PWNe, GRBs, and AGNs. The relativistic jets interact with the ISM and then excite external shocks including a FS and RS. A similar scenario is also evidenced in shocks of SNRs. In this interaction, the distribution of particles is extremely anisotropic and this distribution is unstable to several plasma instabilities, such as the electrostatic Buneman instability (Buneman, 1958) and the electromagnetic Weibel instability (Weibel, 1959). In relativistic shocks, the Weibel instability has the largest growth rate and will dominate the interaction (Medvedev and Loeb, 1999, Califano et al., 2002, Hededal and Nishikawa, 2005).

The Weibel instability was first introduced by Weibel (1959) for the non-relativistic plasma with the two different temperatures in two directions. Later, Fried (1959) introduced a similar instability as filamentation for two-stream of cold plasmas. To show a simple picture of the Weibel instability, we consider the protons (ions) at rest, and just consider moving of the electrons. We assumed they are moving along the x -axis (as illustrated in Figure 3.1) with a velocity $\vec{v} = \pm \vec{v}$ and equal number of particles in opposite directions along the x -axis which assure that the net current is zero). In the next stage, a minute magnetic field fluctuation is introduced as $\vec{B} = \vec{j} B_y \cos(kz)$. Due to the Lorentz force, $-e\vec{v} \times \vec{B}$, the electron trajectories are deflected which results in: the electrons moving to the up will concentrate in a layer indicated by an upward blue arrow, and those moving to the down in a layer indicated by a downward blue arrow (Figure 3.1). Thus, current sheaths form which appear to increase the initial magnetic field fluctuation.

The Weibel instability has attracted a lot of attention as a plausible mechanism which can generate strong small-scale magnetic fields in initially unmagnetized plasmas (Medvedev and Loeb, 1999, Brainerd, 2000, Pruet et al., 2001, Gruzinov, 2001, Spitkovsky, 2008a) and subsequently accelerates particles (Silva et al., 2003, Frederiksen et al., 2004). This instability has been studied analytically (Yoon and Davidson, 1987, Medvedev and Loeb, 1999, Tautz and Schlickeiser, 2006, Achterberg and Wiersma, 2007, Petri and Kirk, 2007), numerically (Silva et al., 2003, Frederiksen et al., 2004, Nishikawa et al., 2003, 2005), and also in laboratory experiments (Medvedev, 2007), where it has been known as the precursor to the formation of astrophysical shocks of GRBs and SNRs. On the basis of PIC simulation of the relativistically counter-streaming jets, in the case of electron-positron plasmas, energy stored in the anisotropy of the particles distribution will be transferred to the magnetic field energy and leads to the exponential growth of magnetic field. Following this stage, the Weibel instability saturates and the magnetic field

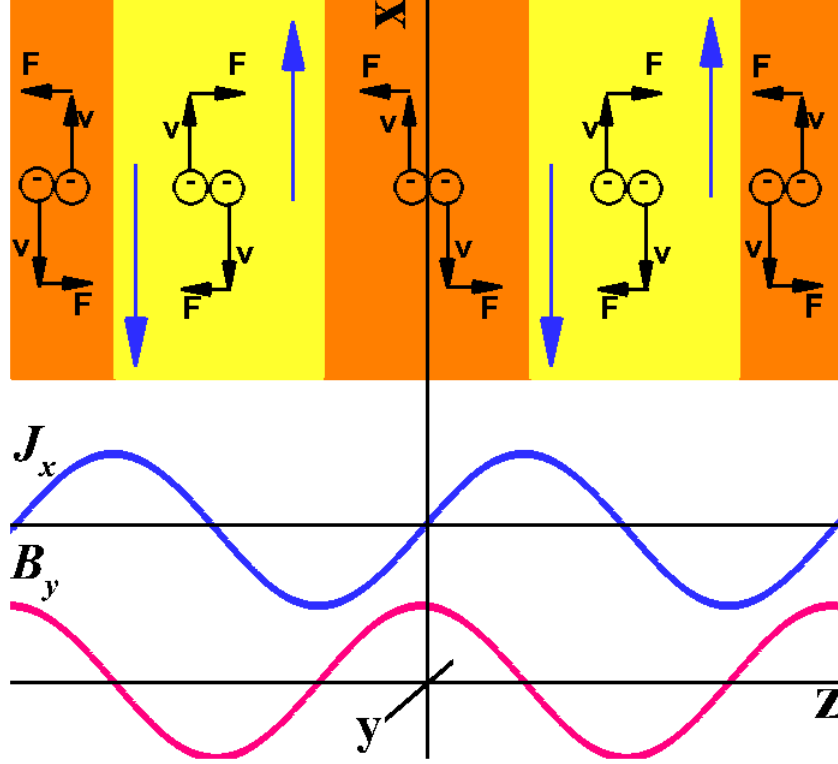


FIGURE 3.1: A simple illustration of the Weibel instability. Adopted based on the [Medvedev and Loeb \(1999\)](#).

energy reaches a quasi-steady level. [Fonseca et al. \(2002\)](#) reported that the generated magnetic field energy density grows to about 15% of the initial kinetic energy density, in consent with the values derived from GRB afterglows ([Panaitescu and Kumar, 2002](#)). Regarding electron-ion plasmas, the ion dynamics and acceleration have been discussed in the relativistic unmagnetized shocks ([Frederiksen et al., 2004](#), [Spitkovsky, 2008a,b](#), [Martins et al., 2009](#)). These studies demonstrate that ion Weibel instability is indeed very effective at deciding the shock transitions in an unmagnetized plasma.

Whereas anisotropy of the particles distribution is the origin of the Weibel instability, by injecting a relativistic particle jet into the background plasma from one side (left in our simulation) this instability can also be excited. This setup is the most similar model for external GRBs, and SNRs shocks. Compared with counter-streaming jets, in this procedure the evolution of the Weibel instability can be investigated in a more realistic spatial way including motion of the jet front. Further, the jet to ambient density ratio can be changed easily. In this chapter, we study via a linear kinetic treatment and

3D PIC simulation the Weibel instability associated with a relativistic jet propagating into an unmagnetized plasma. The domain size and experiment time are larger than [Nishikawa et al. \(2003, 2005\)](#) works to include the ion contribution in the instability. Based on the water-bag approximation ([Bret et al., 2005](#), [Bret, 2009](#), [Bret et al., 2010](#)) an analytical solution is derived for Weibel instability. The instability threshold maps show that Weibel instability will come about for the small values of the jet perpendicular temperature, with respect to the direction of the jet propagation, in a wide range of jet-to-ambient density ratio. Increasing the jet perpendicular temperature demands large enough density ratio for the unstable situations. Moreover, for any given jet forward momentum and density ratio, increasing the jet perpendicular temperature will noticeably narrow the region of unstable wave numbers and significantly suppress the Weibel instability. Regarding the simulation results, temporal evolution of total magnetic energy shows that the incoming electrons initially respond to field fluctuations due to the Weibel instability. In this manner, the electron current filaments will be generated and the total magnetic energy increases linearly as a result of the mutual attraction between the filaments, and downstream advection of the magnetic field perturbations. Therefore, the magnetic fields become strong enough to deflect the much heavier ions. When ions participate in the instability, the linear growth of instability diminishes because of opposite electron-ion currents and topological change in the structure of magnetic fields. The ion current filaments are then merged and magnetic field energy grows more slowly at the expense of the energy stored in ion flow. The results clearly illustrate that ion filaments are the origins of profoundly penetrating magnetic field structures. Also, it has been shown that the Weibel instability is further amplified due to the ions streaming, although in a longer time scale. Simulation results (growth rates and spatial scale of filaments) are validated with those obtained from linear analysis.

3.2 Linear analysis

The thorough linear analysis of the system including a relativistic jet and ambient plasma under arbitrary orientation of the wave vector \vec{k} with respect to the direction of the jet propagation can be found in [Bret et al. \(2005, 2010\)](#). In this section we only review the purely transverse Weibel instability. Our linear analysis is based on the full set of collisionless Vlasov-Maxwell equations in which the one-particle distribution function f_n evolves according to the relativistic Vlasov equation ([Petri and Kirk, 2007](#)):

$$\left[\frac{\partial}{\partial t} + \vec{v}_n \cdot \nabla + q_n \left(\vec{E} + \frac{\vec{v}_n}{c} \times \vec{B} \right) \cdot \nabla_p \right] f_n = 0 \quad (3.1)$$

where \vec{E} and \vec{B} are the electric and magnetic fields. We choose the standard notation $(t, \vec{r}, \vec{v}, \vec{p}, m_n, q_n)$ for the time, position, 3-velocity, 3-momentum, mass and charge of a particle of species n , respectively. Separating the particle distribution function into an unperturbed part and an infinitesimal perturbation, $f_n = f_{n0} + \delta f_n$, and considering the unperturbed part for n th species spatially uniform, $f_{n0}(\vec{r}, \vec{p}) = n_n \varphi_n(\vec{p})$, one can obtain the following dispersion relation for the transverse electromagnetic perturbations propagating along y -direction (Bret et al., 2005, 2010):

$$0 = 1 - \frac{c^2 k^2}{\omega^2} + \sum_n \frac{\omega_{pn}^2}{\omega^2} \left[\int d^3 \vec{p} \frac{p_x}{\gamma} \frac{\partial}{\partial p_x} + \int d^3 \vec{p} \frac{p_x^2}{\gamma^2} \frac{k}{m\omega - k p_y / \gamma} \frac{\partial}{\partial p_y} \right] \varphi_n(\vec{p}) \quad (3.2)$$

here $\gamma = (1 + p^2/m^2 c^2)^{1/2}$, $\omega_{pn} = (4\pi n_n q_n^2 / m_n)^{1/2}$, and $\vec{k} = \vec{j}k$ denote the Lorentz factor, plasma frequency, and wave vector, respectively. To elucidate the detailed characteristics of the Weibel instability as the source of electromagnetic fields generation in relativistic jet-ambient interactions, we assume that jet particles initially move with momentum p_0 (correspond to $mc\gamma_0\beta_0$ in the next section) along the x -direction and are thermally distributed along the y -direction such as $-p_{jth} \leq p_y \leq p_{jth}$. Additionally, for particles in the ambient plasma we suppose $p_x = 0$, and $-p_{ath} \leq p_y \leq p_{ath}$. The jet and ambient plasmas are considered cold along the z -direction. Hence, the distribution function is given by

$$\varphi_n(\vec{p}) = \frac{1}{2p_{nth}} \delta(p_x - p_{n0}) [H(p_y + p_{nth}) - H(p_y - p_{nth})] \delta(p_z) \quad (3.3)$$

for $n = j, a$

where $H(x)$ is the Heaviside step function with $H(x < 0) = 0$ and $H(x \geq 0) = 1$, and $\delta(x)$ is the delta function. Hereafter the time is normalized to $1/\omega_{pe}$, space to the electron skin depth $\lambda_{ce} = c/\omega_{pe}$, and particle momentum to the corresponding mc . The dimensionless form of a variable, such as T , is shown by T^* . Making use of the distribution function in Eq. (3.3), after some straightforward but lengthy calculations, Eq. (3.2) results in the following expression for growth rate of the electron species:

$$\Gamma^{*4} - \Gamma^{*2} \left\{ k^{*2} (1 + \beta_{jth}^2) + \frac{\eta}{\gamma_0} \frac{\beta_0^2}{\beta_{jth}^2} - \frac{\eta}{\gamma_0} \left[\frac{\beta_0^2}{\beta_{jth}^2 (1 - \beta_{jth}^2)} - \xi_j \right] + \frac{\xi_a}{\gamma_{ath}} \right\} \\ + k^{*2} \beta_{jth}^2 \left\{ k^{*2} - \frac{\eta}{\gamma_0} \left[\frac{\beta_0^2}{\beta_{jth}^2 (1 - \beta_{jth}^2)} - \xi_j \right] + \frac{\xi_a}{\gamma_{ath}} \right\} = 0 \quad (3.4)$$

where η is the jet density contrast, n_j/n_a , and the usual relativistic definitions $\gamma_{ath} = (1 + \beta_{ath}^2)^{-1/2}$, $\beta_{ath} = p_{ath}^*/\gamma_{ath}$, $\gamma_0 = (1 + \beta_0^2 + \beta_{jth}^2)^{-1/2}$, $\beta_{jth} = p_{jth}^*/\gamma_0$, $\beta_0 = p_0^*/\gamma_0$ are accompanied by the definition $\xi_j = (1/2\beta_{jth}) \ln[(1 + \beta_{jth})/(1 - \beta_{jth})]$ for the jet, and a similar term for the ambient plasma, ξ_a , by $jth \rightarrow ath$. It is also utilized that Weibel

instability is aperiodic, i.e., $\Re\omega = 0$ and $\Im\omega = \Gamma$.

The condition of marginal stability can be determined by setting $\Gamma^* = 0$. Therefore, the unstable range of wave numbers is given by

$$0 \leq k^{*2} \leq k_c^{*2} = \frac{\eta}{\gamma_0} \left[\frac{\beta_0^2}{\beta_{\text{jth}}^2 (1 - \beta_{\text{jth}}^2)} - \xi_j \right] - \frac{\xi_a}{\gamma_{\text{ath}}} \quad (3.5)$$

Looking over Eq. (3.5) discloses that the necessary condition for $k_c^{*2} \geq 0$ corresponds to

$$\frac{\beta_0^2}{\beta_{\text{jth}}^2} \geq \left[-\frac{\gamma_0}{\eta\gamma_{\text{ath}}} \xi_a + \xi_j \right] (1 - \beta_{\text{jth}}^2) \quad (3.6)$$

When Eq. (3.6) is satisfied, and wave number is in the range specified by Eq. (3.5), the growth rate of the Weibel instability is given by

$$\begin{aligned} \Gamma^{*2} = \frac{1}{2} \{ [k^{*2} \beta_{\text{jth}}^2 + \frac{\eta}{\gamma_0} \frac{\beta_0^2}{\beta_{\text{jth}}^2} - (k_c^{*2} - k^{*2})]^2 + 4k^{*2} \beta_{\text{jth}}^2 (k_c^{*2} - k^{*2}) \}^{1/2} \\ - \frac{1}{2} [k^{*2} \beta_{\text{jth}}^2 + \frac{\eta}{\gamma_0} \frac{\beta_0^2}{\beta_{\text{jth}}^2} - (k_c^{*2} - k^{*2})] \end{aligned} \quad (3.7)$$

The mode with the largest growth rate predominates in the time evolution. Some straightforward algebra gives the wave number of the fastest growing mode as follow

$$k_{\text{max}}^{*2} = \frac{1}{(1 - \beta_{\text{jth}}^2)^2} \{ (1 + \beta_{\text{jth}}^2) [\sqrt{C^2 - Ck_c^{*2}(1 - \beta_{\text{jth}}^2)} - C] + k_c^{*2}(1 - \beta_{\text{jth}}^2) \} \quad (3.8)$$

where $C = \eta\beta_0^2/\gamma_0\beta_{\text{jth}}^2$. Substituting k_{max}^{*2} into Eq. (3.7), the corresponding maximum growth rate then can be determined. Based upon the Eq. (3.6), the instability threshold map for different forward momentum is presented in Figure 3.2a. In Figures 3.2, the effective perpendicular temperature, relative to the direction of the jet propagation, is defined by

$$T_{\text{jth}}^* = \frac{K_B T_{\text{jth}}}{mc^2} = \frac{1}{mc^2} \langle \frac{p_{yj}^2}{\gamma m} \rangle = \frac{1}{mc^2} \int d^3\vec{p} \frac{p_y^2}{\gamma m} \varphi_j(\vec{p}) = \frac{1}{2} \gamma_0 [1 + (\beta_{\text{jth}}^2 - 1) \xi_j] \quad (3.9)$$

here, K_B is the Boltzmann constant. In Figure 3.2a the region of (η, T_{jth}^*) parameter space above the instability threshold map corresponds to the unstable situations. It is clear that increasing the jet perpendicular temperature, T_{jth}^* , requires sufficiently large density contrast for unstable situations (e.g., $\eta > 0.4$ for $T_{\text{jth}}^* = 0.1$ and $p_0^* = 2$). Therefore, for any given jet forward momentum and density contrast this instability can be completely stabilized by increasing the T_{jth}^* to adequately large values (e.g., $T_{\text{jth}}^* > 0.1$ for $\eta = 0.4$ and $p_0^* = 2$). One more significant characteristic of the instability threshold map is the asymptotic limit for large jet forward momentum which overlaps the $p_0^* = 10$

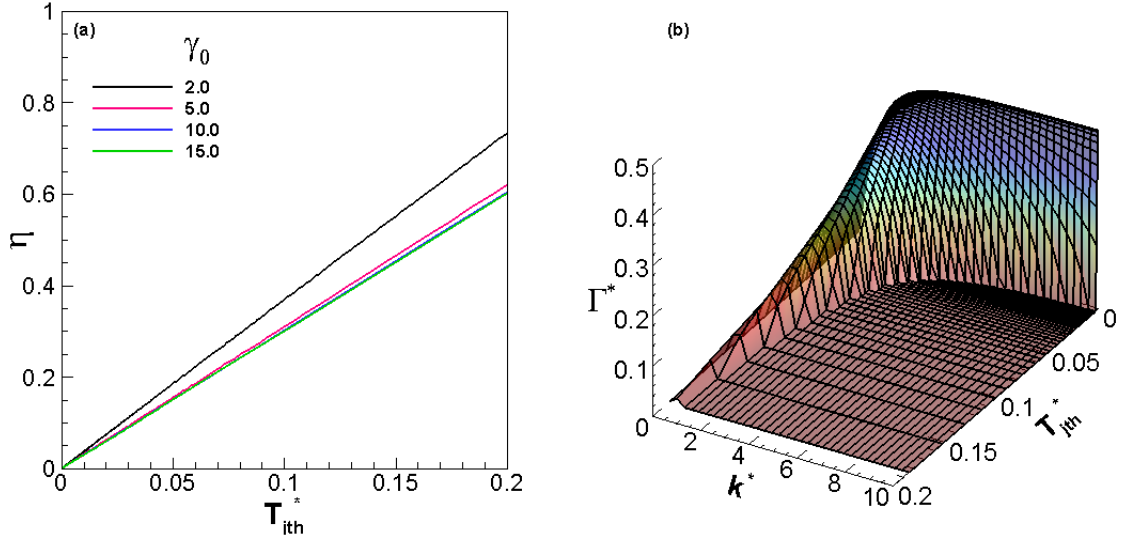


FIGURE 3.2: (a) Weibel instability threshold map for different jet forward momentums, and (b) the Weibel instability growth rate vs wave number and perpendicular temperature for $\gamma_0 = 5$ and $\eta = 0.67$.

threshold map. Shown in Figure 3.2b is the growth rate versus wave number and perpendicular temperature, when $p_0^* = 5$ and $\eta = 0.67$ (according to the simulation setup in next section). As one can see, increasing the jet perpendicular temperature will obviously suppress the Weibel instability and noticeably narrow the region of unstable wave numbers. Further, enhancement of the jet perpendicular temperature diminishes the maximum growth rate, and the corresponding wave number shifts to the smaller values. Physical interpretation of these figures is as follow. The electrons are scattered by the magnetic field turbulences growing because of the Weibel instability. When the scattered electrons travel through the first surfaces, the filaments carrying a current $I \approx \pi R^2 c n_j e \beta_0$ will be generated, where R is the filament radius. Subsequently, the filaments merge together caused principally by attraction force between the filaments, with a maximum value of $F_{\text{max}} = \varepsilon_0 e^2 \beta_0^2 R n_j / 2$ exerting on an electron. However, thermal pressure resulting from the transverse energy spread opposes the merging of filaments, $F_P \approx 3 n_a V K_B T_{\text{jth}} / 2 R$, V volume of the filament. The Weibel instability will grow only if attraction force between the filaments exceeds the pressure force ($\eta > 3 V K_B T_{\text{jth}} / \varepsilon_0 e^2 \beta_0^2 R^2$). Therefore, increasing the jet perpendicular temperature demands sufficiently large density contrast to dominate the attraction against the thermal pressure. Further, for any given density contrast, increasing the perpendicular temperature amplifies the thermal pressure and subsequently decreases the growth rate of the Weibel instability.

3.3 Parameters setup for PIC simulation

In this work, my simulation is performed using a modified version of the TRISTAN code (Buneman, 1993), which is a massively parallel, fully relativistic, particle-in-cell code for many applications in the astrophysical plasma (Nishikawa et al., 2003, 2005, 2009). The basic features of TRISTAN code is discussed in Chapter 2. The experiment is directed on a domain with 1024 cells in the x direction, and 164 cells in the y and z directions. There are 12 particles per cell per species for the ambient plasma, for a total of 330 million particles. Number density of particles in the jet is $0.67n_a$, where n_a is the number density of particles in ambient plasma. The ambient and jet ion-electron has the mass ratio 20. The electron skin depth, $\lambda_{ce} = c/\omega_{pe}$, is 5Δ , where c is the speed of light, ω_{pe} is the electron plasma frequency, and Δ is the grid size. The electron and ion thermal velocity in the ambient plasma are $0.1c$ and $0.1c/\sqrt{m_i/m_e}$, respectively. The time step is $\Delta t\omega_{pe} = 0.025$. In the simulation, a flat jet which fills the computational domain in the transverse directions is injected at $x = 25\Delta$ in the positive x -direction. The relativistic jet bulk velocity is initially $\beta_{0j} = 0.9798$, and the jet electrons and ions have thermal velocities $0.01c$ and $0.01c/\sqrt{m_i/m_e}$, respectively. Radiating boundary condition is used on the surfaces at x_{\min} and x_{\max} based on the Lindman's condition (Lindman, 1975). Periodic boundary condition is applied for all other boundaries (Buneman, 1993).

3.4 Simulation results

Recently, to simulate Weibel instability, a relativistic plasma stream is launched from one side and reflected from a rigid boundary at the opposite side (Jaroschek et al., 2005, Chang et al., 2008, Spitkovsky, 2008a,b, Martins et al., 2009). This is corresponding method of colliding two counter-streaming identical plasmas but saves one-half of the computational efforts (Chang et al., 2008, Spitkovsky, 2008a,b). However, in the present study by injecting the particles jet into the ambient plasma from the left, the Weibel instability is observed when the incoming particles jet interact with ambient plasma in the computational box. In the present simulation, the evolution of the Weibel instability can be studied in a more realistic way including motion of the jet front. Further, the jet-to-ambient density ratio can be changed easily. This instability leads to the field fluctuations, particles deflections, and current perturbations. In the following this scenario is explained in more detail.

As shown in Figure 3.3, the temporal evolution of the square root of the magnetic energy density (normalized to the initial kinetic energy density of incoming jet) presents different phases. At first the jet electrons are (being lighter than ion) deflected behind

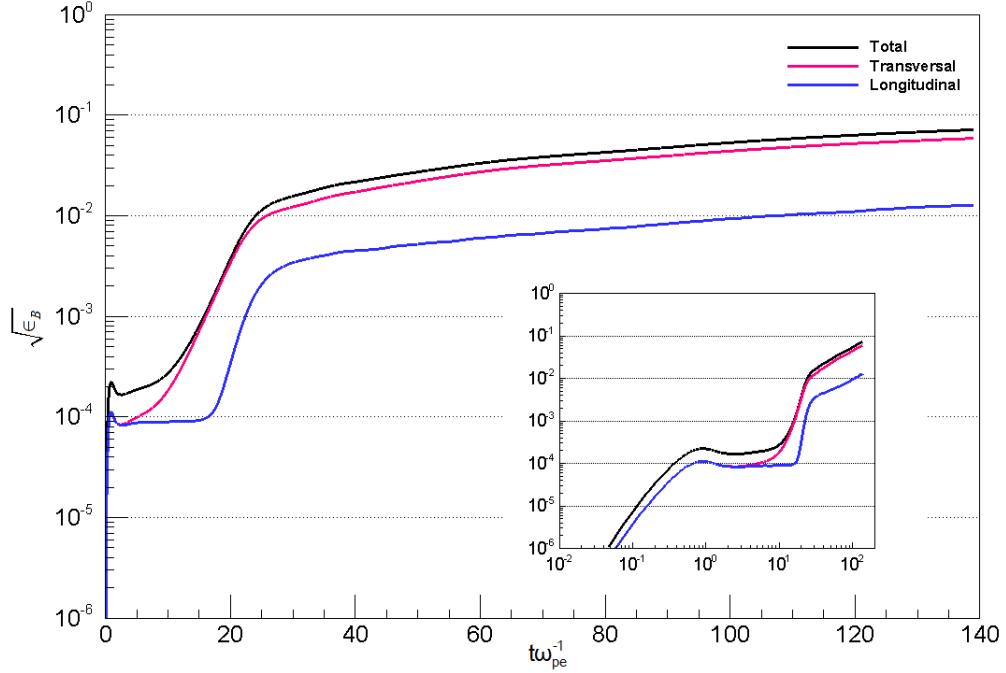


FIGURE 3.3: Time evolution of the square root of the normalized magnetic field energy density. The inset shows a log-log plot of the same data.

the jet front by the magnetic field perturbations growing because of the Weibel instability (Weibel, 1959, Medvedev and Loeb, 1999, Nishikawa et al., 2003, 2005). The deflection of jet electrons is represented in Figures 3.4a, and 3.4b. Clearly the kinetic energy (parallel velocity) of the incoming jet is transferred to the perpendicular deflection by means of the electromagnetic field perturbations (illustrated by transversally averaged in Figure 3.5a) generated by the electron Weibel instability. The transverse acceleration of electrons is accompanied by the deceleration of electrons and for $t = 24.9\omega_{pe}^{-1}$ takes place between $17\lambda_{ce} \leq x \leq 27\lambda_{ce}$. At this time, the strongest acceleration and deceleration occurs around the maximum amplitude of perturbations due to the electron Weibel instability at $x = 24\lambda_{ce}$, as seen in Figure 3.5a.

When the deflected electrons collect into the first surfaces, the filamentary current structures will be generated. As seen in Figure 3.3, the Weibel instability initially grows non-linearly ($2\omega_{pe}^{-1} \leq t \leq 16\omega_{pe}^{-1}$), interpreting as amplification of generated magnetic fields in a small volume (Frederiksen et al., 2004). Physically, the perturbations in current lead to perturbations in magnetic field, which in turn will increase the current inhomogeneity and generate a large number of current filaments. Because of the longitudinal current filaments the magnetic field structures are mainly transversal. According to Ampere's law the current filaments are encircled by approximately azimuthal magnetic fields (illustrated by arrows in Figures 3.7).

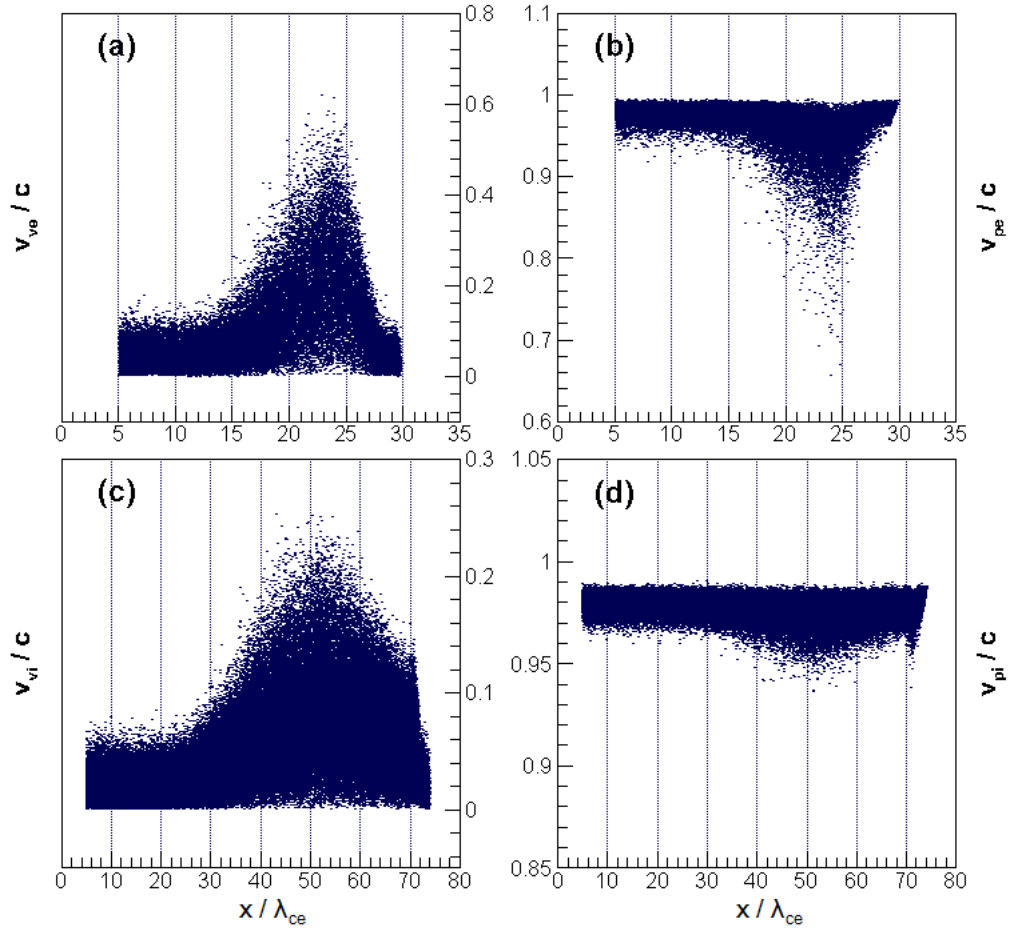


FIGURE 3.4: Distribution of jet particles (a) electrons at $t = 24.9\omega_{pe}^{-1}$ in $x - v_{ve}$ phase space, (b) electrons at $t = 24.9\omega_{pe}^{-1}$ in $x - v_{pe}$ phase space, (c) ions at $t = 69.72\omega_{pe}^{-1}$ in $x - v_{vi}$ phase space, and (d) ions at $t = 69.72\omega_{pe}^{-1}$ in $x - v_{pi}$ phase space. Roughly 20% of the jet particles are randomly selected for these plots. $v_v = (v_y^2 + v_z^2)^{1/2}$, $v_p = v_x$.

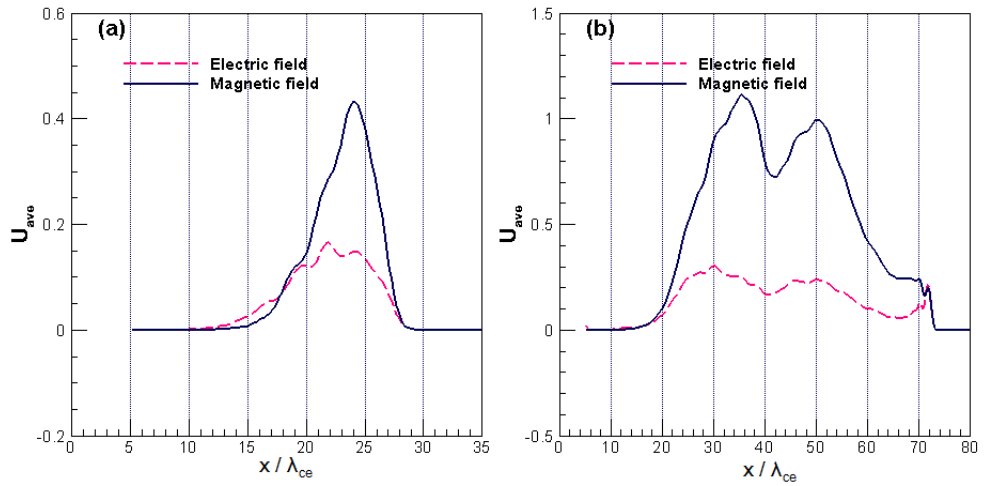


FIGURE 3.5: One dimensional displays of transversally averaged electric and magnetic field energies at (a) $t = 24.9\omega_{pe}^{-1}$, (b) $t = 69.72\omega_{pe}^{-1}$.

As shown in Figure 3.3, the total magnetic field energy enhances more linearly afterwards, caused mainly by mutual attraction between the electron current filaments, downstream advection of the magnetic field fluctuations, and the increase of volume filling factor (Silva et al., 2003, Frederiksen et al., 2004). During this stage ($16\omega_{pe}^{-1} \leq t \leq 26\omega_{pe}^{-1}$), initially randomly elongated electron filaments merge together to construct a more organized, and large scale pattern (Figures 3.6a, and 3.6b). Therefore, the azimuthal magnetic field structures are amplified in strength. When the magnetic fields grow strong enough to deflect the much heavier ions, the ions begin to participate in the instability. A portrait of the ion deflection is depicted in Figures 3.4c, and 3.4d. As seen, the transverse deflection of ion flow for $t = 69.72\omega_{pe}^{-1}$ is between $30\lambda_{ce} \leq x \leq 65\lambda_{ce}$ and strongest deflection takes place around the maximum amplitude of perturbations due to the ion Weibel instability at $x = 50\lambda_{ce}$, Figure 3.5b.

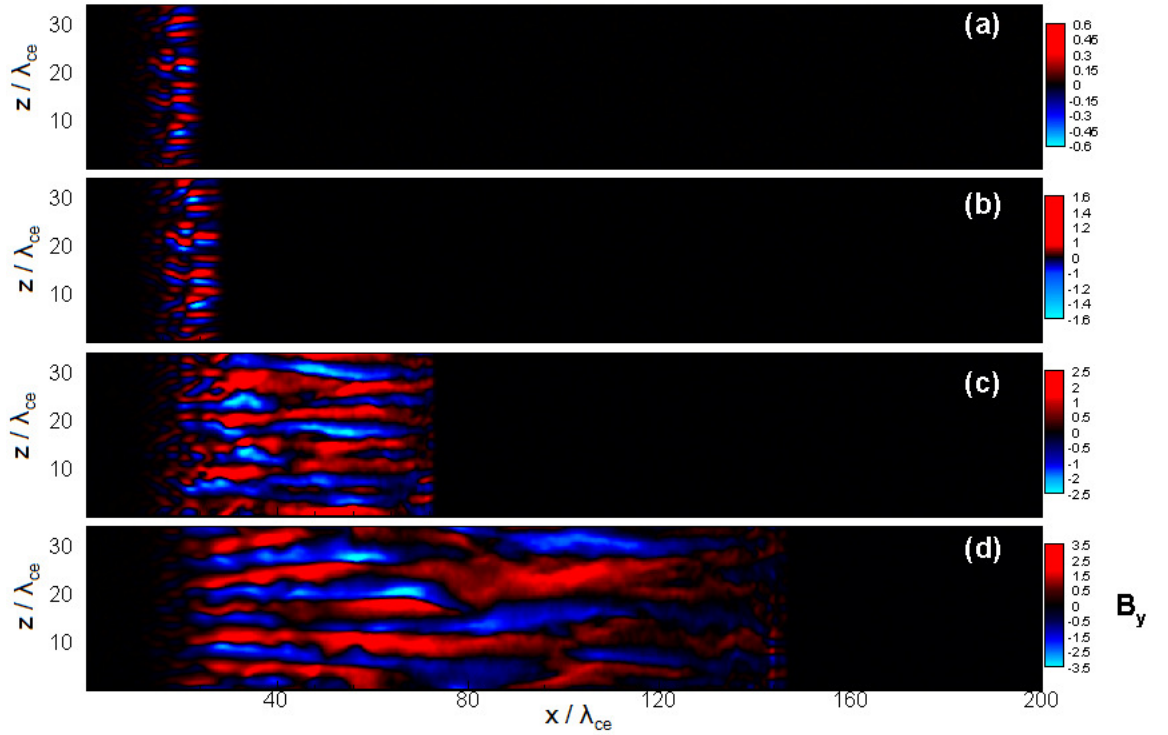


FIGURE 3.6: Time evolution of the Weibel instability in the $x-z$ plane ($y = 16.67\lambda_{ce}$). Transverse magnetic field, B_y , at simulation times (a) $t = 19.92\omega_{pe}^{-1}$, (b) $t = 24.9\omega_{pe}^{-1}$, (c) $t = 69.72\omega_{pe}^{-1}$, (d) $t = 144.4\omega_{pe}^{-1}$.

At the end of first linear stage the magnetic energy density, ϵ_B , reaches about 1% of KE_{0j} for the mass ratio $m_i/m_e = 20$ and initial jet velocity $\beta_{0j} = 0.9798$. Electron currents point into the page and the associated magnetic fields are clockwise while ion currents direct out of the page and the related magnetic fields are counter-clockwise (represented by arrows in Figures 3.7a and 3.7b). Therefore, about $t = 26\omega_{pe}^{-1}$ the growth of magnetic energy diminishes (Figure 3.3) because of opposite electron-ion current filaments and

topological change in the structure of magnetic fields. The drop in the growth rate will happen on a later timescale for larger mass ratios because stronger magnetic fields are required to deflect the heavier ions. The ion filaments are then undergone the same growth process as electron filaments. The proceeded slow growth, for $t > 26\omega_{pe}^{-1}$, indicates the enlargement of the filaments size with time, as shown in Figures 3.6c, and 3.6d. The magnetic field is proportional to the electric current, which in turn increases in inverse proportion to the number of the current filaments. The transverse magnetic fields are more amplified, whereas the total electric current is predominantly divided into fewer but stronger ion filaments, as depicted in Figure 3.7b and Figure 3.8.

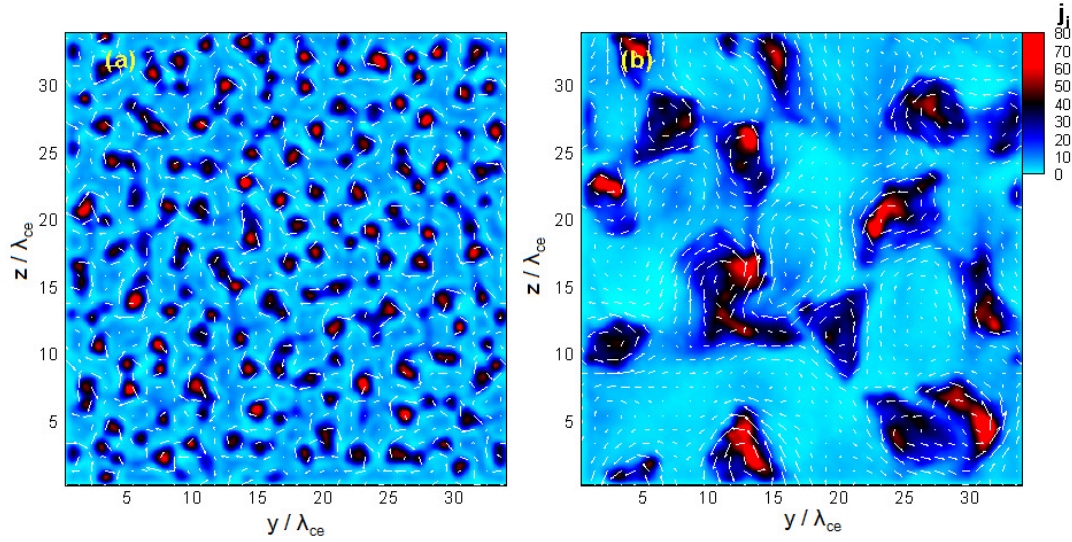


FIGURE 3.7: Longitudinal current density through a transverse section. (a) Electron flux at $x = 25\lambda_{ce}$ and $t = 24.9\omega_{pe}^{-1}$, (b) Ion flux at $x = 83\lambda_{ce}$ and $t = 144.4\omega_{pe}^{-1}$.

As Frederiksen et al. (2004) remarked, when ion current filaments are adequately strong, they will be subjected to Debye shielding by the electrons. The Debye shielding extinguishes the electron filaments, in contrast with the strengthening the ion filaments (Figure 3.8); the high random velocities of the electron population allow the concentrated ion filament to keep preserving strong magnetic fields. In this stage, the residual magnetic field is highly inhomogeneous, seen as an assortment of magnetic field zones or bubbles as called by Silva et al. (2003). These magnetic zones isolate current filaments with opposite polarity (Figure 3.7b).

Validation of these results is examined as follow. The exponential growth of magnetic field can be expressed as:

$$B(t) = B_0 \exp(\Gamma t) \quad (3.10)$$

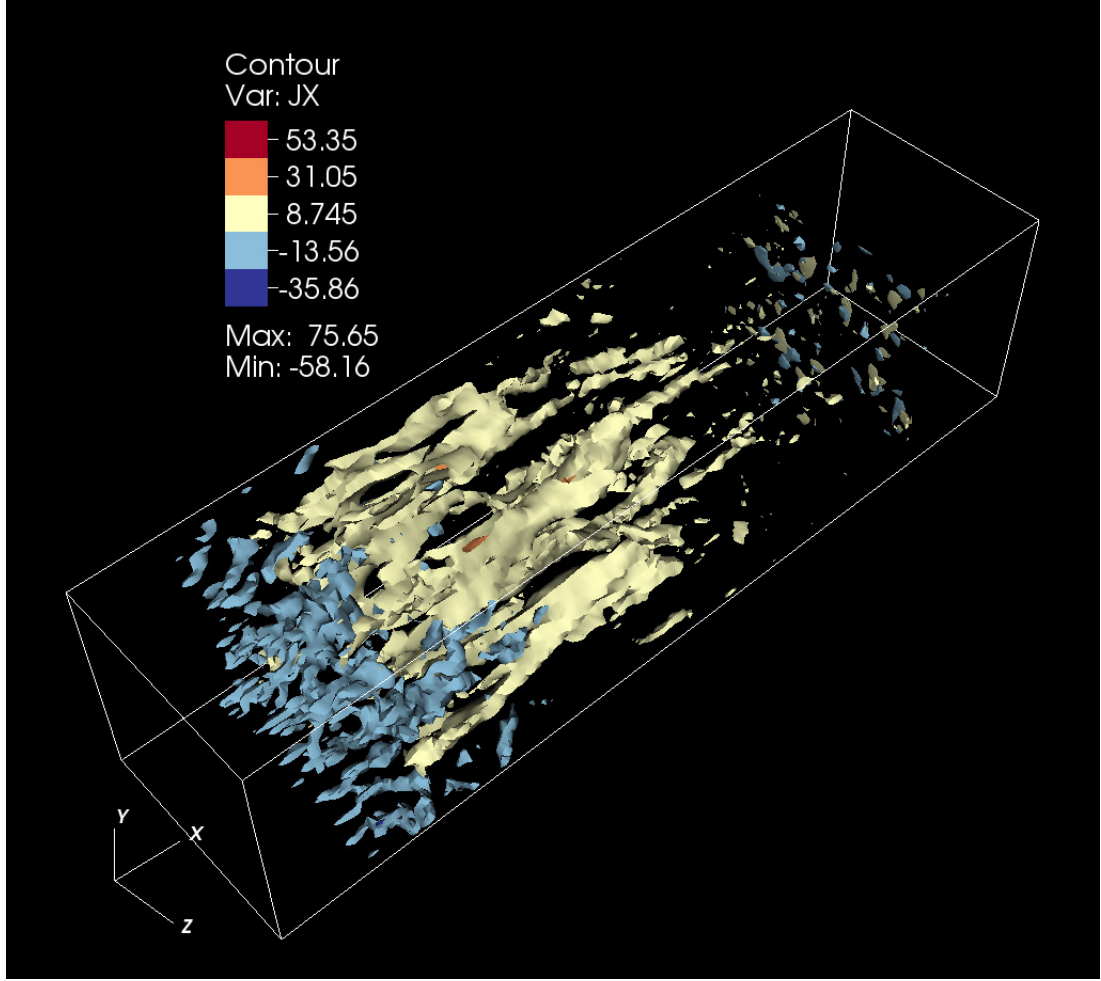


FIGURE 3.8: Longitudinal current density in 3D view. The electron current density (negative) and the ion current density (positive) are shown with two different colors.

Where Γ and t are growth rate and temporal scale, respectively. Using the magnetic energy density formula, $u_b = B^2/\mu_0$, the growth rate can be obtained as:

$$\Gamma = \frac{\ln(u_{B2}/u_{B1})^{1/2}}{t_2 - t_1} \quad (3.11)$$

Using the above formula for two linear segments of Figure 3.3, two exponential growth rates can be found as, $\Gamma_1^* \approx 0.30$ and $\Gamma_2^* \approx 0.02$, respectively. Since the incoming electrons initially respond to the field perturbations and the ions are accelerated afterwards, in the present experiment the exponential growth rates of the electron and ion Weibel instabilities are indeed $\Gamma_e^* \approx 0.30$ and $\Gamma_i^* \approx 0.02$, respectively. $\Gamma_e^* \approx 0.30$ is consistent with the theoretical estimate for electrons as (Medvedev and Loeb, 1999):

$$\Gamma_{\text{emax}}^* \approx \left[\frac{1}{\gamma_0} \left(1 - \frac{2\sqrt{2}}{\gamma_0} \right) \right]^{1/2} \approx 0.30 \quad (3.12)$$

Furthermore, based on Eq. 3.7, the maximum growth rate for the ion Weibel instability is as $\Gamma_{\text{imax}}^* = \sqrt{m_i/m_e} \Gamma_{\text{emax}}^* \approx 0.07$ under the same initial condition. However, in the simulation, the ions contribute in the instability at the later stages when the perpendicular temperature is increased by the electron Weibel instability. Hence, the ion Weibel instability will increase with a smaller growth rate than 0.07 which in this simulation is ≈ 0.02 . The filamentary structures resulting from the electron Weibel instability have diameters about $R_e \approx 8\Delta$, Figure 3.7a. This is in good agreement with the theoretical estimate where $R \approx 1/k_{\text{max}}$ (Medvedev and Loeb, 1999):

$$k_{\text{max}} \approx \frac{1}{2^{1/4}} \lambda_{\text{ce}}^{-1} \left(1 - \frac{3}{\sqrt{2}\gamma_0}\right)^{1/2} \quad (3.13)$$

The size of ion filamentary structures is about $R_i \approx 30\Delta$, Figure 3.7b. In accordance with above equation, ion Weibel instability generates larger filamentary structures by a ratio of $\sqrt{m_i/m_e}$ at a later time, hence $R_i \approx \sqrt{m_i/m_e} R_e \approx 35$. The filaments are elongated along the direction of jet injection (the x -direction). Clearly, the longitudinal extension of the electron filaments is limited, while the ion magnetic filaments extend through a larger scale, as seen in Figures 3.6. Hence, the ion current filaments are the sources of deeply penetrating magnetic field structures.

The nonlinear saturation amplitude of the magnetic field, B_{sat} , i.e., when magnetic field growth stalls, can be determined following the magnetic trapping mechanism (Medvedev and Loeb, 1999). When the magnetic field reaches the value

$$B_{\text{sat}} = \frac{\sqrt{2\mu_0} n^{1/2} m_p^{1/2} \beta_0 c \gamma_0^{1/2}}{1 + \beta_{\text{th}}} \quad (3.14)$$

the free streaming of particles across the magnetic field lines is suppressed. Therefore, electron-ion jets will drive higher levels of saturated magnetic field, by a factor of $\sqrt{m_i/m_e}$, but on a longer timescale since $\Gamma \propto m_p^{-1}$. In order for the saturated magnetic field to examine, I need much longer simulations.

3.5 Conclusions

In this chapter I have studied the role of the ions in the Weibel instability driven by a relativistic electron-ion jet front propagating into an unmagnetized background electron-ion plasma. The jet is injected in the positive x -direction. My analysis was based on a self-consistent, 3D relativistic PIC code. The simulation results illustrate the basic characteristics of the Weibel instability:

1. In the absence of a magnetic field in the ambient plasma, a small scale, fluctuating, and dominantly transversal magnetic field is generated by the Weibel instability.
2. Weibel instability is excited behind the jet front, where current filaments are generated because of the electron-ion density perturbations. The deflection of particles due to the Lorentz force increases as the Weibel instability grows.
3. Temporal evolution of the generated magnetic field demonstrates that Weibel instability is aperiodic, i.e., $\Re\omega = 0$. Therefore, it can be saturated only by nonlinear effects and not by kinetic effects, such as collisionless damping or resonance broadening. Hence the magnetic field can be amplified to very high values locally.

In addition to the above points, the experiment reported upon here reveals the ion effects on the Weibel instability in the relativistic jet-plasma interactions:

1. After the first linear phase in the time evolution of the total magnetic field energy, ion streaming amplifies the Weibel instability and the magnetic fields grow more slowly, showing a second linear stage. Therefore, electron-ion jets will drive higher levels of saturated magnetic field, but on a longer time scale since $\Gamma \propto m_p^{-1}$. Our simulation results have confirmed the theoretical predictions for the exponential growths in the magnetic field energy.
2. Ion current filaments are the sources of profoundly penetrating magnetic field structures. The filaments merge in the downstream direction, with a proportional increase of the magnetic energy. The elementary currents have a complicated 3D structure. The diameter of electron filaments is on the order of the electron skin depth. However, the transverse size of ion structures is larger by a ratio of $\sqrt{m_i/m_e}$.

Chapter 4

Collisionless shocks in relativistic jet-ambient interactions

The course of non-thermal electron ejection in relativistic unmagnetized electron-ion shocks is investigated by performing self-consistent particle-in-cell simulations. The shocks are excited through the injection of a relativistic jet into ambient plasma, leading to two distinct shocks (referred to as the trailing shock and leading shock) and a contact discontinuity. The Weibel-like instabilities heat the electrons up to approximately half the ion kinetic energy. The double layers formed in the trailing and leading edges then accelerate the electrons by ion kinetic energy. The electron distribution function in the leading edge shows a clear, non-thermal power-law tail which contains $\sim 1\%$ of electrons and $\sim 8\%$ of electron energy. Its power-law index is -2.6. The acceleration efficiency is $\sim 23\%$ by number and $\sim 50\%$ by energy and the power-law index is -1.8 for the electron distribution function in the trailing edge. The effect of the dimensionality is examined by comparing the results of three dimensional simulations with those of two-dimensional simulations. The comparison demonstrates that electron acceleration is more efficient in two dimensions. The current chapter is based on the two articles as: (1) **K. Ardaneh**, D. Cai, K.-I. Nishikawa. [Collisionless electron-ion shocks in relativistic unmagnetized jet-ambient interactions: Non-thermal electron injection by double layer](#). *The Astrophysical Journal*, 2016, Volume 827, 124 (15pp). (2) **K. Ardaneh**, D. Cai, K.-I. Nishikawa, B. Lembége. [Collisionless Weibel shocks and electron acceleration in gamma-ray bursts](#). *The Astrophysical Journal*, 2015, Volume 811 (1), 57 (9pp).

4.1 Introduction

Tightly collimated streams of plasma with speeds close to the speed of light, commonly referred to as relativistic jets, are included in some astrophysical systems, e.g., PWNe, GRBs, and AGNs. The relativistic jets propagate through the ambient medium and subsequently excite double shock structures. The acceleration of particles is ubiquitous in astrophysical shocks (Koyama et al., 1995, Eriksen et al., 2011, Masters et al., 2013). Non-thermal emissions from these environments are generally considered as synchrotron or inverse Compton radiations via a power-law distribution of electrons accelerated at shock sides (Tautz and Lerche, 2012).

Charged particles may be accelerated via first-order Fermi acceleration (or diffusive shock acceleration, DSA) in the collisionless shocks. In DSA, particles reflect backward and forward around the shock surface and achieve energy from the magnetohydrodynamics waves (Blandford and Ostriker, 1978, Bell, 1978, Drury, 1983, Blandford and Eichler, 1987, Bell, 2013). However, DSA needs a fraction of particles with kinetic energies beyond of the thermal ones because only these particles are capable of multiple crossings of the shock front and effective scattering by magnetic turbulences. However, this is not apparent in what way the electrons can achieve the threshold energy of DSA. The threshold demands that electrons kinetic energies be equivalent to those of the ions. This is known as the electron injection problem (Balogh and Treumann, 2013).

In the case of a magnetized upstream region, the injection of electrons is considered to be directly associated with the background motional electric field $\vec{E}_0 = -\vec{\beta}_0 \times \vec{B}_0$. The electrons may be accelerated the motional electric field while they gyrate-surf around the shock front. Based on the barrier that reflects the electrons toward the upstream, thus making them capable of repeated energizations, this process is known by several distinct names. If the reflecting barrier has a magnetic source, e.g., the gradient of the magnetic field at the leading edge of the shock, then the acceleration mechanism is known as shock drift acceleration or SDA (Chen and Armstrong, 1975, Webb et al., 1983, Begelman and Kirk, 1990, Park et al., 2012, 2013, Guo et al., 2014). If the barrier has an electrostatic source, e.g., the electrostatic solitary waves appearing at the leading edge of the shock due to Buneman instability (Buneman, 1958), then the process is called shock surfing acceleration or SSA (Lee et al., 1996, Hoshino and Shimada, 2002, Shapiro and Ücer, 2003, Amano and Hoshino, 2009, Matsumoto et al., 2012). Basically, the SSA process acts only in electron-ion shocks because an electrostatic barrier would not be generated if the species have the same inertia.

An interesting question is the following. How does the electron ejection operate in unmagnetized electron-ion shocks? Due to the lack of an upstream motional electric field,

we expect a process other than SDA and SSA. Particle-in-cell (PIC) simulations provide a self-consistent description of particle acceleration in collisionless shocks. Our work has focused on the large-scale PIC simulations of electron injection in unmagnetized relativistic electron–ion shocks. In PIC simulations, the shock waves are usually excited by the so-called injection approach (Hoshino, 2001, Hoshino and Shimada, 2002, Spitkovsky, 2008a,b, Amano and Hoshino, 2009, Martins et al., 2009, Sironi and Spitkovsky, 2011, Sironi et al., 2013, Guo et al., 2014). Using this approach, a high-speed plasma stream is launched from one end of the computational grid and reflected from a rigid boundary at the opposite end. Subsequently, a shock is excited due to interactions between the incoming and reflected streams. Although this method reduces the number of calculations by one-half, it has some disadvantages as well. In this method, the reverse and forward shocks are degenerate (not distinguishable) and the simulations are limited to two identical counters streaming beams. However, we focus on the asymmetric jet–ambient interactions, i.e., interactions of plasmas with different properties that result in two different shocks, that is, a trailing shock (TS) and leading shock (LS), and a contact discontinuity (CD).

In the present work, we have performed a three-dimensional (3D) PIC simulation where a collisionless double shock is created by an unmagnetized relativistic jet propagating into an unmagnetized ambient plasma. In contrast to the injection method, our asymmetric jet–ambient model is more realistic since it avoids an infinitely sharp CD and permits us to appropriately explore the dynamics of the TS and LS for different jet–ambient parameters. Beam–plasma (or jet–ambient) systems are unstable relative to some plasma instabilities, e.g., electrostatic two-stream or Buneman modes (Buneman, 1958), and electromagnetic filamentation (Fried, 1959) or Weibel (Weibel, 1959) modes. Therefore, the unstable spectrum is not less than two-dimensional (2D). Which of these modes will dominate depend on the system characteristics (Bret, 2009). This undoubtedly clears a demand for studies employing methods like ours (Nishikawa et al., 2003, 2005, 2009, 2016, Ardaneh et al., 2014, 2015, Choi et al., 2014), or using asymmetric counter-streaming beams (Niemi et al., 2012, Wieland et al., 2016), because the most unstable modes excited in various setups can generate the totally different shock waves.

Our paper is dedicated to answering five questions. First, how does the double shock structure form in unmagnetized jet–ambient interactions? Second, are the shocks characterized by magnetic or electrostatic forces? Third, what are the main processes responsible for electron injection? Fourth, what is the resulting electron distribution function? Fifth, what is the effect of the dimensionality?

The fluid dynamics of relativistic shocks is presented in Section 4.2. The simulation model and parameters setup are described in Section 4.3. The results of the simulations

are presented in Section 4.4. We conclude with a summary in Section 4.5.

4.2 The fluid dynamics of relativistic shocks

Whenever a fast flow encounters an obstacle which forces the flow to slow down sufficiently, the result of this is a shock. The critical number for the occurrence of a shock is the famous sonic Mach number $M_s = v/c_s$, where v is the velocity of the obstacle relative to the bulk velocity of the flow and c_s is the speed of sound in the medium of the flow. An obstacle moving through a medium always excites compression waves, which propagate through the medium at the speed of sound. If the velocity of the obstacle relative to the flow is subsonic, i.e., $M_s < 1$, the medium has sufficient time to rearrange itself and to dodge around the obstacle. If the velocity is supersonic, i.e., $M_s \geq 1$, the medium has no time to rearrange itself, but gets extremely compressed at the obstacle. This effect is called a shock or shock wave.

The point of the shock wave that is farthest away from the obstacle is called the shock front. It is characterized by a sudden jump in several physical parameters. Most notable is a jump in the flow velocity, which abruptly drops from supersonic to subsonic. Accompanying this is a jump in the temperature, since the kinetic energy of the flow is converted into thermal energy. Yet another jump can be found in the density of the medium. As mentioned above, the medium gets extremely compressed at the shock front, and, although it can disperse again behind the shock, the density still is higher than in the unshocked medium. A shock process is an adiabatic compression and, since entropy is generated at the shock front, an irreversible process. The surface at which the jumps occur is called shock discontinuity. It separates the unshocked medium in front of the shock from the shocked medium behind the shock, which are called upstream and downstream medium, respectively (see Figure 4.1a). In some cases, it is also possible that two shock fronts develop: the FS, which is moving away from the site where the shock was created in forward direction and the RS, which moves in the opposite direction and mostly back towards the site of the shock creation (see Figure 4.1b). Both shocks have their accompanying upstream and downstream region, in which the latter are separated by a so-called CD, i.e., a surface across which there is no particle transport.

4.2.1 Jump conditions for relativistic 90° shock

A shock discontinuity, the surface where the jump in several physical parameters occurs, is indeed a solution of hydrodynamics. However, the hydrodynamic equations are only

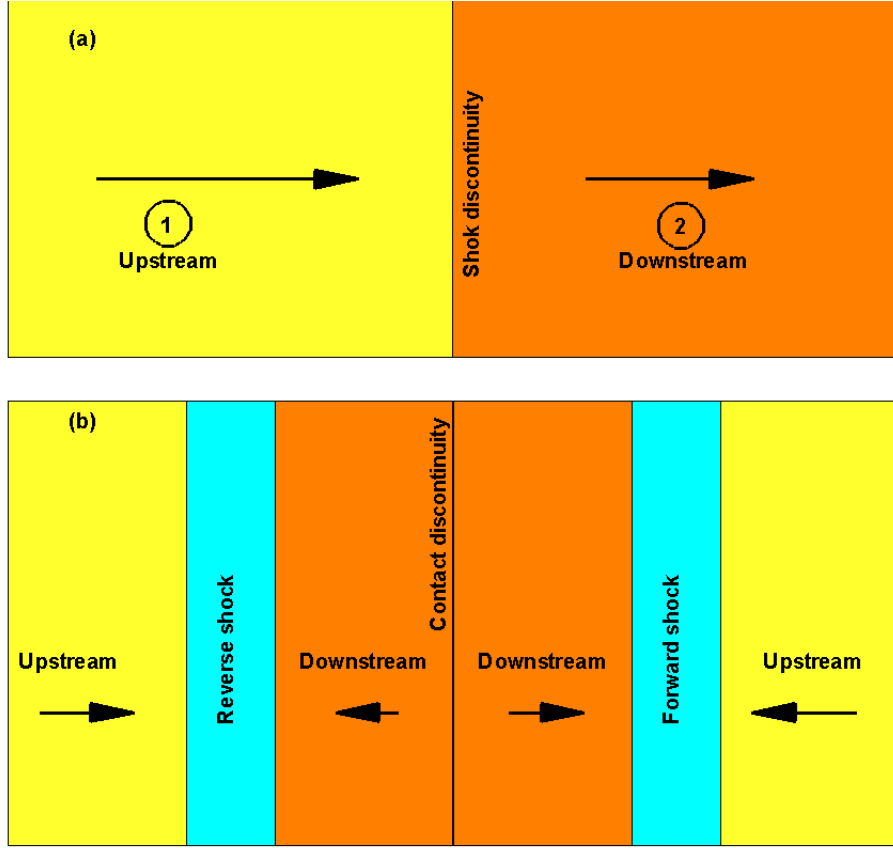


FIGURE 4.1: Illustration of the shock system. (a) illustration of a simple shock structure with the shock discontinuity separating the unshocked upstream medium and the shocked downstream medium drawn in a frame where the shock discontinuity is at rest, and (b) illustration of a double-shock structure with FS moving away from the shock creation site, RS moving back towards the shock creation site and the CD separating the downstream regions of the forward and the RS drawn in a frame where the CD is at rest. Adopted based on the [Zhang and Kobayashi \(2005\)](#), [Zel'dovich and Raizer \(2002\)](#), [Piran \(2003\)](#).

valid on scales where the medium in question can be described as a fluid, i.e., larger than the mean free path for two-body collisions. However, a real shock is thinner than that and, therefore, needs a different description. First of all, a shock front is described by its geometrical shape. Since its width is very thin compared to its tangential extension, it can be considered as a thin, locally flat surface. The vector \vec{n} normal to this surface is called the shock normal. The jump in the physical parameters at the shock front is subject to some conditions which can be derived using the conservation laws for mass, momentum and energy. These conditions are also known as Euler equations. In this section, at first I review the MHD analysis of a relativistic 90° shock propagating into an unmagnetized plasma (Figure 4.1a), and then extend the analysis for the dual shock structures (Figure 4.1b). The present work adopts the notation of [Zhang and Kobayashi \(2005\)](#), where quantities with a single index Q_i denote the value of the quantities Q in the region i in their own rest frame and quantities with double indices Q_{ij} denote the

value of the quantities Q in the region i in the rest frame j . In the following, indices 1, 2, and s refer to the upstream, downstream, and shock frame, respectively. The jump conditions for 90° shocks are solutions of the following none-dimensional MHD conservation equations (Kennel and Coroniti, 1984, Zhang and Kobayashi, 2005):

$$[1 + \sigma_1(1 - Y)]\gamma_{1s}\mu_1^* = \gamma_{2s}\mu_2^* \quad (4.1a)$$

$$[1 + \frac{\sigma_1}{2\beta_{1s}^2}(1 - Y^2)]p_{1s}^*\mu_1^* + \frac{P_1^*}{p_{1s}^*} = p_{2s}^*\mu_2^* + (\frac{n_1}{n_2})\frac{P_2^*}{p_{2s}^*} \quad (4.1b)$$

where $\sigma_1 = B_{1s}^2/(4\pi n_1\mu_1\gamma_{1s}^2)$ is the magnetization, with B_{1s} as the transverse magnetic field, and dimensionless specific enthalpy and Y , as the ratio of shock frame magnetic fields or density (Kennel and Coroniti, 1984, Zhang and Kobayashi, 2005), are defined as

$$\mu_i^* = 1 + (\frac{n_1}{n_i})\frac{\tilde{\Gamma}_i}{\tilde{\Gamma}_i - 1}P_i^* \quad (4.2a)$$

$$Y \equiv \frac{B_{2s}}{B_{1s}} = \frac{N_{2s}}{N_{1s}} = \frac{\gamma_{2s}p_{1s}^*}{\gamma_{1s}p_{2s}^*} = \frac{\gamma_{2s}n_2}{\gamma_{1s}n_1} \quad (4.2b)$$

here P^* denote the dimensionless thermal pressure, $P^* = P/n_1mc^2$, and $\tilde{\Gamma}$ is the adiabatic index. In my simulations the upstream flow is considered a cold plasma, i.e., $P_1^* = 0$, so that $\mu_1^* = 1$. Solving Eq. (4.1a) for μ_2^* and inserting the resulting expression into Eq. (4.1b) leads to the following equation for unmagnetized plasma (Zhang and Kobayashi, 2005):

$$p_{1s}^{*2} = \frac{(\gamma_{21} - 1)(\tilde{\Gamma}\gamma_{21} + 1)^2}{\tilde{\Gamma}(2 - \tilde{\Gamma})(\gamma_{21} - 1) + 2} \quad (4.3a)$$

$$\gamma_{1s}^2 = \frac{(\gamma_{21} + 1)[\tilde{\Gamma}(\gamma_{21} - 1) + 1]^2}{\tilde{\Gamma}(2 - \tilde{\Gamma})(\gamma_{21} - 1) + 2} \quad (4.3b)$$

$$p_{2s}^{*2} = \frac{(\gamma_{21} - 1)(\tilde{\Gamma} - 1)^2}{\tilde{\Gamma}(2 - \tilde{\Gamma})(\gamma_{21} - 1) + 2} \quad (4.3c)$$

$$\gamma_{2s}^2 = \frac{(\gamma_{21} + 1)}{\tilde{\Gamma}(2 - \tilde{\Gamma})(\gamma_{21} - 1) + 2} \quad (4.3d)$$

The corresponding jump condition can then be determined by Eq. (4.2b) as.

$$\frac{n_2}{n_1} = \frac{\tilde{\Gamma}\gamma_{21} + 1}{\tilde{\Gamma} - 1} \quad (4.4)$$

4.2.2 Jump conditions for jet-ambient interaction

Now I consider an unmagnetized jet with Lorentz factor γ_{41} being decelerated by an ambient medium with density n_1 . In such system, a CD and two shock waves propagating

away from the CD into the upstream form. Hence, two shocks and one CD split up the jet and ambient medium into four regions: (1) unshocked ambient, (2) shocked ambient, (3) shocked jet, and (4) unshocked jet. Relative to the CD, the above formalism can easily include the shocks associated with jet-ambient interactions. The speed of the CD can be determined by applying Eq. (4.1b) in the interface of the ambient and jet (Nishikawa et al., 2009). Hence, in the CD rest frame we have

$$\mu_1^* \gamma_{1CD}^2 \beta_{1CD}^2 + P_1^* = \frac{n_4}{n_1} \mu_4^* \gamma_{4CD}^2 \beta_{4CD}^2 + P_4^* \quad (4.5)$$

The jet speed measured in the CD frame and associated Lorentz factor are given by

$$\beta_{4CD} = \frac{\beta_{41} - \beta_{1CD}}{1 - \beta_{41}\beta_{1CD}} \quad (4.6a)$$

$$\gamma_{4CD} = (1 - \beta_{4CD}^2)^{-1/2} \quad (4.6b)$$

In my simulations, the jet and ambient mediums are initially cold plasmas. Hence Eq. (4.5) reduces to

$$\mu_r \gamma_{1CD}^2 \beta_{1CD}^2 = \gamma_{4CD}^2 \beta_{4CD}^2 \quad (4.7)$$

where μ_r is the jet-to-ambient enthalpy ratio. Making use of Eqs. (4.6), after some algebra Eq. (4.7) gives

$$\beta_{1CD} = \frac{\gamma_{41} \mu_r^{1/2}}{\gamma_{41} \mu_r^{1/2} + 1} \beta_{41} \quad (4.8)$$

which is the speed of ambient medium towards the CD, and thus the speed of the CD through the ambient medium. In regard to shocked ambient, once β_{1CD} (γ_{1CD}) is determined from Eq. (4.8), by $\gamma_{21} \rightarrow \gamma_{1CD}$ Eqs. (4.3) can be solved to find the speed of the shocked ambient (FS) in the ambient frame, $\beta_{FS1} = -\beta_{1s}$. The jump condition for the FS is

$$\frac{n_2}{n_1} = \frac{\tilde{\Gamma} \gamma_{1CD} + 1}{\tilde{\Gamma} - 1} \quad (4.9)$$

Concerning the shocked jet (RS), making use of Eq. (4.6a) the speed of CD in the jet rest frame can be calculated $\beta_{CD4} = -\beta_{4CD}$. Under $1 \rightarrow 4$, $2 \rightarrow 3$ and $\gamma_{34} \rightarrow \gamma_{4CD}$ transformations in Eqs. (4.3), we can calculate the speed of the RS in the jet rest frame, $\beta_{RS4} = -\beta_{4s}$. In this region the jump condition becomes

$$\frac{n_3}{n_4} = \frac{\tilde{\Gamma} \gamma_{CD4} + 1}{\tilde{\Gamma} - 1} \quad (4.10)$$

Finally, the speed of the RS in the ambient rest frame is given by

$$\beta_{RS1} = \frac{\beta_{41} - \beta_{RS4}}{1 - \beta_{41}\beta_{RS4}} \quad (4.11)$$

4.3 Simulation model and parameters setup

In our work, an unmagnetized particle jet is injected into an unmagnetized ambient plasma (Nishikawa et al., 2003, 2005, 2009, 2016, Ardaneh et al., 2014, 2015, Choi et al., 2014). Finally, a double shock structure is formed resembling what is schematically illustrated in Figure 4.2. The deceleration of the jet stream by magnetic fluctuations (excited in the beam-plasma interactions) results in a CD and two shock waves that divide the jet and ambient plasmas into four regions: (1) unshocked ambient, (2) shocked ambient, (3) shocked jet, and (4) unshocked jet. Hereafter, the subscripts 1, 2, 3, and 4 refer to the unshocked ambient, shocked ambient, shocked jet, and unshocked jet, respectively. Quantities with a single index ϱ_i indicate the value of quantities ϱ in region i in rest frame i and quantities with double indices ϱ_{ij} show the value of quantities ϱ in region i as seen in rest frame j .

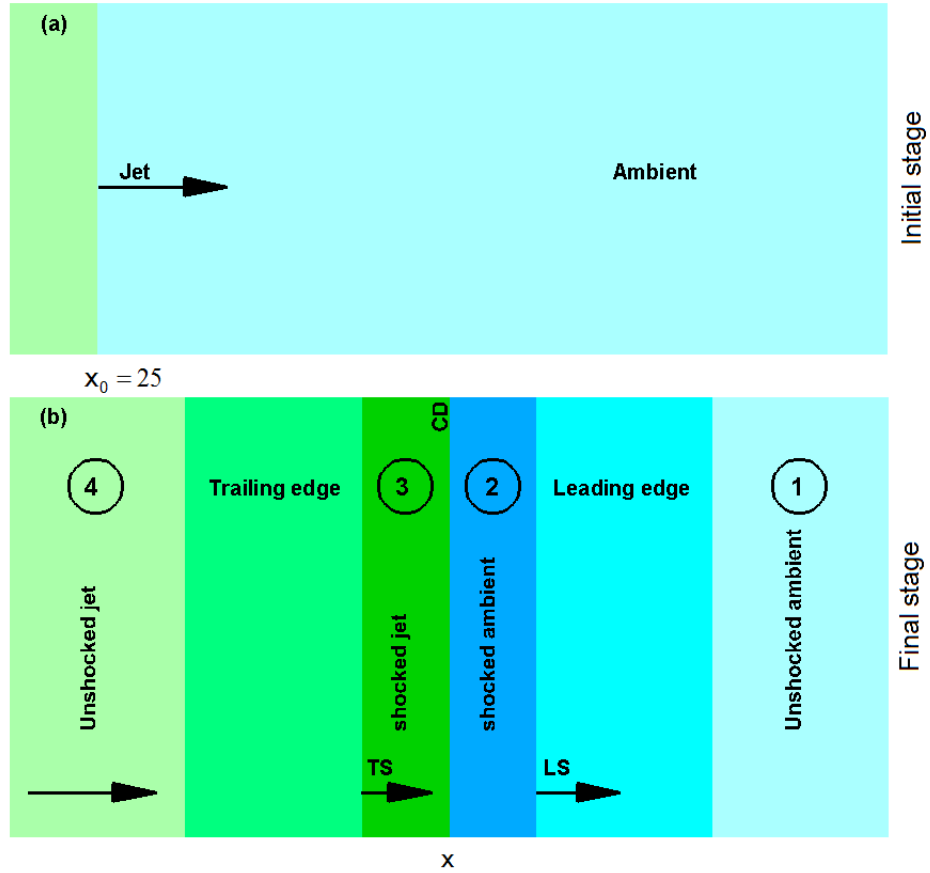


FIGURE 4.2: Illustration of the jet-ambient interaction showing (a) a particle jet being injected into an ambient plasma and (b) the resulting double shock structure. The shocks are named according to Nishikawa et al. (2009).

The code employed in the present work is a modified version of the TRISTAN PIC code (Buneman, 1993). A series of test simulations have already been performed to

establish a numerical code which is stable relative to the numerical self-heating. In the PIC simulations including a cold relativistic plasma beam, a numerical heating instability arises when the beam travels large distances over the numerical grid. The instability is a combination of numerical Cherenkov instability and spurious plasma oscillations (Dieckmann et al., 2006). The latter oscillations are usually excited by coupling between a sideband of the beam mode with the electromagnetic mode. The beam mode has a physical phase speed $\omega/k = v_b$, where v_b is the beam velocity. The beam interaction with the numerical grid, probably through a finite grid instability (Birdsall and Langdon, 1991), excites artificial sidebands that are separated from the beam mode by the frequency modulus $\Delta\omega = 2\pi v_b/\Delta$, where $2\pi v_b/\Delta$ is the grid crossing frequency. One of these sidebands may couple to the electromagnetic mode and results in the artificial obliquely propagating waves that are observed in the PIC simulations (Dieckmann et al., 2006). The growth rate of these waves can be reduced by using a higher-order numerical scheme (Yee, 1966, Dieckmann et al., 2006). Here, the numerical instability is diminished by means of the fourth-order solver for Maxwell's curl equations and a Friedman filter as presented in Greenwood et al. (2004).

The simulation is performed using a computational grid with $(\ell_x, \ell_y, \ell_z) = (8005, 245, 245)$, grid size: $\Delta x = \Delta y = \Delta z = 1$. There are six particles per cell per species for the ambient plasma (\simeq three billions particles per species). The density ratio of the jet-to-ambient is 5/3. Our frame of reference is the ambient where the jet plasma moves to the right in positive x -direction with bulk speed $\beta_{41} = 0.995$ (bulk Lorentz factor $\Gamma_{41} = 10$). The jet fills the whole computational box in the yz -plane and is injected continuously at $x_0 = 25$. The jet plasma is injected with energy distribution in the jet rest frame given by a 3D Maxwell-Jüttner distribution $f(\gamma_4) \propto \gamma_4^2 \beta_4 \exp(-\gamma_4/\theta_4)$ and thermal spread $\theta_4 = (K_B T_e/m_e c^2)_4 = 0.092$ (relativistically hot, $\beta_{th4} = 0.4$). In the ambient medium, the electrons have a thermal spread $\theta_1 = (K_B T_e/m_e c^2)_1 = 12.5 \times 10^{-4}$. In both plasmas, the ions are in thermal equilibrium with the electrons. The m_i/m_e mass ratio used is 16. The system is numerically resolved with five grid cells per electron skin depth, $\lambda_{ce} = 5$, and $\Delta t = 0.01\omega_{pe}^{-1}$, where Δt and ω_{pe} are the time step and the electron plasma frequency, respectively. The surfaces at x_{\min} and x_{\max} are rigid reflecting boundaries for the ambient particles, while they are open boundaries for the jet particles. These surfaces are radiating boundaries for the fields based on Lindman's method (Lindman, 1975). Periodic boundary conditions are applied at all other boundaries for both particles and fields. Hereafter, time is normalized to ω_{pe}^{-1} , space to the λ_{ce} , particle momentum for species s to the corresponding $m_s c$ (e: electron and i: ion), and density to the unshocked ambient density, n_1 . Furthermore, the position x is measured from x_0 .

For the described setup, according to the hydrodynamic jump conditions for jet-ambient interactions (Zhang and Kobayashi, 2005, Nishikawa et al., 2009, Ardaneh et al., 2015),

TABLE 4.1: Parameters of the formed double shock structure.

Parameters of the LS		
Parameter	In region (1)	In region (2)
γ_{ls}	$\gamma_{ls1} = 1.91$	$\gamma_{ls2} = 1.01$
β_{ls}	$\beta_{ls1} = 0.85$	$\beta_{ls2} = 0.17$
n_2/n_1	$n_{21}/n_1 = 16.0$	$n_2/n_{12} = 5.8$
Parameters of the TS		
Parameter	In region (1)	In region (3)
γ_{ts}	$\gamma_{ts1} = 1.38$	$\gamma_{ts3} = 1.03$
β_{ts}	$\beta_{ts1} = 0.68$	$\beta_{ts3} = -0.25$
n_3/n_4	$n_{31}/n_{41} = 2.8$	$n_3/n_{43} = 4.9$

the theoretical predictions for the LS and TS parameters under the adiabatic index $\tilde{\Gamma} = 4/3$ are summarized in Table 4.1.

4.4 Simulation results

The jet-ambient interactions include the growth of the oblique instability (Bret et al., 2010), and the generation of magnetic fields which decelerate the jet stream and consequently form a double shock structure. At late times, the particles are effectively heated and accelerated. This section aims to explain the scenario in more detail.

4.4.1 Formation of the CD

When the particles jet interacts with the ambient plasma, the distribution of particles is extremely anisotropic and is susceptible to several instabilities, e.g., electrostatic modes (two-stream or Buneman instabilities) and electromagnetic modes (filamentation or Weibel instabilities). Depending on the the jet-to-ambient density ratio, jet and ambient temperatures, and jet drift velocity, the two-stream, filamentation, or oblique modes will dominate the linear phase. Whereas perturbations parallel and normal to the jet stream are potentially present, the instability propagates obliquely.

The jet electrons rapidly decelerate when they interact with ambient particles to form electron current filaments in both jet and ambient plasmas (Figure 4.3a). As a result, the density of the jet electron increases from $n_{41}/n_1 = 1.7$ to $n_{41}/n_1 \simeq 2.2$ just behind the jet front (Figure 4.3b). On the other hand, ambient electrons become swept up by the incoming jet stream (Figure 4.3c) and the density of the ambient electrons increases by a factor of three near the jet front (Figure 4.3d). In this stage (about $t = 40\omega_{pe}^{-1}$), a CD is formed around $x = 36\lambda_{ce}$ which separates the decelerated jet electrons from the

accelerated ambient electrons. The decelerated jet electrons become mainly confined to the left side of the CD and pile up in this region. However, due to the CD formation, the accelerated ambient electrons are dominantly confined to the right side of the CD and pile up due to continuous sweeping by the jet inflow. Once trapped in the left side of the CD, the jet electron populations commence heating.

Due to larger ion inertia, the jet ions are able to penetrate deeper into the ambient plasma without significant deceleration (Figures 4.3e and 4.3f) and ambient ions are present in deeper lengths of the jet stream (Figures 4.3g and 4.3h). Therefore, a certain fraction of both ion populations (jet and ambient) is present in each other before the CD is fully formed. These fractions form a separate population on the two sides of the CD. Each of these populations are affected by another plasma medium (jet or ambient) and is reflected back toward the CD. For the ambient fraction, since the ions have no means of either passing through the CD or escaping from the continuous flow of jet particles, they are trapped in the left side of the CD and will eventually become part of the TS population. This population is visible in the ambient ion phase-space and density plots in Figures 4.3g and 4.3h. Due to their highly relativistic forward momentum ($p_{xi} = 80\text{MeV}/c$), the deceleration of the jet ions by the ambient plasma will take place at later stages, following the formation of LS in the ambient particles. Therefore, the thermodynamic properties of the jet and ambient plasmas (density and temperature) would be different across the LS. This leads to the formation of a double layer (will be discussed in Section 4.4.5) which causes the tapping of another fraction of ambient ions in the right side of the CD. This population will become part of the LS.

4.4.2 Evolution of the TS

The continuous stream of the particle jet and the inability of the particles to cross the CD result in the formation of shocks on both sides. Since the ambient plasma located in the right side of our simulation box represents the interstellar medium and the jet plasma coming from the left represents the ejecta, we designate the right shock as the LS and the left shock as the TS. The time evolution of the TS structure is illustrated in Figures 4.4 as a sequence of snapshots that shows the magnetic field component B_y and the averaged total ion density from $t = 40\omega_{pe}^{-1}$ (Figure 4.4a) up to $t = 280\omega_{pe}^{-1}$ (Figure 4.4g) with an interval of $\Delta t = 40\omega_{pe}^{-1}$. They show that the TS propagates in the positive x -direction with $\beta_{ts1} = 0.66$. The peak value of the total ion density corresponding to the TS reaches $n_{31}/n_{41} = 2.9$ at $t = 280\omega_{pe}^{-1}$ (Figure 4.4g), in good agreement with the hydrodynamic jump conditions for a relativistic gas which predict $\beta_{ts1} = 0.68$ and $n_{31}/n_{41} = 2.8$ for the TS in the ambient rest frame (see Table 4.1).

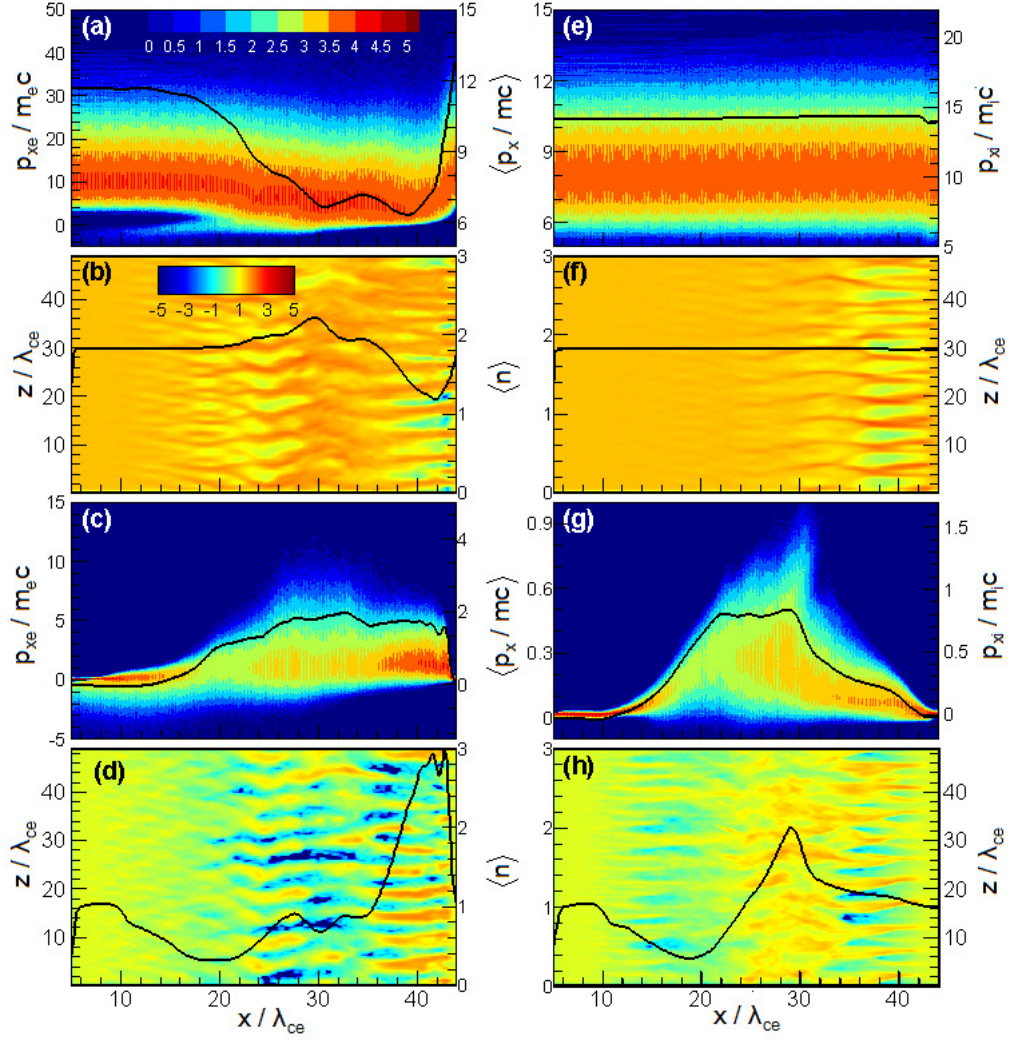


FIGURE 4.3: Structure of the jet-ambient interaction at time $t = 40\omega_{pe}^{-1}$ when the fastest jet ions reach $x = 45\lambda_{ce}$. The longitudinal phase-space distribution and density in log scale are displayed for the following: jet electrons in panels (a) and (b), ambient electrons in panels (c) and (d), jet ions in panels (e) and (f), and ambient ions in panels (g) and (h). The over-plotted line in panels (a), (c), (e), and (g), shows the average momentum in x -direction. The over-plotted line in panels (b), (d), (f), and (h), shows the transversely averaged (in yz -plane) density normalized to the density in the unshocked ambient. In panels (a), (c), (e), and (g), the phase-space distributions are expressed in $\log[N(x, p_x)]$.

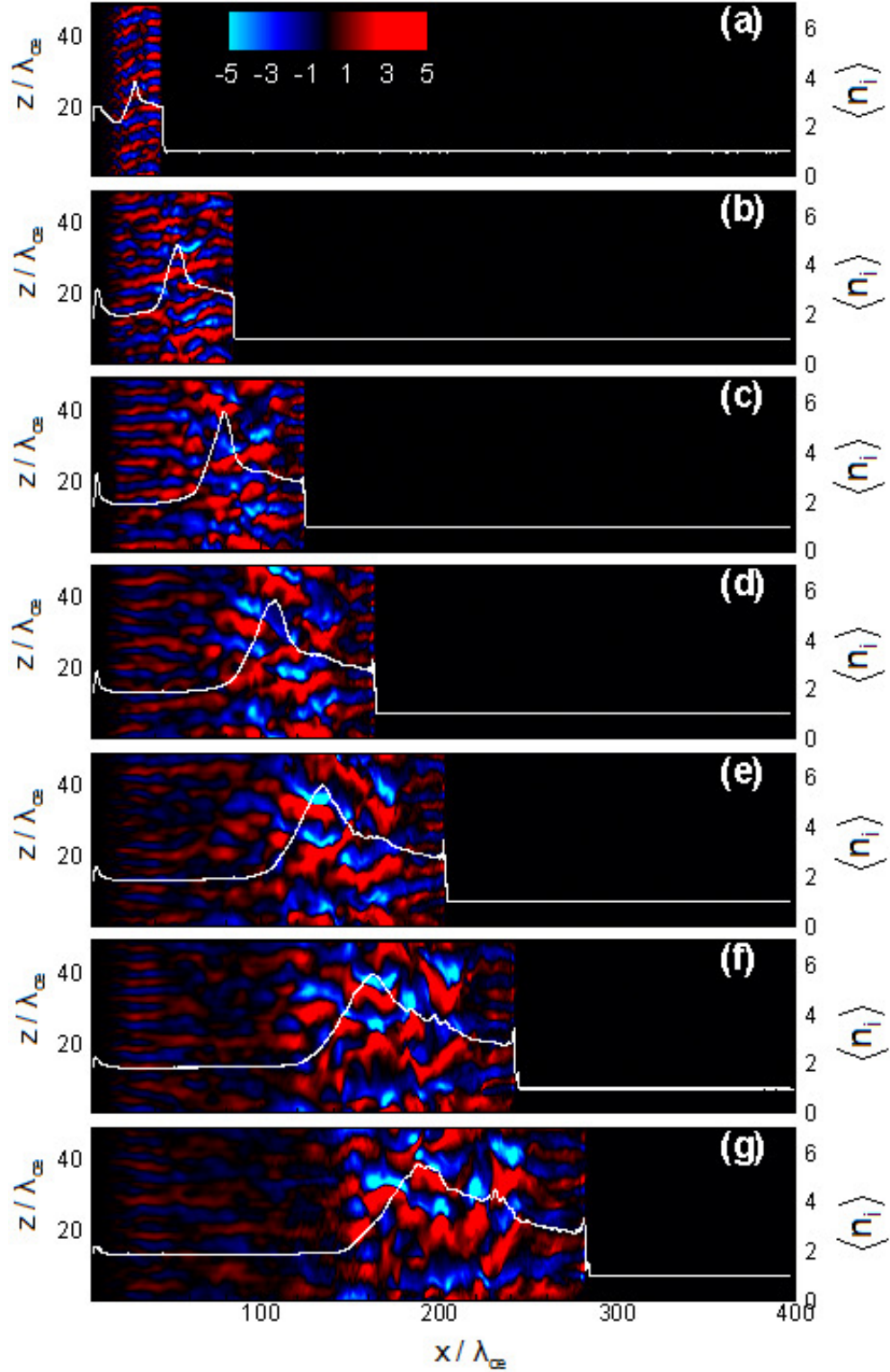


FIGURE 4.4: The time evolution of the TS structure. Sequence snapshots of the magnetic field component B_y at $y = 24\lambda_{ce}$ from $t = 40\omega_{pe}^{-1}$ panel (a), up to $t = 280\omega_{pe}^{-1}$ panel (g), with an interval of $\Delta t = 40\omega_{pe}^{-1}$. Over-plotted in each panel is the transversely averaged total ion density normalized to the density in the unshocked ambient.

As shown before in Figure 4.3g, prior to the full formation of the CD, a fraction of ambient ions is present in a deeper length through the jet stream due to their higher inertia against sweeping by particles jet. They are continuously pushed toward the CD by the incoming jet stream (see Figures 4.5). Encountering the CD, these ambient ions are reflected back into the left side of the CD. Therefore, the reflected ambient ions are trapped and start to pile up on the left side of the CD. This process results in the formation of the ambient ion pile in the TS structure.

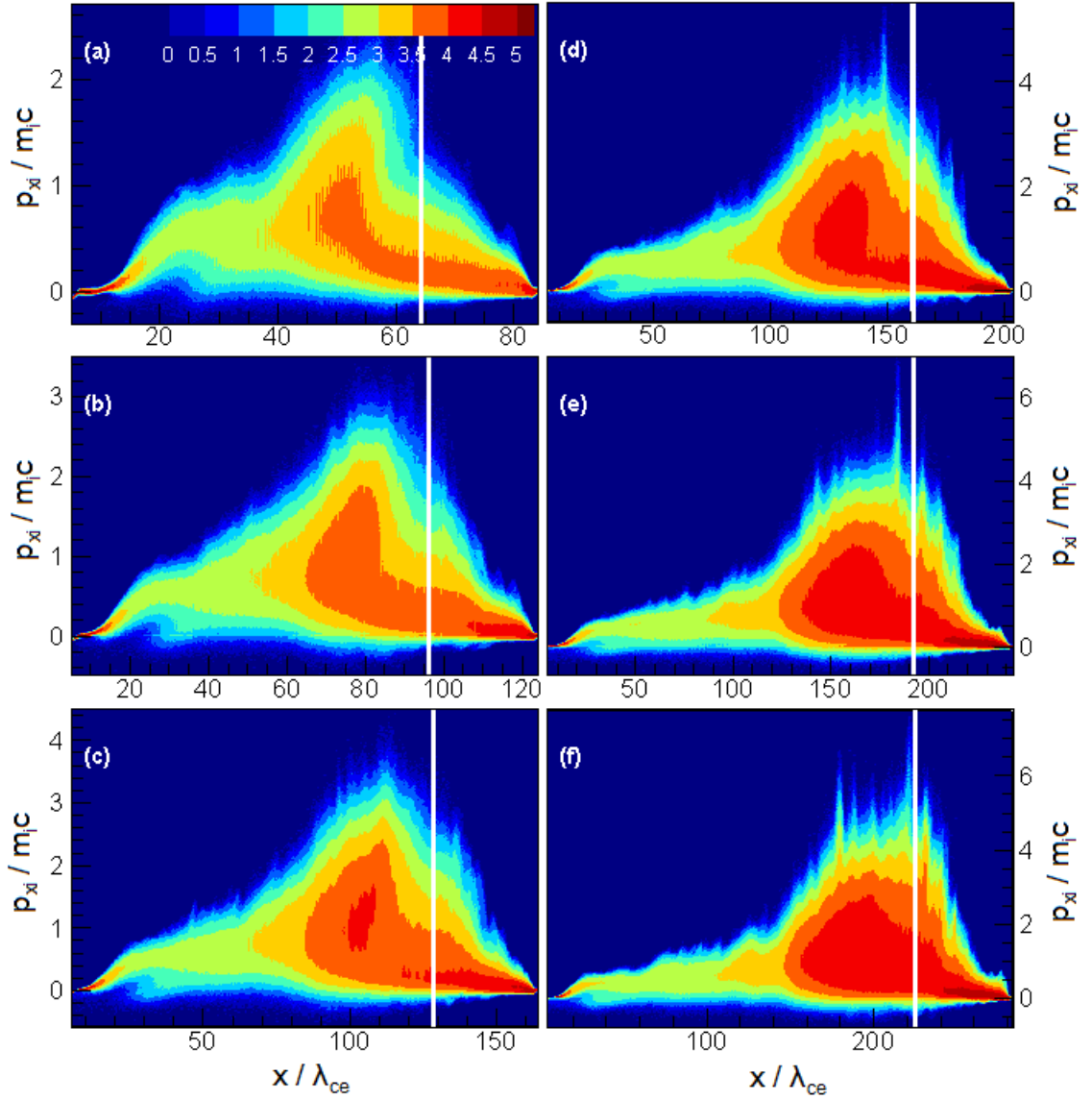


FIGURE 4.5: The longitudinal phase-space distribution of ambient ions expressed in $\log[N(x, p_x)]$ during evolution of the TS structure from $t = 80\omega_{pe}^{-1}$, panel (a), up to $t = 280\omega_{pe}^{-1}$, panel (f), with an interval of $\Delta t = 40\omega_{pe}^{-1}$. The position of the CD at each time is shown by a vertical white line.

The electron contribution in the TS structure belongs to the jet electrons (see Figures 4.3a and 4.3b). The induced magnetic fields due to the Weibel-like instabilities in the

jet-ambient collision region resist the propagation of incoming jet electrons into the ambient plasma, which causes the deceleration of the jet electrons and the formation of the CD (Figures 4.6). formed CD does not allow any more jet electrons to pass into the ambient medium. They are effectively stopped at the left side of CD and start to pile up as a part of the TS structure.

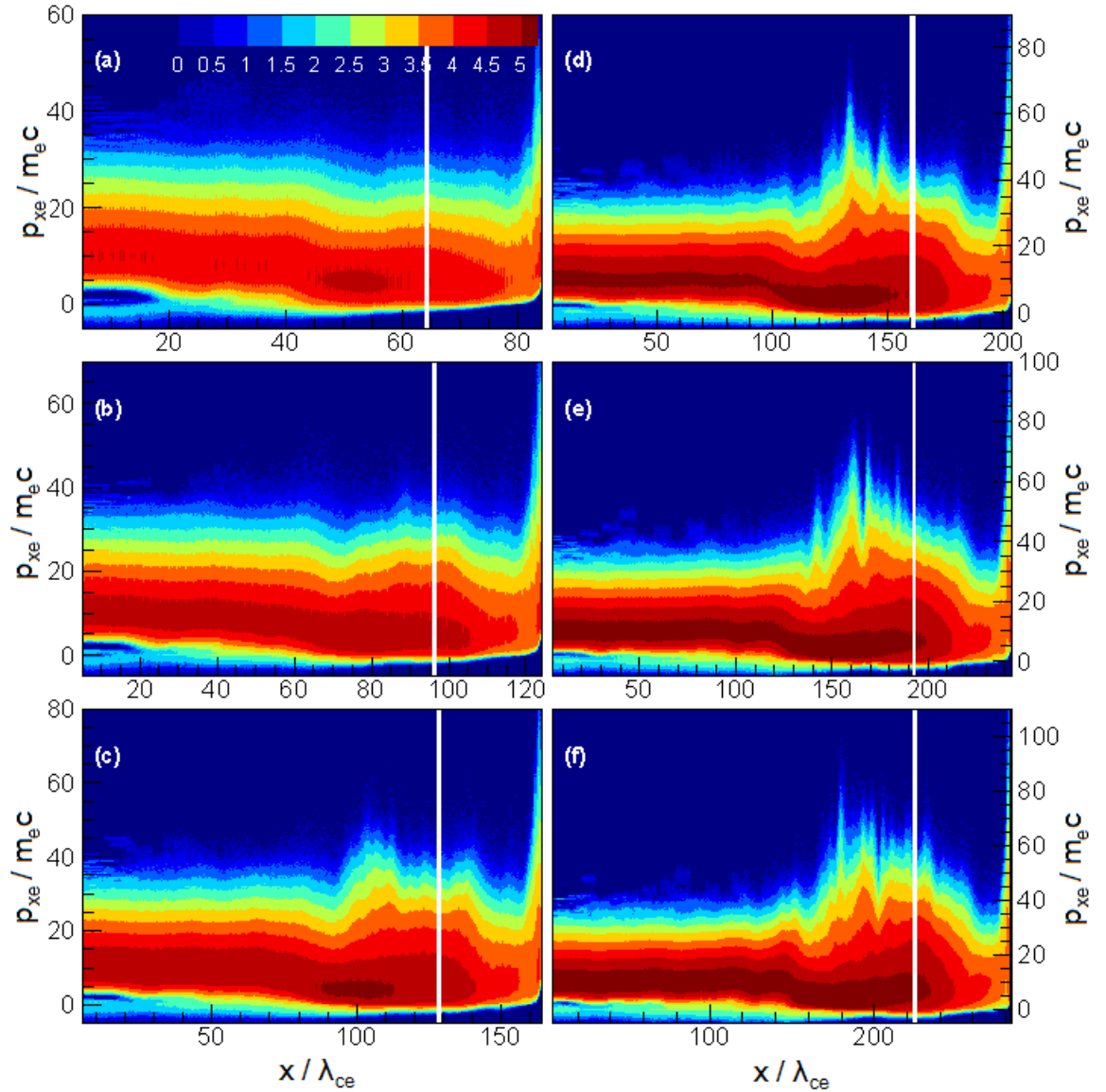


FIGURE 4.6: The longitudinal phase-space distribution of jet electrons expressed in $\log[N(x, p_x)]$ during evolution of the TS structure from $t = 80\omega_{pe}^{-1}$, panel (a), up to $t = 280\omega_{pe}^{-1}$, panel (f), with an interval of $\Delta t = 40\omega_{pe}^{-1}$. The position of the CD at each time is shown by a vertical white line.

At $t = 280\omega_{pe}^{-1}$, the compression ratio for the TS reaches the level of $n_{31}/n_{41} = 2.9$ (see Figure 4.4g) predicted by the hydrodynamic jump conditions for a 3D relativistic plasma with adiabatic index $\tilde{\Gamma} = 4/3$. The shock in the electrons is caused mainly by the jet electrons (Figures 4.7a and 4.7c), while the ion contribution is supplied by

the ambient ions (Figures 4.7b and 4.7d). The extended region between the unshocked and shocked jet constitutes the trailing edge. The structure of the trailing edge is exclusively controlled by the strongly nonlinear jet-ambient interactions which result in the formation and merger of current filaments due to the Weibel-like instabilities (Bret et al., 2010). In the vicinity of the TS, the corresponding electromagnetic fields are predominantly transverse. The transverse electric and magnetic fields are related to each other via $\vec{E} = -\vec{\beta} \times \vec{B}$ where $\vec{\beta}$ is the velocity of the carriers. The carriers move roughly at the speed of light in the x -direction (drift velocity $v_d = E/B \simeq c$), and hence $\beta \simeq \beta_x \simeq 1$. As a result, the transverse fields are as $E_y = B_z$, and $E_z = -B_y$ (see Figures 4.8). These electric fields cause heating of the particles in the transverse directions. Ahead of the filaments (toward the unshocked jet), the electrons belong to the ambient plasma are not present (Figure 4.7c). However, a fraction of jet electrons which are reflected in the CD zone flows with a slightly relativistic speed against the injected jet (see Figures 4.6). This process excites a Weibel-like two-stream instability (Medvedev and Loeb, 1999, Frederiksen et al., 2004, Hededal et al., 2004) between the reflected jet electrons and incoming jet electrons that constructs a longitudinal electrostatic perturbation as E_x (Figure 4.8g) and associated density modulations, further to the filamentation of the trailing edge (see Figures 4.8). The amplitude of Weibel-like two-stream instability saturates at small levels, and its major effect is heating the jet electrons in the trailing edge. Toward the TS, the longitudinal electrostatic perturbations become amplified through the stream of the reflected ambient ions in the CD region (see Figures 4.5), and the fluctuations in E_x are enhanced (Figure 4.8g). The longitudinal and transverse structures are present at the same time, remarking that the Weibel-like instability and the longitudinal electric field act parallelly and propagate obliquely.

4.4.3 Evolution of the LS

The evolution of the LS structure is displayed in Figures 4.9 where the magnetic field component B_y and the averaged total ion density are shown in sequent snapshots from $t = 300\omega_{pe}^{-1}$ (Figure 4.9a) up to $t = 500\omega_{pe}^{-1}$ (Figure 4.9f) with an interval of $\Delta t = 40\omega_{pe}^{-1}$. As one can see, a density compression appears primarily in the ambient plasma at late stages ($t \simeq 300\omega_{pe}^{-1}$) which we designate as the LS. The compression ratio rises with time until reaches $n_{21}/n_1 = 6.5$ at the end of the simulation $t = 500\omega_{pe}^{-1}$ (Figure 4.9f). The LS structure moves with a speed $\beta_{ls1} = 0.89$ in the positive x -direction. In the formed double shock structure, the CD moves in the positive x -direction with a speed $\beta_{cd1} = 0.80$. The hydrodynamic jump conditions for the LS predict $\beta_{ls1} = 0.85$ and $n_{21}/n_1 = 16$ in the ambient rest frame (Table 4.1). Hence, the density jump for the

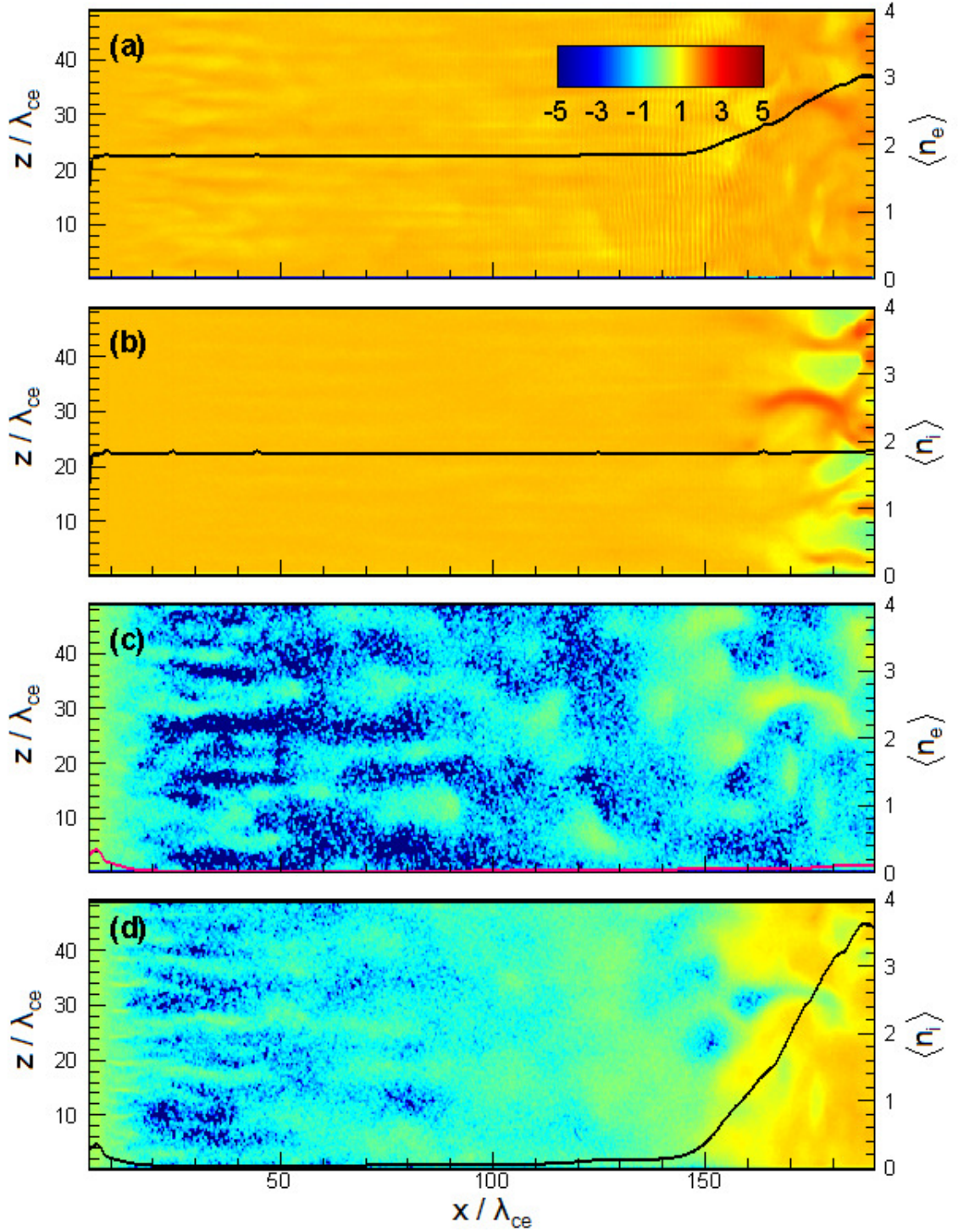


FIGURE 4.7: Structure of the trailing edge at time $t = 280\omega_{pe}^{-1}$. The density of the particle in log scale with an over-plotted line for the average density of the particle normalized to the density in the unshocked ambient is shown for the: (a) jet electron, (b) jet ion, (c) ambient electron, and (d) ambient ion, respectively.

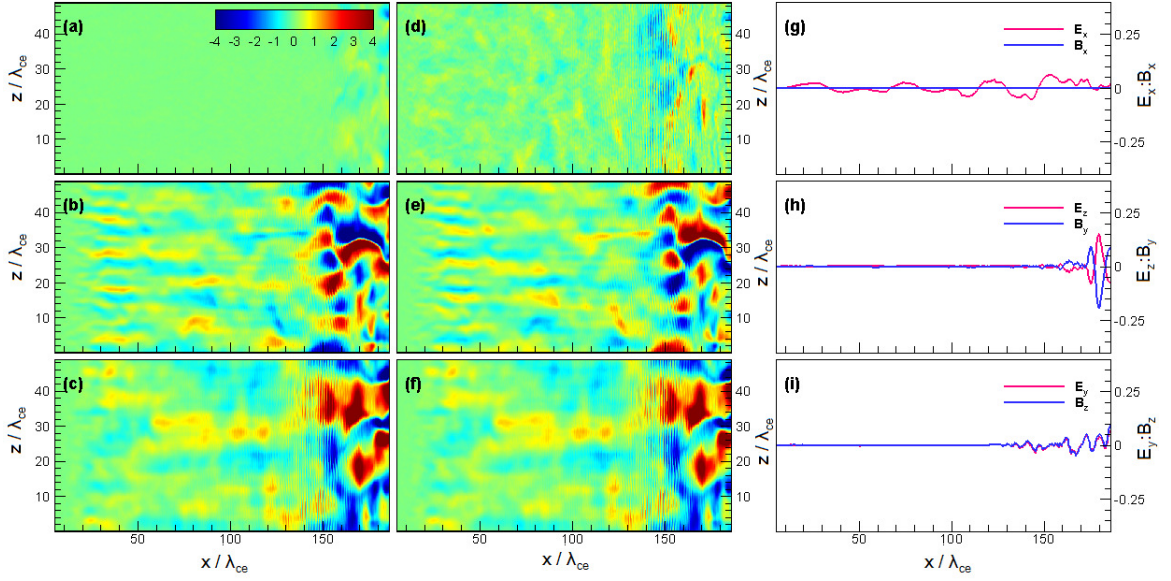


FIGURE 4.8: Structure of the trailing edge at $t = 280\omega_{pe}^{-1}$. Panels (a), (b) and (c) show the components of the magnetic field B_x , B_y , and B_z , respectively, at $y = 24\lambda_{ce}$. Panels (d), (e) and (f) show the components of the electric field E_x , E_z , and E_y , respectively, at $y = 24\lambda_{ce}$. The transversally averaged field components ($E_x : B_x$), ($E_z : B_y$), and ($E_y : B_z$) are shown in panels (g), (h) and (i), respectively.

shocked ambient is about a factor of ~ 2.5 smaller than theoretically predicted for a fully developed LS.

The ambient particles (both electrons and ions) are swept by the incoming jet stream. Due to the CD formation in the early stages and reflection by the CD, the ambient electrons are mainly trapped in the right side of the CD (Figures 4.10) and create a compressed region as part of the LS structure. In regard to the ambient ions, as discussed in Section 4.4.2, they are also present at deeper lengths of the trailing edge due to their higher rigidity against the incoming jet stream. On the other hand, the formed CD and continuous sweeping by the jet stream accumulate part of the ambient ions on the right side of the CD (Figures 4.11). This population contributes to the LS structure. Furthermore, during the evolution of the LS, reflection of the ambient ions against the incoming jet occurs for which these hot counter-streaming ions are obvious as a population with negative momentum in Figures 4.11. Counter-streaming ions play an important role in preserving the double layer in the trailing edge, which will be discussed in Section 4.4.5.

At the end of the simulation, the jump condition for the TS is not reached the jump condition for a fully developed hydrodynamic shock. The compression of electrons is dominantly supplied by the ambient electrons (Figures 4.12a and 4.12c), although the deeply penetrating jet electrons that are trapped in the right side of the CD (see Figure 4.12a beyond $x = 420\lambda_{ce}$) contribute slightly to the LS structure. The ion contribution

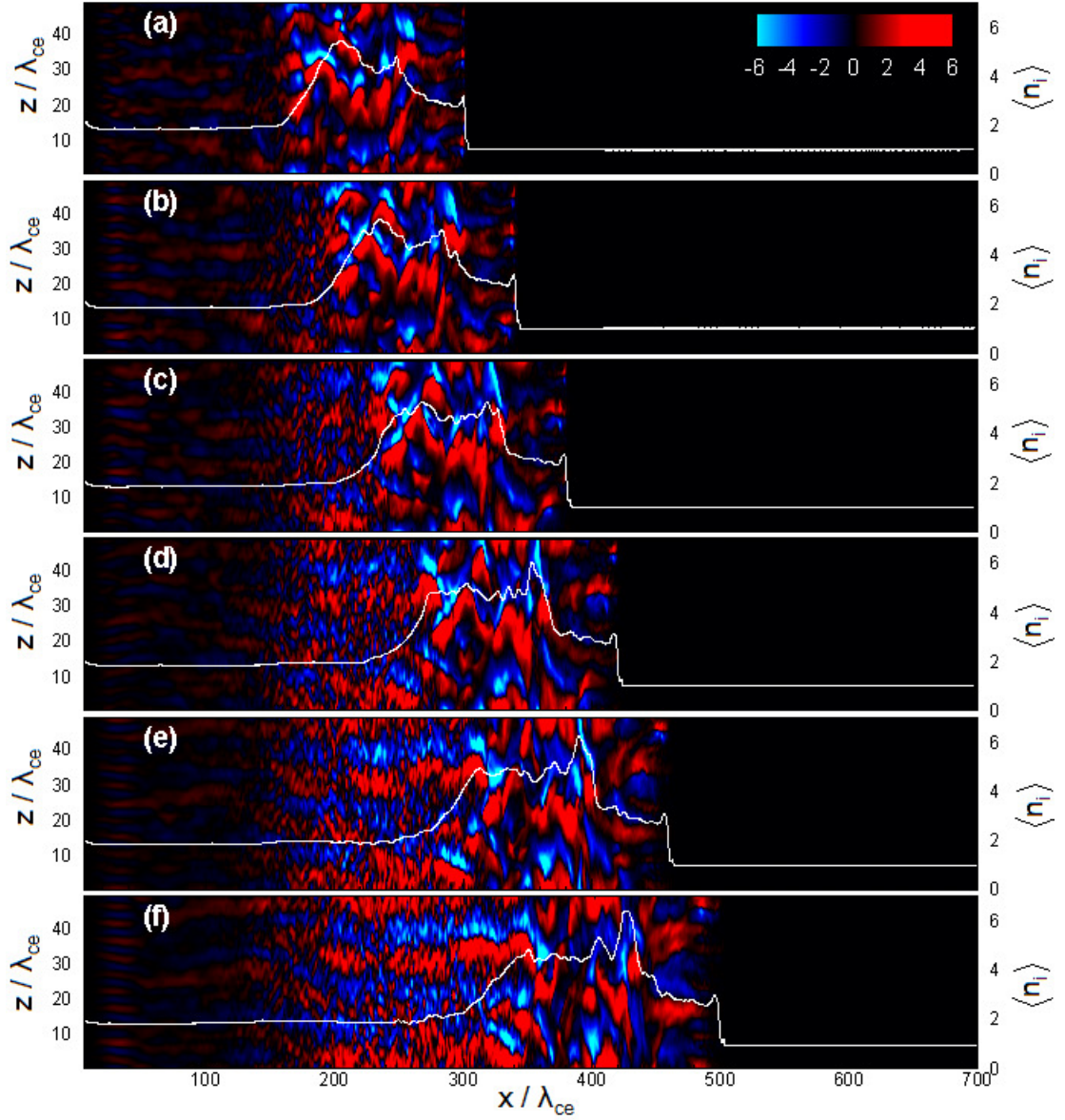


FIGURE 4.9: The time evolution of the TS structure. Sequence snapshots of the magnetic field component B_y at $y = 24\lambda_{ce}$ from $t = 300\omega_{pe}^{-1}$, panel (a), up to $t = 500\omega_{pe}^{-1}$, panel (f), with an interval of $\Delta t = 40\omega_{pe}^{-1}$. Over-plotted in each panel shows the transversely averaged (in yz -plane) total ion density normalized to the density in the unshocked ambient.

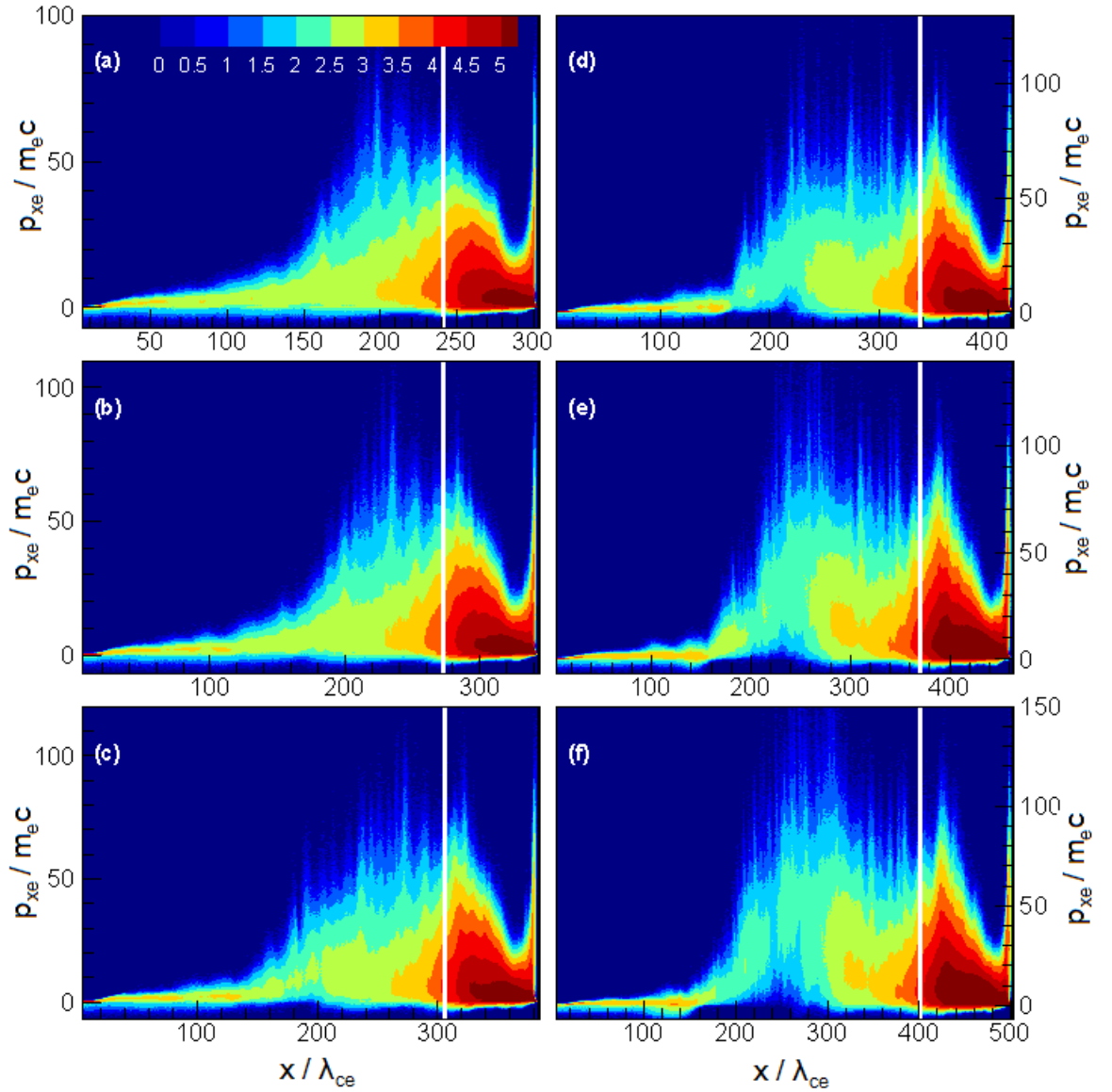


FIGURE 4.10: The longitudinal phase-space distribution of ambient electrons expressed in $\log[N(x, p_x)]$ during evolution of the LS structure from $t = 300\omega_{pe}^{-1}$, panel (a), up to $t = 500\omega_{pe}^{-1}$, panel (f), with an interval of $\Delta t = 40\omega_{pe}^{-1}$. The position of the CD at each time is shown by a vertical white line.

is exclusively provided by the ambient ions (Figures 4.12b and 4.12d). The extended region between the unshocked and shocked ambient represents the leading edge.

The structure of the electromagnetic fields in the leading edge is mainly controlled by relativistic ion beam-plasma instabilities, where the propagation of dense jet ions into the ambient ions excites the Weibel-like instabilities with wave vectors oriented obliquely to the jet propagation direction (Bret et al., 2010). The Weibel-like instabilities lead to current filamentation (see Figure 4.12d) and the generation of transverse magnetic fields (Figures 4.13a, 4.13b, and 4.13c). In contrast with the ordinary filamentation

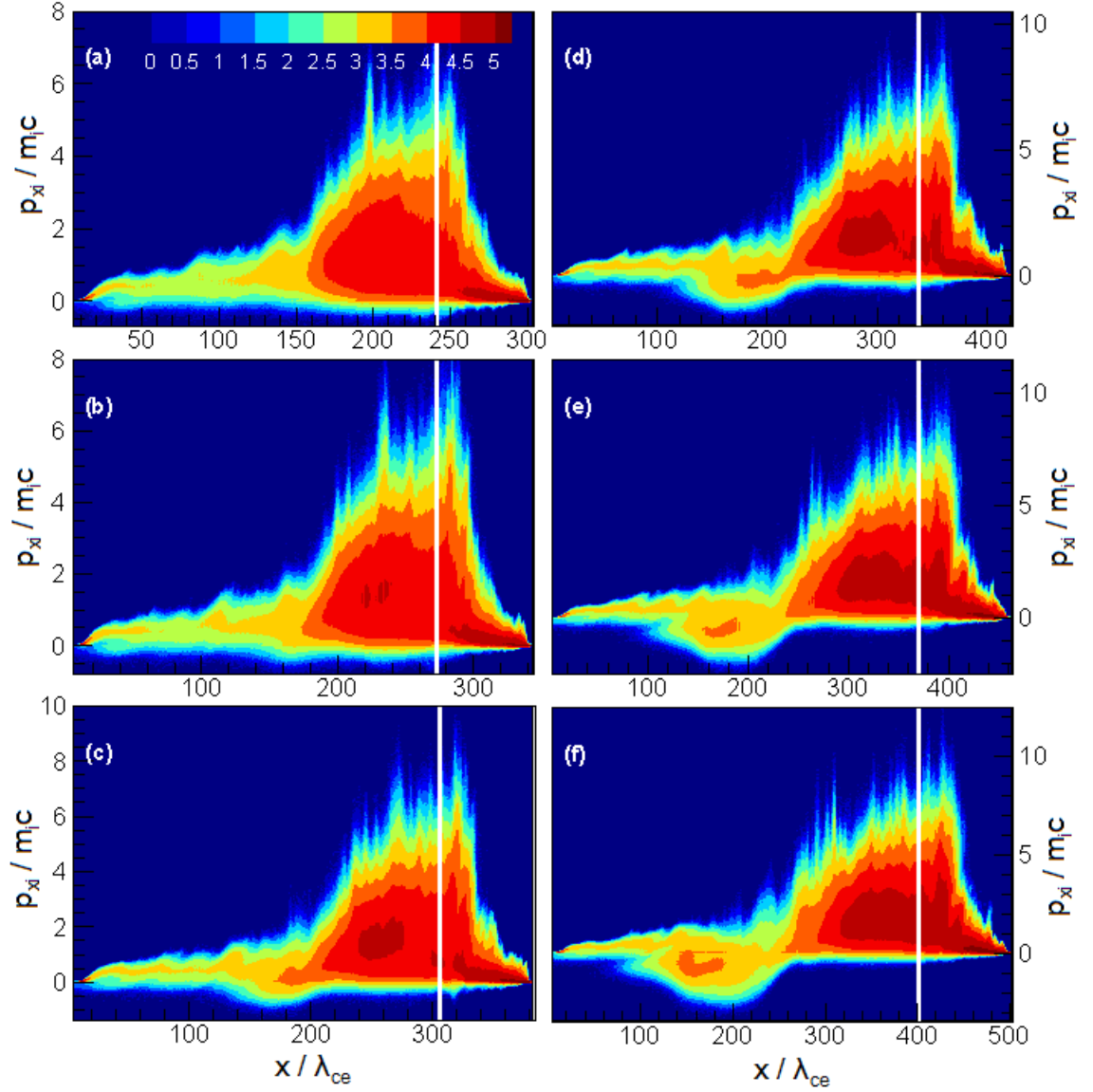


FIGURE 4.11: The longitudinal phase-space distribution of ambient ions expressed in $\log[N(x, p_x)]$ during evolution of the LS structure from $t = 300\omega_{pe}^{-1}$, panel (a), up to $t = 500\omega_{pe}^{-1}$, panel (f), with an interval of $\Delta t = 40\omega_{pe}^{-1}$. The position of the CD at each time is shown by a vertical white line.

instabilities, the electric fields are not purely transverse and there is a finite electrostatic component (see Figures 4.13d, 4.13e, 4.13f and 4.13g). The relation between the transverse electric and magnetic fields is the same as the trailing edge, where $\vec{E} = -\vec{\beta} \times \vec{B}$ and hence $E_y = B_z$, and $E_z = -B_y$ (Figures 4.13). Only when the jet and ambient plasmas are quite symmetric (i.e., same density, temperature, and drift velocity), the filamentation instability would be purely transverse (Bret et al., 2005, 2010). In order to not result in any space charge, the beam and ambient plasmas must pinch absolutely at the same rate. However, this rate highly depends on both the thermal spread (since thermal pressure opposes the magnetic pinching) and the relativistic momentum (and

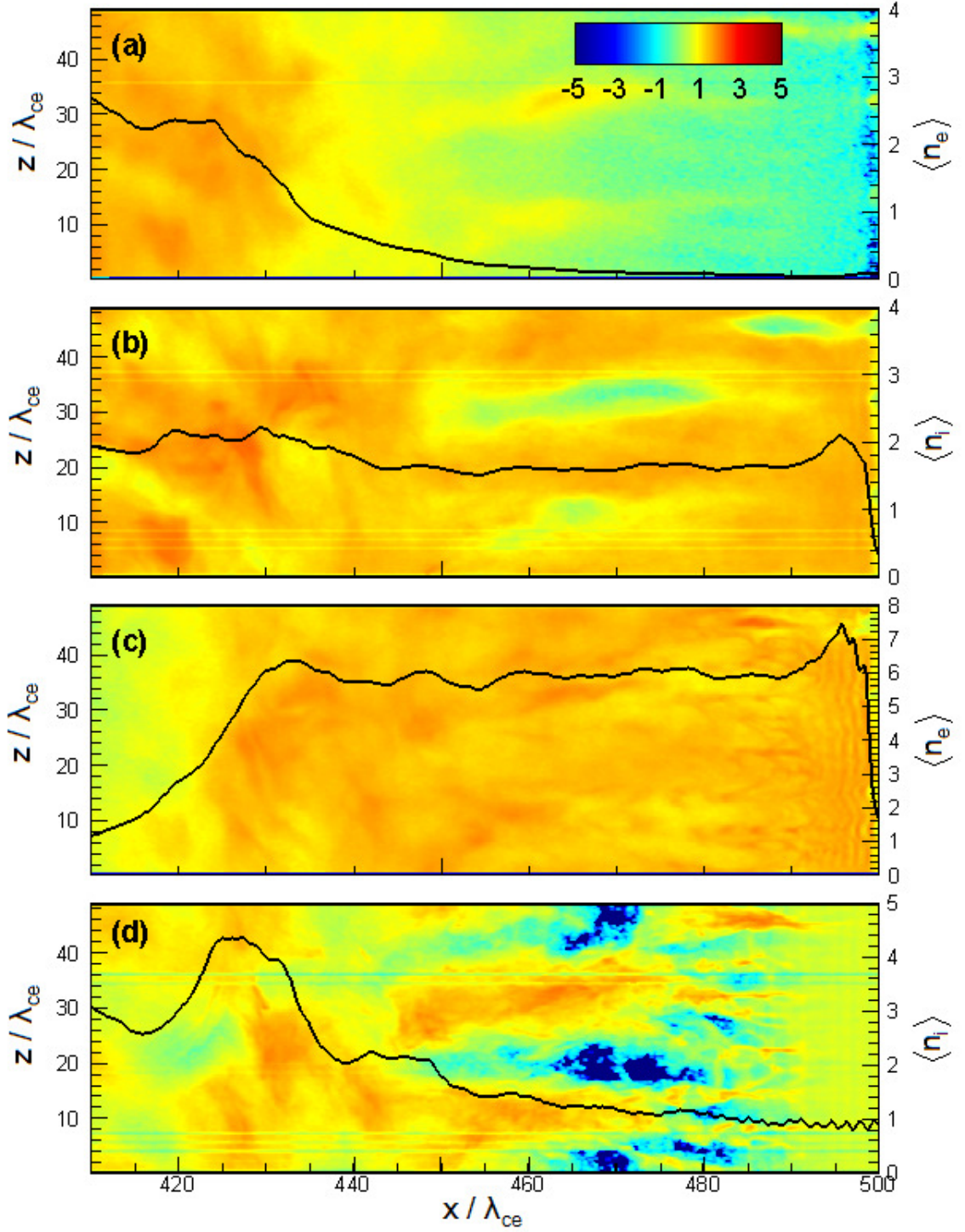


FIGURE 4.12: Structure of the leading edge at time $t = 500\omega_{pe}^{-1}$. The density of the particle in log scale with an over-plotted line for the average density of the particle normalized to the density in the unshocked ambient is shown for the: (a) jet electron, (b) jet ion, (c) ambient electron, and (d) ambient ions, respectively.

thus the Lorentz factors) of the two populations. Charge imbalance hence appears whenever these parameters are different (see also Choi et al. (2014)). The induced magnetic fields influence the dynamics of particles. The jet ions are decelerated in average and demonstrate a fraction of particles with low speeds. Concurrently, the ambient ions, where filamentation is strongest (Figure 4.12d), are heated. Thick filaments in the ambient ions are surrounded by electrons. The kinetic energy freed by the slowed down jet ions is transferred to the heating of the electrons by the transverse electric fields around the ion filaments. The space between the ion filaments is empty of ambient ions and occupied by the jet ions. The filamentary structures in the jet electrons are more diffusive due to their higher electrons temperature (Figure 4.12a).

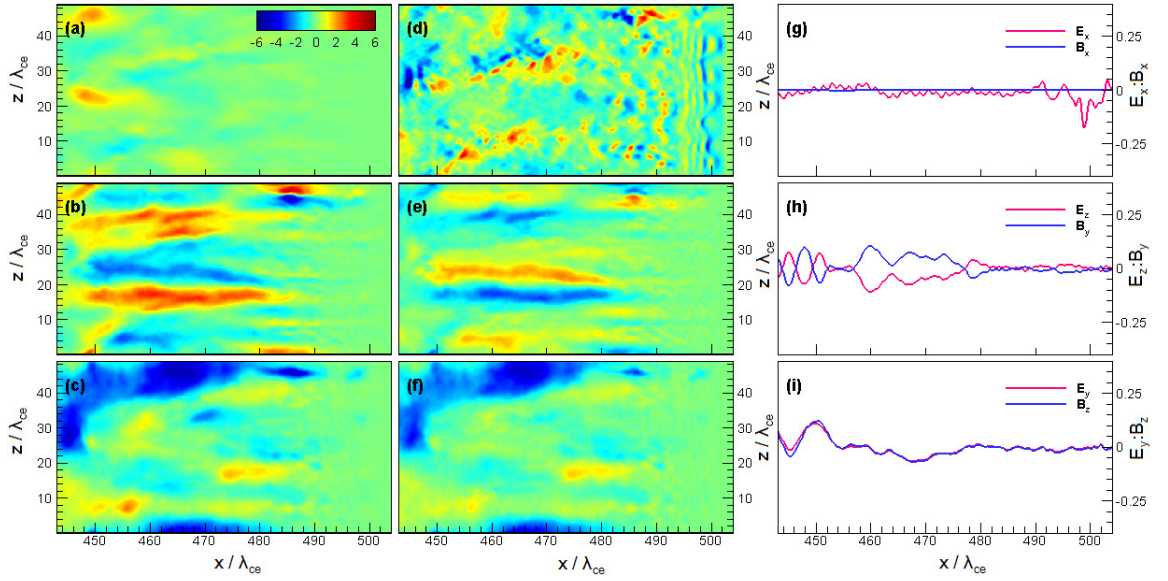


FIGURE 4.13: Structure of the leading edge at $t = 500\omega_{pe}^{-1}$. Panels (a), (b) and (c) show the components of the magnetic field B_x , B_y , and B_z , respectively, at $y = 24\lambda_{ce}$. Panels (d), (e) and (f) show the components of the electric field E_x , E_z , and E_y , respectively, at $y = 24\lambda_{ce}$. The transversally averaged field components $(E_x : B_x)$, $(E_z : B_y)$, and $(E_y : B_z)$ are shown in panels (g), (h) and (i), respectively.

4.4.4 Shock structure at the end of simulation

A double shock structure forms when the relative velocity between the jet and ambient plasmas exceeds the sound speed in the ambient plasma and the magneto-sonic speed in the jet, and the pressure in the shocked region exceeds the pressure in the unshocked region (Zhang and Kobayashi, 2005). A first density compression appears due to the deflection of jet electrons and ambient ions which we define as the TS. This density compression grows due to amplification of the Weibel-like instabilities at the expense of the streaming ions. Time stacked plots of the transversely averaged (in the yz -plane) total ion density as a function of axial distance are shown in Figure 4.14a. The time

range is $t = 20 - 540\omega_{pe}^{-1}$ with an interval of $\Delta t = 20\omega_{pe}^{-1}$. One can readily identify a TS propagating in the positive x -direction with $\beta_{ts1} \approx 0.66$. The shape and peak value of the total density corresponding to the TS are almost constant in time ($n_{31}/n_{41} \approx 2.9$, Figure 4.14b), and the TS is fully developed. On the other hand, a density compression appears mainly in the ambient plasma at late times ($t \approx 300\omega_{pe}^{-1}$) that we identify as the LS. The compression ratio rises with time until reaches about $n_{21}/n_1 \approx 6$ at the end of the simulation (Figure 4.14b). The LS structure moves at a speed $\beta_{ls1} \approx 0.89$ in the positive x -direction. The CD moves in the positive x -direction at a speed $\beta_{cd1} \approx 0.80$. The shocked region ($340\lambda_{ce} \leq x \leq 430\lambda_{ce}$ at $t = 500\omega_{pe}^{-1}$) between the TS and LS separates the jet and ambient upstreams (Figure 4.14b).

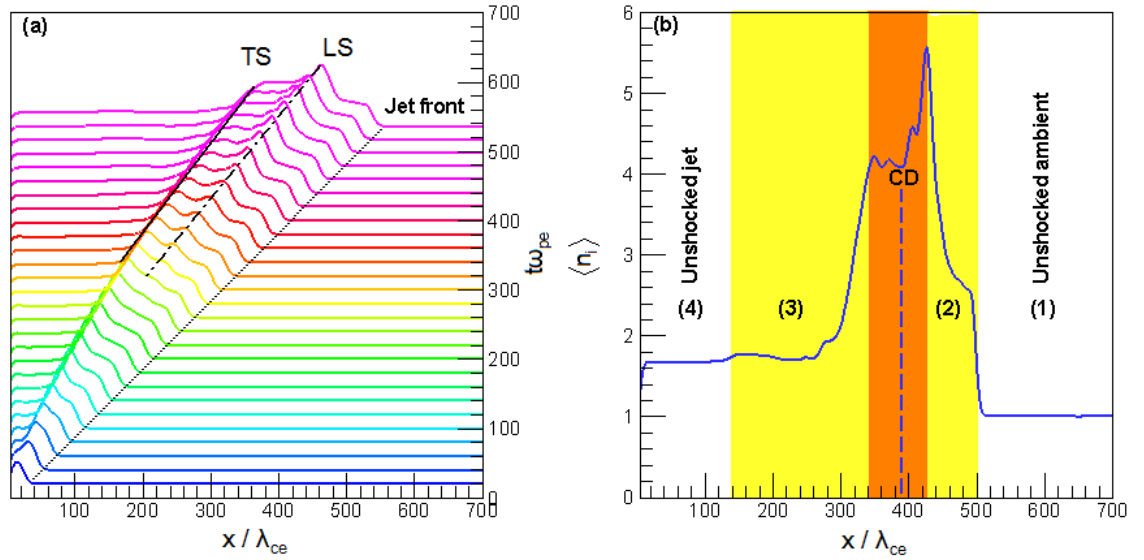


FIGURE 4.14: Panel (a) shows stacked profiles of the transversely averaged ion density (total jet+ambient) from $t = 20\omega_{pe}^{-1}$ up to $540\omega_{pe}^{-1}$ with an interval of $\Delta = 20\omega_{pe}^{-1}$ and panel (b) represents the ion density profile at $t = 500\omega_{pe}^{-1}$. Solid, dashed-dot, and dotted black lines in panel (a) indicate the TS, LS, and jet front, respectively. In panel (b) the shocked region is shown as orange, yellow represents the shock transition region (left for the TS and right for the LS), white shows the unshocked regions (jet or ambient), and the dashed blue line shows the CD.

4.4.5 Formation of the double layers

While the longitudinal density structures stream to the TS, the density of the ambient ions and shock-reflected ambient ions increases (see Figures 4.11). As a result of shock reflection, a hole in the ambient ion will be appeared within the trailing edge (see $200\lambda_{ce} \lesssim x \lesssim 260\lambda_{ce}$ in Figure 4.15h). The hole is filled with shocked jet electrons, a small fraction of the ambient electrons trapped in the trailing edge due to the CD, and jet ions. This process forms a double layer plasma and the associated ambipolar electrostatic field causes trapping of the shock-reflected ambient ions behind the electrostatic field

(see $x \lesssim 220\lambda_{ce}$ in Figure 4.15h). The electrons are locally accelerated to high energy ($p_e \simeq 75\text{MeV}/c$ in Figure 4.15a) and convect toward the TS region. The accelerated jet electrons and the reflected ambient ions resemble to the free streaming particle species in a double layer plasma as discussed in Block (1978). Figure 4.15 presents the structure of the jet-ambient interaction at time $t = 500\omega_{pe}^{-1}$ which is illustrative of the features explained before. Shown in Figure 4.15a and 4.15b are the z -component of the electric field, E_z , and y -component of the magnetic field, B_y , respectively. Panels 4.15c-4.15e show the transversally averaged (in the yz -plane) electric and magnetic field components, $[E_x(B_x), E_y(B_z), E_z(B_y)]$. The energy distribution (total of jet+ambient) and average energy along the x -direction for electron and ion species are shown in Figures 4.15f-4.15i. All panels are at $t = 500\omega_{pe}^{-1}$. Where high-speed jet particles interact with the ambient medium (behind the TS at $x \leq 340\lambda_{ce}$) or scattered ambient particles blend with the upstream ambient (in front of the LS at $430\lambda_{ce} \leq x$), particles distribution becomes strongly anisotropic. Anisotropies result in the Weibel-like instability which generates current filaments in these regions with currents in the x -direction. According to Ampere's law, these current filaments are encircled by transverse magnetic fields, and we see that $\langle B_x \rangle = 0$ in Figure 4.15c. The transverse electric fields are related to the magnetic fields via $-\vec{\beta}_{e:i} \times \vec{B} = \vec{E}$ where $\beta_{e:i}$ is the velocity of the electron (ion) carrier. The carriers move roughly at the speed of light in the x -direction, $\beta_{e:i} \simeq \beta_{e:ix} \simeq 1$. Therefore, the transverse electric field components are $E_y = B_z$, and $E_z = -B_y$, as are observed in the simulation results for $[E_y(B_z), E_z(B_y)]$ (Figures 4.15a-4.15e). Additionally, there is a longitudinal ambipolar electric field within the trailing edge, $140\lambda_{ce} \leq x \leq 340\lambda_{ce}$ (Figure 4.15c). This electric field is generated by the double layer (Forslund and Shonk, 1970, Forslund and Freidberg, 1971, Hoshino, 2001, Choi et al., 2014).

The double layer in the trailing edge accelerates jet electrons out of the bulk to an average momentum of $\langle p_e \rangle \simeq 40\text{MeV}/c$ (see Figure 4.15g). The formed double layer is not stationary, but instead is one with a floating potential instead (Figure 4.16). Therefore, the energy of the jet electrons increases in time while the jet electron temperature remains unchanged (as will be shown in Section 4.4.7). The energy of the accelerated electrons exceeds their thermal energies, even after the Weibel-like instabilities have heated the electrons (the average $\langle p_{ye} \rangle \simeq \langle p_{ze} \rangle \simeq 20\text{MeV}/c$, see Figure 4.18b). Therefore, the kinetic energy of the jet electrons have been increased through the double layer potential where $e\langle\phi\rangle \simeq 20\text{MeV}$ (Figure 4.18c). According to the Bohm criterion (Block, 1978), a double layer demands a drift speed which is higher than the thermal one. This criterion is well satisfied whereas $v_d \simeq c$. The accelerated jet electrons then interact with the ambient medium through an oblique Weibel-like instability; in this case, the

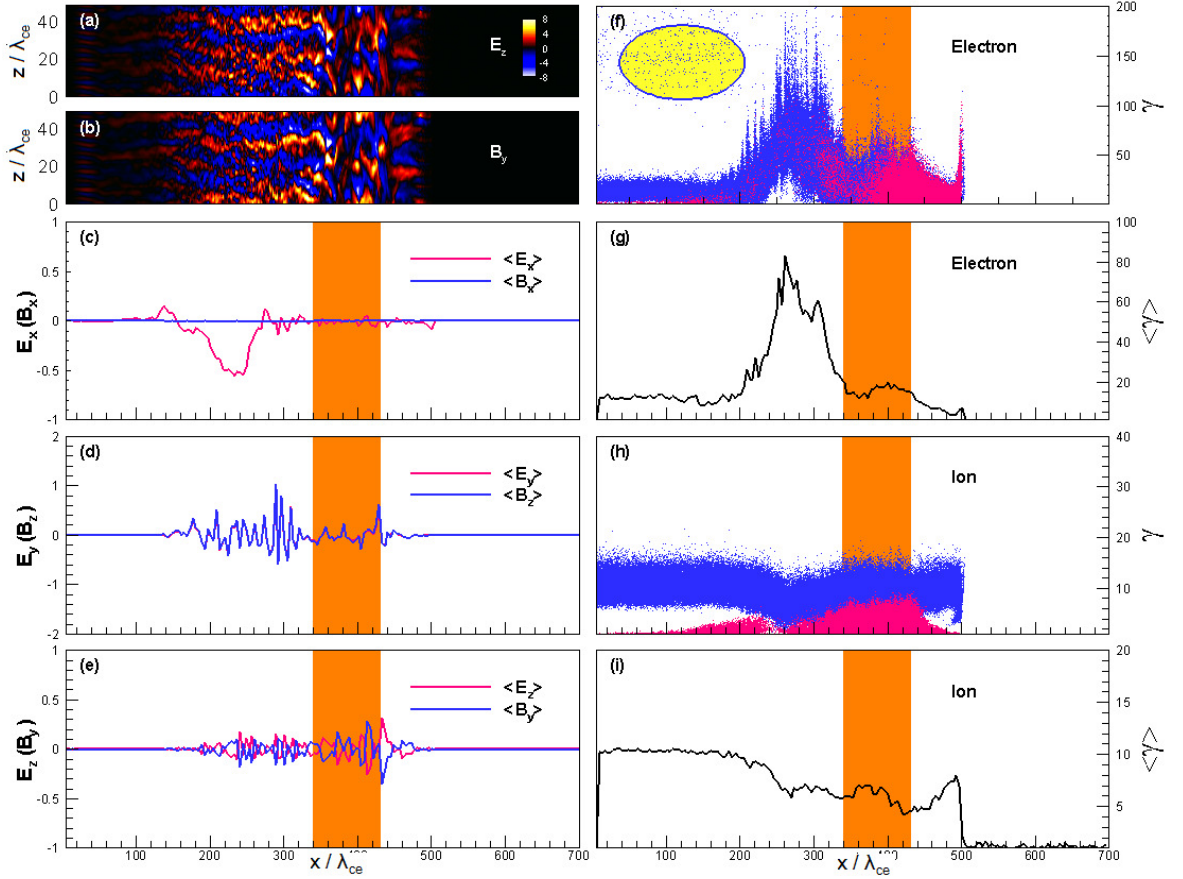


FIGURE 4.15: Structure of the relativistic double shock at $t = 500\omega_{pe}^{-1}$. Panels (a) and (b) show the z -component of the electric field E_z and the y -component of the magnetic field B_y at $y = 24\lambda_{ce}$. Panels (c)-(e) show the transversally averaged (in the yz -plane) field components. Total of the jet (blue) + ambient (red) particle energy distribution, and average energy along x -direction are presented in panels (f) and (g) for electrons, and (h) and (i) for ions. The shocked region is identified by orange coloring or between vertical orange lines. The ellipse in panel (f) shows the high-energy electrons reflected into the upstream. In (f) and (h), 1.2×10^6 particles are randomly selected. Due to the very large number of particles in the simulation, only a part of them is represented. Particles of each population are selected randomly so that the respective distribution function is not affected.

corresponding electromagnetic fields are responsible for the spikes in the electron phase-space distribution within an interval of $200\lambda_{ce} \lesssim x \lesssim 340\lambda_{ce}$ in Figure 4.15f. A secondary two-stream instability was also found in Newman et al. (2001), Dieckmann and Bret (2009), although the jets (beams) were non-relativistic there. Principally, the kind of instability is not vital regarding the development of the double layer since it is created behind it. The electric field of the double layer is strong inasmuch as it can slow down the jet ions by a factor of 50 % from the initial momentum $p_i = 80\text{MeV}/c$ (Figure 4.15i), which supports the energy for the electron acceleration. The double layer is thus an ion decelerator which is characteristic of an electrostatic shock. The corresponding electrostatic TS involving only the ambient ions occurs at $x = 340\lambda_{ce}$.

Another double layer structure exists in the leading edge (see Figure 4.16) which moves with a speed $\beta \simeq c$. The density and temperature of the jet and ambient plasmas differ through the leading edge (see Figures 4.15). Therefore, the quasi-neutrality is violated and a double layer will be formed. This double layer accelerates ambient electrons up to an average energy of $\simeq 5\text{MeV}$ (see Figure 4.15c and Figure 4.18c). Similar to the previous one, the double layer in the leading edge is strong enough to slow down the jet ions stream and supply the energy for electron acceleration. As a result, another electrostatic shock including also the jet ions forms near the jet ion front (see Figures 4.12b and 4.12c).

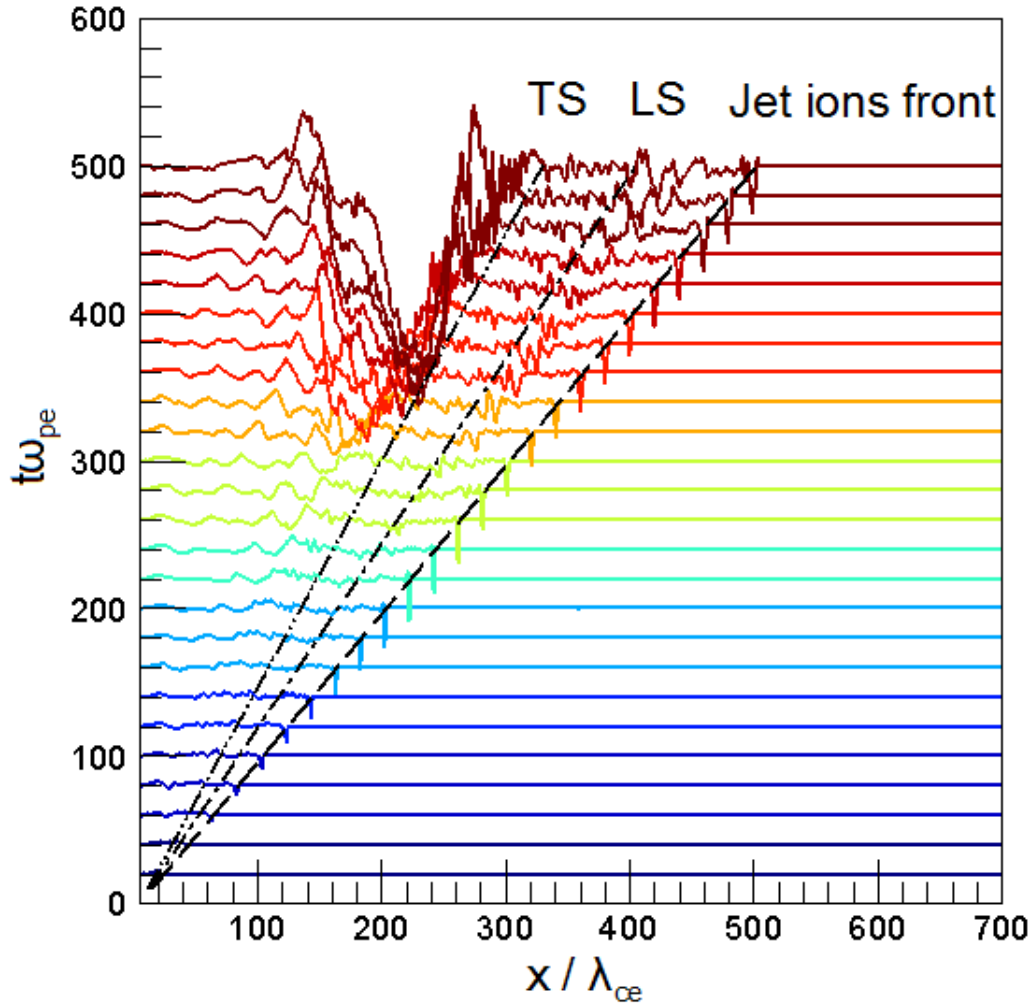


FIGURE 4.16: The stacked profiles of the transversely averaged E_x is shown from $t = 20\omega_{pe}^{-1}$ up to $500\omega_{pe}^{-1}$ with an interval of $\Delta t = 20\omega_{pe}^{-1}$. Dashed-dot-dot, dashed-dot, and dashed lines represent the TS, LS, and jet ions front, respectively.

4.4.6 Electron heating and acceleration

Ion current filaments generated by the Weibel-like instabilities have a crucial role in establishing the shock transition, and electron heating in the unmagnetized electron-ion plasmas (Frederiksen et al., 2004, Hededal et al., 2004, Spitkovsky, 2008a). In Figures 4.17, the longitudinal current density, $J_x = J_{ix} + J_{ex}$, through a transverse cross section is shown at $x = 320\lambda_{ce}$, in the RS transition region (Figure 4.17a and 4.17c) and at $x = 480\lambda_{ce}$, in the FS transition region (Figure 4.17b and 4.17d) for $t = 500\omega_{pe}^{-1}$. Positive (red-white colors) and negative (green-blue colors) represent the ion and electron contribution to the total current, respectively. As one can see, longitudinal current filaments are surrounded by approximately azimuthal magnetic fields (illustrated by the arrows in Figure 4.17a and 4.17b). Electric fields are perpendicular to the magnetic fields and the associated arrows point in the radial direction (Figure 4.17c and 4.17d). In the RS transition region, magnetic fields are predominantly due to the ion filaments (counter-clockwise arrows) and electrons act to Debye shield these filaments (Frederiksen et al., 2004). However, there are some electron filaments (clockwise arrows) within the FS transition region. Furthermore, electromagnetic fields in the RS transition region are stronger than those in the FS transition region. The transverse size of the filamentary structures is on the order of the relativistic ion skin depth. Perpendicular electric and magnetic fields lead to the $\vec{E} \times \vec{B}$ motion of electrons parallel to the shock direction of propagation (x -direction). During this motion, the electrons are effectively heated.

At distances less than a Debye length, an electron at first moves in the direction opposite to the electric fields. Due to the velocity v_\perp thus obtained, the magnetic part of the Lorentz force produces a motion perpendicular to the electric and magnetic fields which instantly bends the electron trajectory. During the first-half gyration, the electron is accelerated at the expense of the potential energy stored in the transversal electric fields. On the other hand, the electron in its second-half gyration does work on the electric fields and its kinetic energy will be transferred to the electric field energy. The growth of the ion Weibel-like instabilities increases the electric charge of the ion filaments with time; hence in the next gyration the electron experiences deeper electric potentials that enhance the amplitude of energy oscillations. The maximum attainable energy for an electron during the heating stage can be estimated analytically. Approximately, an electron moving toward an ion current filament gains energy $u_{ele} \approx eE\Delta r \simeq eB\Delta r$ ($\beta_{xi} \simeq 1$). The maximum radial distance that the electron can travel is about half the distance between the filaments (measured from the filaments axes), $\Delta r \approx c/\omega_{pi,r}$, where $\omega_{pi,r} = (4\pi n_i e^2 / m_i \gamma_i)^{1/2}$ is the relativistic ion skin depth. Hence, the electron energy density is $\epsilon_{ele} \approx \sqrt{\epsilon_b}$ (normalized to the total incoming energy). Using this expression, the average change in the electron energy, $\langle \Delta E_e / m_e c^2 \rangle = \langle \Delta \gamma_e \rangle$, due to the transverse

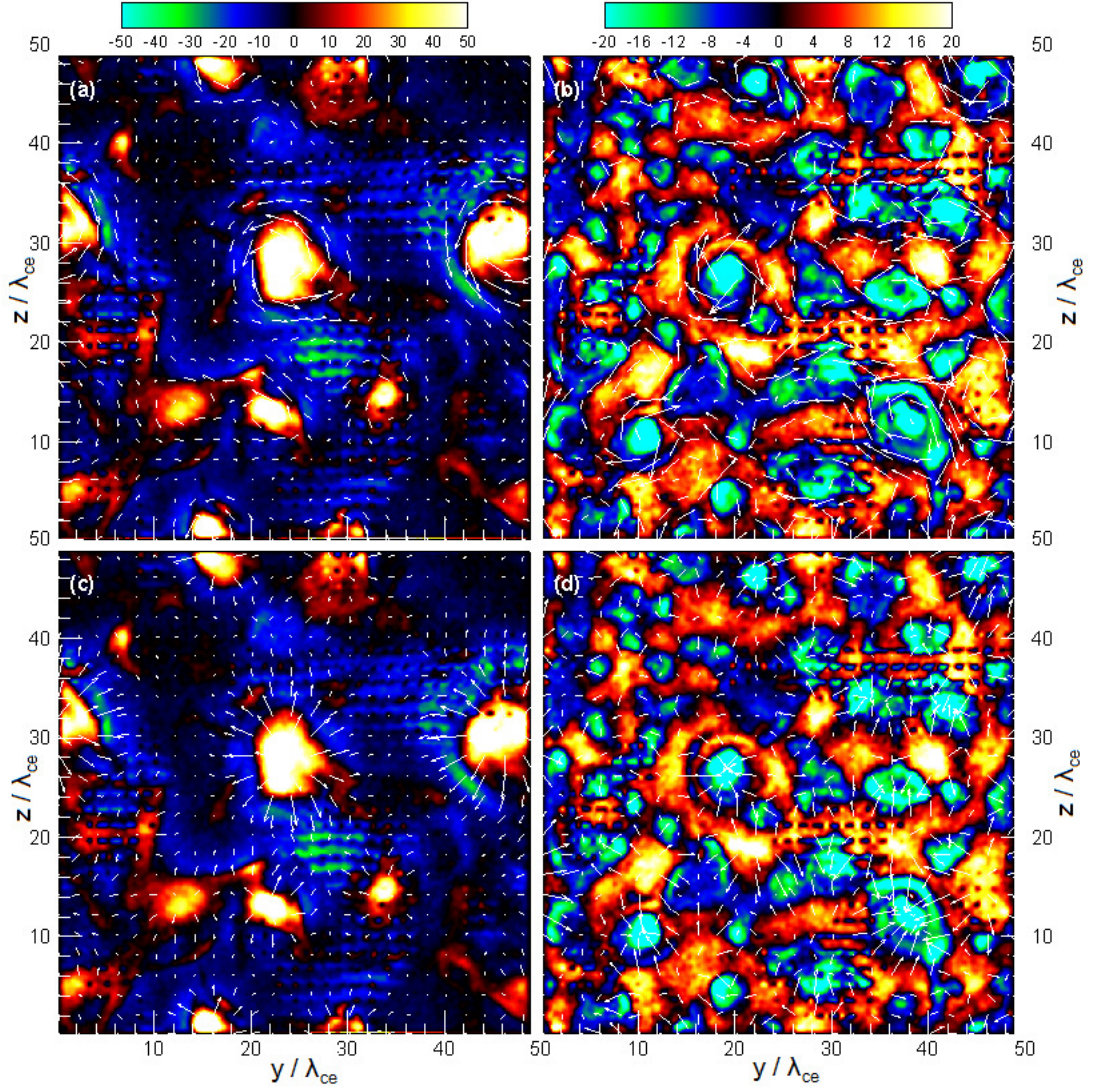


FIGURE 4.17: Longitudinal current density through a transverse cross section at $x = 320\lambda_{ce}$ (first column) and $x = 480\lambda_{ce}$ (second column) for $t = 500\omega_{pe}^{-1}$. The arrows represent the transverse magnetic (first row), and electric (second row) fields.

electric fields of ion filaments is displayed in Figure 4.18b. As can be seen, in the trailing edge, $x \lesssim 340\lambda_{ce}$, the electrons (mostly jet electrons) are heated by the ion filament up to 20MeV. Furthermore, due to the presence of a double layer in the trailing edge, the electrons can gain more energy within the double layer electric field. The maximum attainable energy through the double layer in the trailing edge is $e\langle\phi\rangle \simeq 20\text{MeV}$ (Figure 4.18c). Hence, the ion filaments and the double layer together increase the electron energy in the trailing edge by an average energy of 40MeV (Figure 4.18d). A similar process in the leading edge increases the average energy of the ambient electrons to 5MeV.

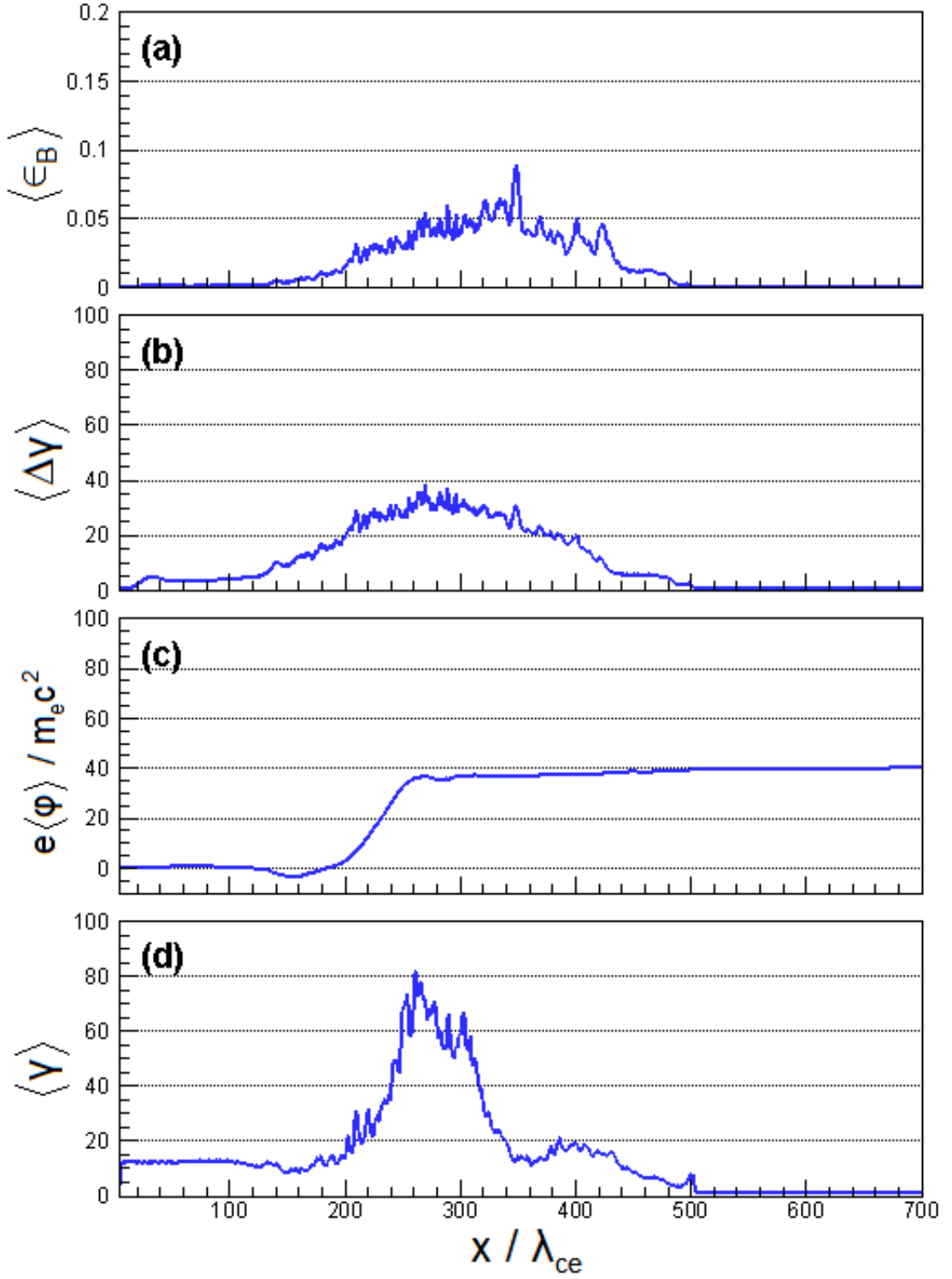


FIGURE 4.18: Electrons heating and acceleration. Displayed are: (a) magnetic energy density ϵ_B , normalized to the jet energy density, (b) average change in the electron energy due to the transverse electric fields of ion filaments, $\langle \Delta E_e / m_e c^2 \rangle = \langle \Delta \gamma_e \rangle$, (c) average change in the electron kinetic energy due to the double layer electric field, $e \langle \phi \rangle / m_e c^2$, and (d) average electron energy, $\langle \gamma_e \rangle$, along x -direction. All panels are calculated at $t = 500 \omega_{pe}^{-1}$.

4.4.7 Evolution of the electron distribution function

The common observational characteristic of PWNe, GRBs afterglows, and AGN jets is a broad non-thermal spectrum of synchrotron and inverse Compton emission that extends from the radio up to the gamma-ray band. One of the key ingredients in creating this non-thermal spectrum is a non-thermal, highly energetic electron population. This population may be seen in the electron distribution function where a pure 3D Maxwell-Jüttner distribution (in our case) does not account for the high energies. In fact, a more complex distribution function is expected as a result of electron acceleration. Shown in Figures 4.19 are the evolution of the electron distribution function over time (Figure 4.19a taken in the leading edge, Figure 4.19b taken in the shocked region, and Figure 4.19c taken in the trailing edge). At late stages, in both the leading and trailing edges, the electron distribution function consists of a drifting Maxwell-Jüttner distribution (our rest frame of reference is the ambient) and a high-energy tail. The electron distribution function in the shocked region illustrates a hot, well-mixed population (includes jet and ambient) with a drifting Maxwell-Jüttner distribution. The electron distribution functions in Figures 4.19a and 4.19c clearly develop a non-thermal tail over time. For $t \gtrsim 300\omega_{pe}^{-1}$, when the counter-streaming shock-reflected ions come to account a strong double layer forms in the trailing edge, the electrons are accelerated within the double layer. In this manner, their temperature does not changed significantly. This process is visible in the inset panel of Figure 4.19c where the most probable momentum, p_{mpm} , is constant for $t \gtrsim 300\omega_{pe}^{-1}$. The white line shows a power-law fit to the non-thermal, high-energy electron population. The power-law begins around $p_{min} = 12.5\text{MeV}/c$ and extends to high energies with an exponential cutoff. The power-law index α , defined in $N(p) \propto p^{-\alpha}$, has a best-fit value of $\alpha = 2.6$ in the leading edge, and $\alpha = 1.8$ in the trailing edge. The non-thermal tail in the electron distribution function (Figure 4.19a and 4.19c) extends over time to higher and higher energies. It clearly demonstrates that electron acceleration is efficient and perseveres over time. Regarding the electron distribution function in the leading edge, at time $t = 500\omega_{pe}^{-1}$, the non-thermal tail for $p \geq 12.5\text{MeV}/c$ contains $\sim 1\%$ of the electrons ($\sum_{p_e \geq p_{min}} N_i / \sum N_i$) and $\sim 8\%$ of the electron energy ($\sum_{p_e \geq p_{min}} N_i E_i / \sum N_i E_i$) in the leading edge. The acceleration efficiency for the electrons is $\sim 23\%$ by number and $\sim 50\%$ by energy in the trailing edge, calculated in the same way as the leading edge.

Theoretically, an ensemble of electrons with a power-law energy distribution function $N(\gamma)d\gamma \propto \gamma^{-\alpha}d\gamma$ (for the ultra-relativistic speeds $\gamma \propto p$) results in a radiation spectrum of $F(\nu) = \nu^{-s}$ (Rybicki and Lightman, 1979), where the spectral index s is related to the particle distribution index α by $s = (\alpha - 1)/2$. Therefore, $\alpha = 1.8 - 2.6$ in the electron energy distribution results in the spectral index $s = 0.4 - 0.8$ which is in the

range of the radio up to optical and X-ray emission (Bietenholz et al., 1997, Panaitescu, 2001, Panaitescu and Kumar, 2002).

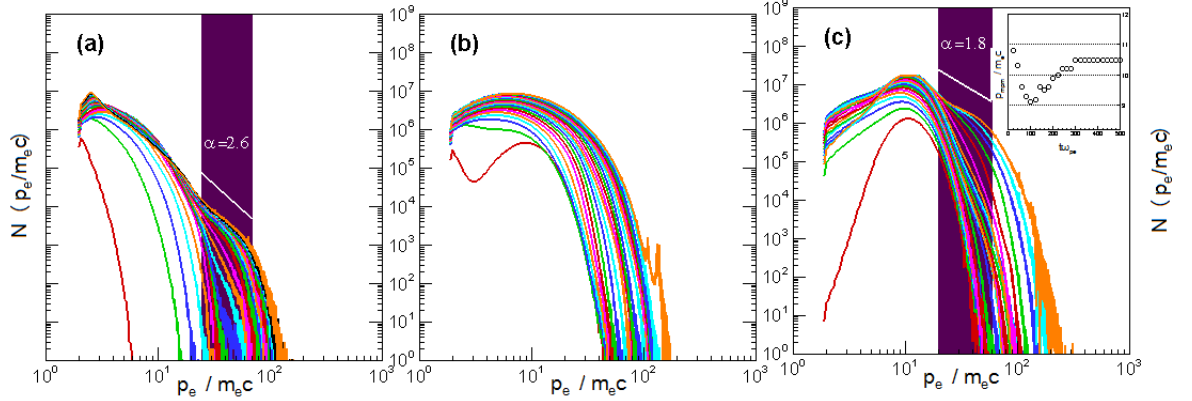


FIGURE 4.19: Evolution of the electron distribution function from $t = 20\omega_{pe}^{-1}$ (leftmost red line) up to $500\omega_{pe}^{-1}$ (rightmost orange line) with an interval of $\Delta t = 20\omega_{pe}^{-1}$: (a) for ambient in the leading edge taken at $(\beta_{41} - \beta_{ls1})t\omega_{pe}^{-1}$, (b) for ambient+jet in the shocked region taken at $(\beta_{ls1} - \beta_{ts1})t\omega_{pe}^{-1}$, and (c) for jet in the trailing edge taken at $x/\lambda_{ce} \lesssim \beta_{ts1}t\omega_{pe}^{-1}$. White line in panel (a) and (c) shows a power-law fit to the non-thermal component in the electron distribution function at the latest time. The inset in panel (c) shows the time evolution of the most probable momentum for jet electrons,

p_{mpm} .

4.4.8 Dependence on the dimensionality

Our reference run is performed in a 3D spatial domain. To examine effect of the dimensionality, we have run a simulation with the same physical parameters as in our reference run, but in a 2D computational domain. For the 2D run, the box size along the z -direction is only $1.6c/\omega_{pe}$ (8 grid cells). We find that the phase-space distributions of the particles and density structure agree well in terms of both the formed shock structure and the double layers in the trailing and leading edges. However the adiabatic index $\tilde{\Gamma} = 3/2$ in the 2D domain results in the slower shocks ($\beta_{ts1} = 0.60$ and $\beta_{ls1} = 0.87$) and smaller particle compression ($n_{31}/n_{41} = 2.0$ and $n_{21}/n_1 = 11.63$) compared to the 3D structure.

The time evolution of the electron distribution function from the 2D run is displayed in Figures 4.20. In our 2D run, the observed power-law index of the electron distribution function is $\alpha = 3.2$ in the leading edge, and $\alpha = 2$ in the trailing edge. The harder spectral index in 2D run could mean that the electron acceleration is more efficient than in 3D. Actually, the non-thermal tail in electron distribution function contains $\sim 2.3\%$ of electrons and $\sim 14\%$ of energy in the leading edge, and $\sim 24.4\%$ of electrons and $\sim 51.4\%$ of energy in the trailing edge, respectively.

In the early phase, the fields generated in the 3D simulation are stronger than in the 2D simulation due to the additional transverse dimension that the 3D instability can gather particles from. However, at later stages, the growth of fields in the 2D simulation surpasses the 3D case (Stockem et al., 2015). This is primarily caused by two effects. First, a 2D system has fewer degrees of freedom for the motion of particles; they are then more easily trapped and saturate in a larger amplitude. Second, ion current filaments can merge to larger transverse structures. This also can be followed in the 3D simulation but over longer times for a larger box.

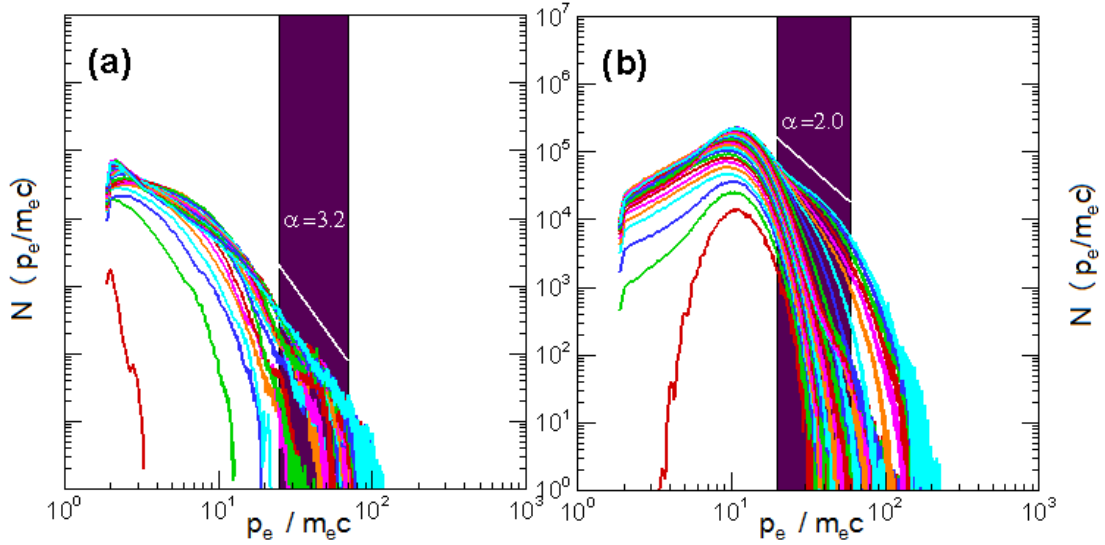


FIGURE 4.20: 2D run: Evolution of the electron distribution function from $t = 20\omega_{pe}^{-1}$ (leftmost red line) up to $560\omega_{pe}^{-1}$ (rightmost cyan line) with an interval of $\Delta t = 20\omega_{pe}^{-1}$: (a) for ambient in the leading edge taken at $(\beta_{41} - \beta_{ls1})t\omega_{pe}^{-1}$, and (b) for jet in the trailing edge taken at $x/\lambda_{ce} \lesssim \beta_{ts1}t\omega_{pe}^{-1}$. White line shows a power-law fit to the non-thermal component in the electron distribution function at the latest time.

4.5 Summary and conclusions

Our purpose has been dedicated to determine the mechanism that may accelerate electrons in the unmagnetized shock to energies, so that they can experience the DSA to ultra-relativistic energies. The observational radio synchrotron emissions from the supernova remnant shocks confirm the existence of such electrons (Uchiyama et al., 2007, Eriksen et al., 2011) although their origin is still unclear. The electrons contribute in the DSA, if their kinetic energies be equivalent to the ion kinetic energies (Hoshino et al., 1992, Hoshino, 2001, Amano and Hoshino, 2009, Reynolds, 2008, Hillas, 2005). It is believed that the electrons are pre-accelerated by instabilities, which are excited by ion beams in the transition region of shocks (Cargill and Papadopoulos, 1988, Hoshino et al., 1992, Hoshino, 2001). The origin of the ion can be the reflection of beam ions

in the shock region or the leaking of downstream ions into the upstream plasma. However, the Buneman instability (Buneman, 1958) and Weibel-like two-stream instability invoked in previous works (Hoshino, 2001, Hoshino and Shimada, 2002, Hededal et al., 2004, Medvedev, 2006, Amano and Hoshino, 2009) are not strong enough to inject the electrons into the DSA. They may simply exchange a few amount of the ion kinetic energy to the electrons.

The present work investigates the secondary processes triggered by the Weibel-like instabilities using a 3D PIC code (Buneman, 1993, Niemiec et al., 2008). The employed model of the simulation completely differs from the injection model used in several related papers (Hoshino, 2001, Hoshino and Shimada, 2002, Spitkovsky, 2008a,b, Amano and Hoshino, 2009, Martins et al., 2009, Sironi and Spitkovsky, 2011, Sironi et al., 2013, Guo et al., 2014). We have modeled an unmagnetized relativistic jet propagating into an ambient plasma. They contain ions and electrons. We have simulated the double shock system, and hence our model is self-consistent. The jet moves with a bulk speed of $0.995c$ in the x -direction relative to the ambient plasma. The initial temperatures of the species in the jet and ambient have been set to 46.25 keV and 0.6 keV, respectively, in their rest frame.

Three spatial directions have been resolved by the current PIC simulation, which indicates that the wave vector driven by the Weibel-like instabilities propagates obliquely with respect to the jet propagation direction (Bret et al., 2005, Bret, 2009, Bret et al., 2010). Both filamentation and two-stream modes are present and operate simultaneously in the electron heating. Consequently, strong fluctuations occur in the density of particles that result in the creation of the full shock system. The conclusions of the work presented here can be summarized as answers to the remarked questions in Section 4.1.

1. “How does the double shock structure form in the unmagnetized jet-ambient interactions?”

At early times, a CD forms between the decelerated jet electron and the swept up ambient electrons. Consequently, the jet electrons accumulate on the right side of CD as part of the TS. Additionally, a fraction of the ambient ions are located on the right side of CD because of the ion higher rigidity. They are swept by the jet continuous stream and contribute to the TS because of reflection by the CD. Therefore, we have defined the TS as a pile up of jet electrons and a fraction of ambient ions. On the other hand, the swept up ambient electrons and the swept up ambient ions on the right side of the CD construct the LS. In a longer simulation, when the jet ions become significantly decelerated we expect that jet ions will contribute to the both TS and LS structures.

2. “The shocks are characterized by magnetic or electrostatic forces?”

The electrostatic and magnetic effects are strongly activated at the same time in the captured double shock structure (a similar situation was also found for non-relativistic shocks in [Matsumoto et al. \(2013\)](#)). The transverse magnetic fields are induced due to the Weibel-like instabilities in the jet-ambient interaction. These fields are dominantly azimuthal and associated with the ion current filaments. In the shocked region, the magnetic energy density, ϵ_B , is near 10% of jet energy density. Transverse electric fields are also present around the ion current filaments due to the density filamentation by Weibel-like instabilities. The longitudinal electrostatic fields are due to the formed double layers in the trailing and leading edges. Both electrostatic force and $\vec{E} \times \vec{B}$ drift motion are important and play significant role in electron dynamics. However, in the shocked region, the induced magnetic fields facilitate energy transfer between the jet and ambient plasma.

3. “What are the main mechanisms responsible for electron injection?”

At first, the electrons are heated up to a maximum energy density $\epsilon_e \simeq \sqrt{\epsilon_B}$ via $\vec{E} \times \vec{B}$ drift motion. Additionally, the shock-reflected ambient ions trigger a double layer in the trailing edge which consequently evolves into an electrostatic shock. A double layer is also formed in the leading edge due to the decelerated jet ions and ambient electrons. The secondary electron energization process is associated with the electric fields of double layers. The drift speed of the free streaming particles is well in excess of the thermal one. It maintains the double layer structures over time. The substantial energy stored in the jet ions causes electron acceleration up to 75 MeV. The double layers convert the forward energy of the jet ions into the forward energy of the electrons without heating up the electrons. Electrons can thus be accelerated more efficiently by a double layer than by a shock because the latter spends part of the flow energy on heating.

4. “What is the resulting electron distribution function?”

The electron distribution function includes a non-thermal tail that contains $\sim 1\%$ of electrons and $\sim 8\%$ of electron energy in the leading edge, and $\sim 23\%$ of electrons and $\sim 50\%$ of electron energy in the trailing edge, respectively. The power-law fit to the non-thermal tail has index $\alpha = 1.8$ in the trailing edge, $\alpha = 2.6$ in the leading edge, respectively. These results confirm that the double layers are more efficient than shocks in electron acceleration. Based on the PIC simulations, the shocks efficiency in particle acceleration is $\sim 1\%$ by number and $\sim 10 - 15\%$ by energy ([Spitkovsky, 2008b](#), [Martins et al., 2009](#), [Sironi and Spitkovsky, 2011](#), [Sironi et al., 2013](#), [Guo et al., 2014](#)).

5. “What is the effect of the dimensionality?”

In the performed 2D simulation, the power-law index in the non-thermal tail is $\alpha = 3.2$ in the leading edge, and $\alpha = 2$ in the trailing edge, respectively. The non-thermal tail contains $\sim 2.3\%$ of electrons and $\sim 14\%$ of electron energy in the leading edge, and $\sim 24.4\%$ of electrons and $\sim 51.4\%$ of electron energy in the trailing edge, respectively. These values indicate that the electron acceleration in 2D is more efficient than in 3D.

The present work uses a ion-electron mass ratio $m_i/m_e = 16$. Although this low mass ratio is necessary to keep the computational costs of the 3D simulations reasonable, it changes the growth rate of the unstable modes as well. In the early growth stage, when the ions are not included in the instabilities, the magnetic field energy increases exponentially, independent of the mass ratio. However, the mass ratio effect becomes significant in the nonlinear phase. When it is small compared to the realistic one (1836), the saturation level of the magnetic field becomes higher, since the ion current filaments merge, similar to the electron ones, due to the mutual attraction between the filaments. Increasing the mass ratio will reduce the ion isotropization degree and the degree of kinetic energy transfer with electrons via the Weibel-like instabilities. Moreover, it is found that Weibel-like modes govern the high beam density regimes in the beam-plasma interactions (Bret and Dieckmann, 2010). The domains of these modes expand as the mass ratio decreases. Consequently, the domains governed by the oblique modes shrink with decreasing the mass ratio. Therefore, our low mass ratio places more importance on the Weibel-like instabilities than they normally have.

Regarding the double layers, the electrostatic potential jumps in the trailing and leading edges are established by the electron density and temperature jumps across the shocks. These jumps are in turn decided by the shock jump conditions that do not change significantly for different ion-to-electron mass ratios. Hence, the electrostatic potentials of the double layers are independent of the mass ratio. However, increasing the mass ratio will increase the kinetic energy of the ions. The ions are thus more difficultly slowed down in the double layers, causing the slower rate of kinetic energy exchange between the ions and electrons. In this manner, the TS, LS, and CD acquire their steady-state velocity later.

Chapter 5

Conclusions

5.1 The presented works

In this thesis, the results of the 3D PIC simulations of the relativistic jets that propagate into the ambient medium are presented. The employed code is a modified version of the publicly available TRISTAN PIC code. The simulations are performed on the KDK supercomputer in the Kyoto University, and performance of the code has been analyzed for the strong and weak scaling. Two major simulations are performed to: (1) study the fields structures, and (2) study the process of the shock formation, and particle acceleration during the propagation of the jets into the ambient medium. In first part, the ambient is denser than jet ($n_j/n_a = 8/12$), and is initially very cold, $T_e = T_i = 12.5 \times 10^{-4}$, relative to the rest mass energy. However, the jet is relatively hot $T_e = T_i = 0.092$. In the second part, the jet is denser and hot ($n_j/n_a = 10/6$), while the ambient is very cold same as before. In our simulations, the jets are propagating in the x -direction with the bulk Lorentz factor of $\gamma = 5$, and $\gamma = 10$, respectively, and make contact with the ambient in yz -plane. Both cases are for the unmagnetized electron-ion plasmas, and the mass ratios are 20, and 16, respectively.

5.2 Conclusions

The conclusions of the presented works are summarized in three major parts: (1) Performance analysis presented in Chapter 2, (2) The fields structures presented in Chapter 3, and (3) The shocks and particle acceleration presented in Chapter 3. These results are listed in the following:

1. Performance: Whereas the jet is propagating in x -direction, to have load balance during the simulation we use a configuration as $1 \times N_y \times N_z$ ($N_y = N_z$), where N_y , and N_z is number of processors in y , and z - direction, respectively. For the this setup under strong scaling, when the simulation is loaded over 512 processors, the communication time arise about 35 % of computation time which decrease the efficiency to 70 %, relative to a reference configuration where $1 \times N_y \times N_z = 4$. In the weak scaling analysis, the simulation size is increased as number of the processors increases. The results show that the code performance is around 95% and the communication time reaches about 4% of the computation time. It almost obey the relation of $\eta = 1 - T_{\text{com}}/T_{\text{tot}}$.
2. The fields structures: The propagation of the jets into the ambient medium is controlled by the Weibel-like instabilities that generate the mainly transverse electromagnetic fields $B_{\parallel}/B_{\perp} \approx 0.01$. The field scales are in order of the plasma skin depth and develop in length as the jet propagate into the ambient. The jet incoming energy is transferred to the generated fields via the current filamentation of the plasma, and these fields causes particles deflection in the transverse directions and subsequent anisotropies in the particles phase-space. The anisotropies amplify the induced fields until a saturated level of the magnetic fields.
3. The shocks and particle acceleration: The propagation of the jets into the ambient medium excites a double shock system, which includes TS and LS. They are separated by a CD. The fields are stronger in the TS region, due to the high degree of the anisotropy in the particles phase-space. In the both shocks, the Weible-like instabilities induce the transversal electromagnetic fields which cause $\vec{E} \times \vec{B}$ acceleration of the electrons. These fields are mainly attributed to the ions in the ambient, cause filimentation in the ambient is stronger. However, there is another important candidate for the electron acceleration which is double layer plasma. The reflection of the ambient ions by the LS, and the incoming jet electrons can produce a double layer that transfers a signification fraction of the jet ions to the electrons. Therefore, in the unmagnetized plasma, the double layers are important in the process of the electron injection. The double layers are more efficient than shocks in the acceleration because they do not waste the energy to the heating; they just convert the ions kinetic energy to the electrons kinetic energy. Therefore, in this process the temperature of the electrons does not change. It is also shown that the double layers are able to produce a power-law segment in the particle distributing function. The slop of the segment is consistent with the observations, as $\alpha = 1.8 - 2.6$. The effect of the dimensionality is investigated. It shows that double layers can be generated also in the 2D simulations, although the particle acceleration is more efficient in the 2D simulations than 3D simulations.

The present work uses a ion-electron mass ratio $m_i/m_e = 16 - 20$. Although these low mass ratios are necessary to keep the computational costs of the 3D simulations reasonable, they change the growth rate of the unstable modes as well. In the early growth stage, when the ions are not included in the instabilities, the magnetic field energy increases exponentially, independent of the mass ratio, electron Weibel-like instability where $\Gamma_e \propto \omega_{pe}$. However, the mass ratio effect becomes significant in the nonlinear phase, ion Weibel-like instability where $\Gamma_i \propto \omega_{pi} \propto (m_i/m_e)^{-1/2}$. When it is small compared to the realistic one (1836), the saturation level of the magnetic field becomes higher ($B_{\text{sat}} = \sqrt{2\mu_0} n^{1/2} m_p^{1/2} \beta_0 c \gamma_0^{1/2} / (1 + \beta_{\text{th}})$), since the ion current filaments merge, similar to the electron ones, due to the mutual attraction between the filaments. Increasing the mass ratio will reduce the ion isotropization rate and the rate of kinetic energy exchange with electrons via the Weibel-like instabilities. Moreover, it is found that Weibel-like modes govern the high beam density regimes in the beam-plasma interactions (Bret and Dieckmann, 2010). The domains of these modes expand as the mass ratio decreases. Consequently, the domains governed by the oblique modes shrink with decreasing the mass ratio. Therefore, our low mass ratio places more importance on the Weibel-like instabilities than they normally have.

Regarding the double layers, the electrostatic potential jumps in the trailing and leading edges are established by the electron density and temperature jumps across the shocks. These jumps are in turn decided by the shock jump conditions that do not change significantly for different ion-to-electron mass ratios. Hence, the electrostatic potentials of the double layers are independent of the mass ratio. However, increasing the mass ratio will increase the kinetic energy of the ions. The ions are thus more difficultly slowed down in the double layers, causing the slower rate of kinetic energy exchange between the ions and electrons. In this manner, the TS, LS, and CD acquire their steady-state velocity later.

5.3 Future works

The presented works were associated to the simulation of the relativistic electron - ion shocks in a self-consistent way. There are some more issues in this regard to be investigated. These issues are listed as the plan for the future researches. The suggestions for the futures works are summarized as follow:

1. The presented results were for the unmagnetized jet and ambient plasma. However, many of the astrophysical jets are magnetized. Therefore, study of the magnetized cases would provide useful information, regarding the self-consistent PIC simulation of the relativistic jets and shocks.

2. In the magnetized cases, the angle of the upstream magnetic field with respect to the propagation direction of the jet may also be an important parameter regarding the particle acceleration. Therefore, study the particle acceleration for the different angles can also provide useful information.
3. In this thesis, we just consider two Lorentz factors, $\gamma = 5$, and $\gamma = 10$. Investigation of the dependence of particle acceleration, and fields strength to the jet Lorentz factor is also an important issue.
4. The presented works, we use the ion-to-electron mass ratio of 16, and 20. As discussed before, these low mass ratios although are essential to make the computations efficient, they give a higher importance to the Weibel instability (Bret and Dieckmann, 2010). Therefore, using the larger mass ratios, such as 100 or higher, would provide more reliable results.
5. Another important mechanism for the particle accelerating is magnetic reconnection (Zenitani and Hoshino, 2001, 2007, 2008, Sironi and Spitkovsky, 2014), which spend the magnetic energy stored in the magnetic fields for the kinetic energy of the particles (See Figure 5.1). Investigation of this issue can also provide better view about the responsible mechanisms for the particle acceleration in the jets and shocks. To follow this process, a large simulation box and longer simulation time is needed. During this process, the filaments merge together and reconnection would happen in some sites, where particle acceleration take places.

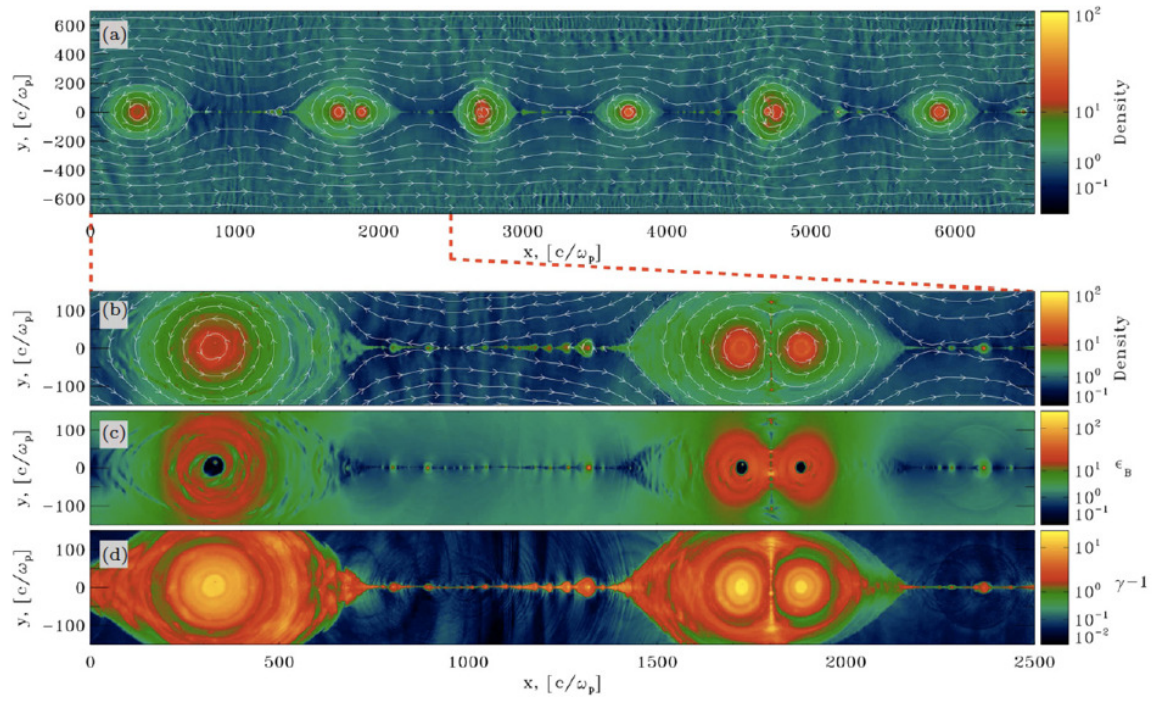


FIGURE 5.1: Illustration of the magnetic reconnection where magnetic field lines configuration is reformed, panel (a), and the magnetic energy will be transferred to the kinetic energy of the particle in the reconnection site, panels (b), (c), and (d). Source: [Sironi and Spitkovsky \(2014\)](#).

Appendix A

The mean free path in relativistic jet-ambient interactions

In this section, We review an approximation of the mean free path for Coulomb collisions of a relativistic electron with momentum $\gamma m_e \vec{v}_e$ in a ambient plasma with density n , based on what presented in [Zel'dovich and Raizer \(2002\)](#), [Heddal \(2005a\)](#).

At first, lets look at the Coulomb collision between an electron and an ion. For simplicity in calculations and without loss of the problem generality, it is supposed that the electron is moving in yz -plane along the z -axis and the ion is located at $(x, y, z) = (0, -b, 0)$. The ion has the surrounding electric fields. Due to the Lorentz contraction and symmetry arguments we can assume that the electron will only be affected by the component that is transverse to \vec{v}_e , namely E_y . In the reference frame of the electron, this component is given by:

$$E_y = \frac{1}{4\pi\epsilon_0} \frac{q\gamma b}{(\gamma^2 v_e^2 t^2 + b^2)^{3/2}} \quad (\text{A.1})$$

where t is the time, calculated so that the electron is in $(0, 0, 0)$ at $t = 0$. The force exerted to the electron is $\vec{F} = qE_y \vec{j}$. The change in the electron momentum δp is as:

$$\delta p = \int dt F_y = \int dt q E_y = \frac{1}{4\pi\epsilon_0} \frac{q^2 \gamma t}{(\gamma^2 v_e^2 t^2 + b^2)^{1/2}} \quad (\text{A.2})$$

The pulse from the ion is felt by the electron in the short time interval $T \simeq b/(\gamma v_e)$. Inserting this into Eq. [A.2](#) we find

$$\delta p = \frac{1}{4\pi\epsilon_0} \frac{q^2}{\sqrt{2}v_e b} \quad (\text{A.3})$$

We are interested in collisions that alter the impinging electrons momentum significantly with $\delta p \simeq \gamma m_e v_e$, and we can thus find the distance b_c for such a collision:

$$\delta p \simeq \gamma m_e v_e \quad (\text{A.4a})$$

$$b_c \simeq \frac{1}{4\pi\epsilon_0} \frac{q^2}{\sqrt{2}\gamma m_e v_e^2} \quad (\text{A.4b})$$

Thus, the cross section for the collision is

$$\sigma_c = \pi b_c^2 = \frac{q^4}{32\pi\epsilon_0^2\gamma^2 m_e^2 v_e^4} \quad (\text{A.5})$$

The collision frequency is $\nu_c = n\sigma_c v_e$ and from this we find the mean free path for a full collision:

$$\lambda_{\text{mfp}} = \frac{v_e}{\nu_c} = \frac{1}{n\sigma_c} = \frac{32\pi\epsilon_0^2\gamma^2 m_e^2 v_e^4}{nq^4} \quad (\text{A.6})$$

In reality, the mean free path somewhat shorter because of accumulation of small angle deflections. We can correct for this by introducing a correction factor $1/\ln \Lambda$, which is of the order of 0.1.

For a electron in a blast wave that is expanding with Lorentz factor $\gamma \simeq \Gamma = 10$, into an interstellar medium with density $n \simeq 10^6 \text{m}^{-3}$, the mean free path for a collision is larger than 10^{24}m . Comparing this number with the typical size of a GRB blast wave $\sim 10^{14} \text{m}$ we conclude that it is reasonable to neglect collisions between the ejecta and ISM, and that the shock between the two is to be regarded as a “collisionless shock”.

Acknowledgements

I would like to extend my gratitude to:

Prof. [Dongsheng Cai](#) for being my supervisor and a great source of inspiration and motivation to students.

Prof. [Ken-Ichi Nishikawa](#) and Prof. [Bertrand Lembége](#) for collaboration, discussions and much more.

[University of Tsukuba](#) and [Department of Computer Science](#) in [Graduate Schools of Systems and Information Engineering](#) for three years of financial support of my PhD studies.

All member of the [CAVELAB](#) laboratory, specially Mrs. Obana for her helps during my study in [CAVELAB](#).

The simulations presented here were performed on the KDK computer system at [Research Institute for Sustainable Humanosphere, Kyoto University](#).

Bibliography

- Achterberg, A., and Wiersma, J., 2007, *Astronomy and Astrophysics*, 475, 1-18.
- Amano, T., and Hoshino, M. 2007, *The Astrophysical Journal*, 690, 244-251.
- Ardaneh, K., Cai, D., and Nishikawa, K-I. 2014, *New Astronomy*, 33, 1-6.
- Ardaneh, K., Cai, D., and Nishikawa, K-I., Lembége, B. 2015, *The Astrophysical Journal*, 811, 57.
- Ardaneh, K., Cai, D., and Nishikawa, K-I. 2016, *The Astrophysical Journal*, 827, 124.
- Balogh, A., and Treumann, R. A., 2013, *Physics of Collisionless Shocks: Space Plasma Shock Waves*, Springer Science and Business Media, New York, First edition.
- Begelman, M. C., and Kirk, J. G. 1990, *The Astrophysical Journal*, 353, 66.
- Bell, A. R. 1978, *Monthly Notices of the Royal Astronomical Society*, 182, 147.
- Bell, A. R. 2013, *Astroparticle Physics*, 43, 56.
- Bietenholz, M. F., Kassim, N., Frail, D. A., Perley, R. A., Erickson, W. C., and Hajian, A. R. 1997, *The Astrophysical Journal*, 490, 291-301.
- Birdsall, C. K., and Langdon, A. B., 1991. *Plasma physics via computer simulation*. Adam Hilger, Bristol.
- Biretta, J. 1957. *Hubble Detects Faster-Than-Light Motion in Galaxy M87*.
- Blandford, R. D, and Znajek, R. L. 1977. *Monthly Notices of the Royal Astronomical Society*. 179, 433.
- Blandford, R., and Eichler, D. 1987, *Physics Reports*, 154, 1-75.
- Blandford, R. D., and Ostriker, J. P. 1978, *The Astrophysical Journal*, 221, L29.
- Block, L. P., 1978, *Astrophysics and Space Science*, 55, 59.
- Bošnjak, Ž., Daigne, F., and Dubus, G., 2009, *Astronomy and Astrophysics*, 498, 677.

- Brainerd, J. J., 2000, *The Astrophysical Journal*, 538, 628-637.
- Bret, A., Firpo, M.-C., and Deutsch, C. 2005, *Physical Review Letters*, 94, 115002.
- Bret, A. 2009, *The Astrophysical Journal*, 699, 990.
- Bret, A., Gremillet, L., and Benisti, D. 2010, *Physical Review E*, 81, 036402.
- Bret, A., and Dieckmann, M. E. 2010. *Physics of Plasmas*, 17, 032109.
- Buneman, O. 1958, *prl*, 1, 8-9.
- Buneman, O. 1993, Tristan, in *Computer Space Plasma Physics, Simulation Techniques and Software*, ed. H. Matsumoto and Y. Omura (Tokyo: Terra Scientific Publishing Company), 67.
- Bykov, A. M., and Toptygin, I. N., 1985, *Soviet Astronomy Letters*, 11, 75-77.
- Bykov, A. M., and Treumann, R. A. 2011. *The Astronomy and Astrophysics Review*, 19, 1.
- Califano, F., Cecchi T., and Chiuderi C. 2002, *Physics of Plasmas*, 9, 451-457.
- Cargill, P. J., and Papadopoulos, K. 1988, *The Astrophysical Journal*, 329, L29.
- Chaisson, E., McMillan., and McMillan, S. 2014. *Astronomy Today*, 8th Edition, Figure 24.35, p634, Pearson Education, Inc.
- Chang, P., Spitkovsky, A., and Arons J., 2008, *The Astrophysical Journal*, 674, 378-387.
- Chen, G., and Armstrong, T. P. 1975, in *Proc. 14th ICRC (Munich)*, Vol. 5, 1814.
- Cherepashchuk, A., 2002, *Space Science Reviews*, 102, 23.
- Choi, E. J., Min, K., Nishikawa, K.-I., and Choi, C. R. 2014, *Physics of Plasmas*, 21, 072905.
- David L. Meier, et al. 2001, *Science* 291, 84.
- Dawson, J. M., 1983, *Reviews of Modern Physics*, 55, 403-447.
- de Gouveia Dal Pino, E. M. 2005, *Advances in Space Research*, 35, 908.
- Dieckmann, M. E., Frederiksen, J. T., Bret, A., and Shukla, P. K. 2006, *Physics of Plasmas*, 13, 112110.
- Dieckmann, M. E., and Bret, A. 2009, *The Astrophysical Journal*, 694, 154-164.
- Drury, L. O. 1983, *Reports on Progress in Physics*, 46, 973.

- Eriksen, K. A., Hughes, J. P., Badenes, C., Fesen, R., Ghavamian, P., Moffett, D., Pluckinsky, P. P., Rakowski, C. E., Reynoso, E. M., and Slane, P. 2011, *The Astrophysical Journal Letters*, 728, L28.
- Frey, H. U., Phan, T. D., Fuselier, S. A., and Mende, S. B. 2003, *Nature* 426, 533.
- Fonseca, R. A., Silva, L. O., Tonge, J., Hemker, R. G., Dawson, J. M., and Mori, W. B., 2002, *IEEE Transactions on Plasma Science*, 30, 28-29.
- Forslund, D. W., and Shonk, C. R. 1970, *Physical Review Letters*, 25, 1699.
- Forslund, D. W., and Freidberg, J. P. 1971, *Physical Review Letters*, 27, 1189.
- Frederiksen, J. T., Hededal, C. B., Haugbølle, T., and Nordlund, Å. 2004, *The Astrophysical Journal Letters*, 608, L13-L16.
- Fried, B. D., 1959, *Physics of Fluids*, 2, 337.
- Greenwood, A. D., Cartwright, K. L., Luginsland, J. W., and Baca, E. A. 2004, *Journal of Computational Physics*, 201, 665.
- Gruzinov, A., 2001, *The Astrophysical Journal*, 563, L15-L18.
- Guo, X., Sironi, L., and Narayan, R. 2014, *The Astrophysical Journal*, 794-153.
- Hededal, C. B., Haugbølle, T., Frederiksen, J. T., and Nordlund, Å. 2004, *The Astrophysical Journal Letters*, 617, L107-L110.
- Hededal, C. B. 2005, Ph.D. thesis, Niels Bohr Inst.
- Hededal, C. B., and Nishikawa, K.-I. 2005, *The Astrophysical Journal Letters*, 623, L89-L92.
- Hillas, A. M. 2005, *Journal of Physics G*, 31, R95.
- Hoshino, M., Arons, J., Gallant, Y. A., and Langdon, A.B., 1992, *The Astrophysical Journal*, 390, 454.
- Hoshino, M. 2001, *Progress of Theoretical Physics Supplements*, 143, 149-181.
- Hoshino, M., and Shimada, N. 2002, *The Astrophysical Journal*, 572, 880-887.
- Jarosechek, C. H., Lesch, H., and Treumann, R. A., 2005, *The Astrophysical Journal*, 618, 822-831.
- Junor, W., Biretta, J., and Livio, M. 1999, *Nature* 401, (6756), 891-892.
- Kennel, C. F., and Coroniti, F. V., 1984, *The Astrophysical Journal*, 283, 694-709.

- Koyama, K., Petre, R., Gotthelf, E. V., Hwang, U., Matsuura, M., Ozaki, M., and Holt, S. S. 1995, *Nature*, 378, 255.
- Lee, M. A., Shapiro, V. D., and Sagdeev, R. Z. 1996, *Journal of Geophysical Research*, 101, 4777.
- Lindman, E. L., 1975, *Journal of Computational Physics*, 18, 66-78.
- Martins, S. F., Fonseca, R. A., Silva, L. O., and Mori, W. B. 2009, *The Astrophysical Journal Letters*, 695, L189-L193.
- Masters, A., Stawarz, L., Fujimoto, M., Schwartz, S. J., Sergis, N., Thomsen, M. F., Retino, A., Hasegawa, H., Zieger, B., Lewis, G. R., Coates, A. J., Canu, P., and Dougherty, M. K. 2013, *Nature Physics*, 9, 164.
- Matsumoto, Y., Amano, T., and Hoshino, M. 2012, *The Astrophysical Journal*, 755, 109.
- Matsumoto, Y., Amano, T., and Hoshino, M. 2013, *Physical Review Letters*, 111, 215003.
- Medvedev, M. V., and Loeb, A. 1999, *The Astrophysical Journal*, 526, 697-706.
- Medvedev, M. V. 2006, *The Astrophysical Journal Letters*, 651, L9-L11.
- Medvedev, M. V., 2007, *Astrophysics and Space Science*, 307, 245-250.
- Newman, D. L., Andersson, L., Goldman, M. V., Ergun, R. E., and Sen, N. 2008, *Physics of Plasmas*, 15, 072902.
- Niemiec, J. and Ostrowski, M. 2004, *The Astrophysical Journal*, 610, 851.
- Niemiec, J., Pohl, M., Stroman, T. and Nishikawa, K.-I. 2008, *The Astrophysical Journal*, 684, 1174.
- Niemiec, J., Pohl, M., Bret, A. and Wieland, V. 2012, *The Astrophysical Journal*, 759, 73.
- Nishikawa, K.-I., Hardee, P., Richardson, G., Preece, R., Sol, H., and Fishman, G. J. 2003, *The Astrophysical Journal*, 595, 555-563.
- . 2005, *The Astrophysical Journal*, 622, 927-937.
- Nishikawa, K.-I., Niemiec, J., Hardee, P. E., Medvedev, M., Sol, H., Mizuno, Y., Zhang, B., Pohl, M., Oka, M., and Hartmann, D. H. 2009, *The Astrophysical Journal Letters*, 698, L10-L13.

- Nishikawa, K. I., Frederiksen, J. T., Nordlund, A., Mizuno, Y., Hardee, P. E., Niemiec, J., Gomez, J. L., Péér, A., Dutan, I., Meli, A., Sol, H., Pohl, M., and Hartman, D. H. 2016, *The Astrophysical Journal*, 820, 94.
- Omura, Y., and Matsumoto, H., 1993, KEMPO1: Technical guide to one dimensional electromagnetic particle code, in *Computer Space Plasma Physics*, edited by H. Matsumoto and Y. Omura, pp.21-65, Terra Scientific, Tokyo.
- Paciesas, W. S., et al. 1999, *The Astrophysical Journal Supplement Series*, 122, 465.
- Panaiteanu, A. 2001, *The Astrophysical Journal*, 556, 1002-1009.
- Panaiteanu, A., and Kumar, P. 2002, *The Astrophysical Journal*, 571, 779-789.
- Park, J., Workman, J. C., Blackman, E. G., Ren, C., and Siller, R. 2012, *Physics of Plasmas*, 19, 062904.
- Park, J., Ren, C., Workman, J. C., and Blackman, E. G. 2013, *The Astrophysical Journal*, 765, 147.
- Patruno, A., and Watts, A. L. 2012. arXiv:1206.2727, astro-ph.HE.
- Pavan, L. et al. 2014. *Astronomy and Astrophysics*, 562, A122.
- Penrose, R. 1969. *General Relativity and Gravitation*, 34, 1141.
- Petri, J., and Kirk, J. G., 2007, *Plasma Physics and Controlled Fusion*, 49, 1885-1896.
- Piran, T. 2003. *Nature*, 422, 268.
- Pruet, J., Abazajian, K., and Fuller, G. M., 2001, *Physical Review D*, 64 (063002-1).
- Rebhan, A. 2009. *Progress in Particle and Nuclear Physics*, 62, 518-528.
- Reynolds, S. R. 2008, *Annual Review of Astronomy and Astrophysics*, 46, 89.
- Rybicki, G. B. and Lightman, A. P. 1979, *Radiative Processes in Astrophysics*, John Wiley and Sons, Inc, New York, 3rd edition.
- Sagdeev, R. Z., 1966, *Reviews of Plasma Physics*, 4, 23.
- Sari, R., Piran, T., and Narayan, R., 1998, *The Astrophysical Journal Letters*, 497, L17.
- Schilling, G., 2002, *Flash The hunt for the biggest explosions in the universe*, Cambridge University Press.
- Schmidt, G. D., Angel, J. R. P., and Beaver, E. A. 1979, *The Astrophysical Journal*, 227, 106.

- Silva, L. O., Fonseca, R. A., Tonge, J. W., Dawson, J. M., Mori, W. B., and Medvedev, M. V., 2003, *The Astrophysical Journal*, 596, L121-L124.
- Sironi, L. 2011, Ph.D. thesis, Princeton University.
- Sironi, L., and Spitkovsky, A. 2011, *The Astrophysical Journal*, 726, 75.
- Sironi, L., Spitkovsky, A., and Arons, J. 2013, *The Astrophysical Journal*, 771, 54.
- Sironi, L., and Spitkovsky, A. 2014, *The Astrophysical Journal*, 783, L21.
- Shapiro, V. D., and Ücer, D. 2003, *Planetary and Space Science*, 51, 665.
- Spitkovsky, A. 2008a, *The Astrophysical Journal Letters*, 673, L39-L42.
- . 2008b, *The Astrophysical Journal Letters*, 682, L5-L8.
- Stockem, A. N., Bret, A., Fonseca, R. A., and Silva, L. O., 2015, *Plasma Physics and Controlled Fusion*, 58, 014005.
- Tanvir, N. R. et al. 2013, *Nature*, 29, 500 (7464), 547-9.
- Tautz, R. C., and Schlickeiser, R., 2006, *Physics of Plasmas*, 13, 062901.
- Tautz, R.C., and Lerche, I. 2012, *Physics Reports*, 520, 1.
- Uchiyama, Y., Aharonian, F. A., Tanaka, T., Takahashi, T., and Maeda, Y. 2007, *Nature*, 449, 576.
- Vink, J., 2004, *Advances in Space Research*, 33, 356.
- Wang, J., Liewer, P., and Decyk, V., *Computer Physics Communications*, 1995, 87, 35-53.
- Wardle, J. F. C., Homan, D. C., Ojha, R., and Roberts, D. H. 1989, *Nature*, 359, 457.
- Waxman, E., 1997, *The Astrophysical Journal*, 485, L5.
- Waxman, E., 2006, *Plasma Physics and Controlled Fusion*, 48, 12B.
- Webb, G. M., Axford, W. I., and Terasawa, T. 1983, *The Astrophysical Journal*, 270, 537.
- Weibel, E. S. 1959, *Physical Review Letters*, 2, 83.
- Wehrle, A.E., Zacharias, N., Johnston, K. et al. 2009. *The Astronomy and Astrophysics Decadal Survey*, 310.
- Wieland, V., Pohl, M., Niemiec, J., Rafighi, I., and Nishikawa, K.-I. 2016, *The Astrophysical Journal*, 820, 62.

- Yee, K.S., 1966, IEEE Transactions on Antennas and Propagation, 14, 302-307.
- Yoon, P. H., and Davidson, R.C., 1987, Physical Review A, 35, 2718.
- Zel'dovich, Y. B., and Raizer, Y. P., 2002, Physics of shock waves and high-temperature hydrodynamic phenomena, edited by Hayes, W. D., and Probstein, R. F., Dover Publications.
- Zenitani, S., and Hoshino, M. 2001, The Astrophysical Journal, 562, L63
- Zenitani, S., and Hoshino, M. 2007, The Astrophysical Journal, 670, 702
- Zenitani, S., and Hoshino, M. 2008, The Astrophysical Journal, 677, 530
- Zhang, B., and Kobayashi, S., 2005, The Astrophysical Journal, 628, 315-334.